Optical Nonlinear Effects and Photon Pair Production in Modulated Materials

Hatef Dinparasti Saleh

Submitted for the degree of Doctor of Philosophy

Heriot-Watt University

School of Engineering and Physical Sciences

Institute of Physics and Quantum Sciences

June 2017

Abstract

According to quantum field theory an oscillation of boundary conditions in the vacuum can generate real photon pairs, which pop into existence from the zero-point energy. This surprising effect is known as the dynamical Casimir effect (DCE). In this thesis, we focus our attention on using the DCE as a route to experimentally study the quantum vacuum.

Initially we explore experimental approaches that rely on an oscillation of vacuum boundary conditions. These require a direct temporal modulation of the boundary condition, which we achieve by temporally modulating the refractive index through the second order nonlinearity of the medium. We show that the key condition for this approach is that the medium is subwavelength in thickness. This leads to a temporal modulation of the refractive index. We use a mechanically exfoliated MoS_2 monolayer. We present a detailed study of the second order nonlinearity of 2D (mono-atomic layer) dichalcogenide MoS_2, and test its potential for spontaneous parametric down-conversion (SPDC) i.e. amplification of vacuum fluctuations mediated by optical nonlinearity. We present a model of SPDC in MoS_2 monolayers and show that our data are compatible with theoretical estimates. We show exciting indications that SPDC may be possible in this material by performing polarization and lifetime measurements. We also discuss and characterise a new photo-luminescence emission around 1500 nm which is enhanced at the edges of multi-layer MoS_2.

In chapter three we present experimental approaches using spatially modulated third order nonlinear media along the propagation axis. We show that under certain conditions the spatial modulation of the boundary conditions along the nonliner media can be considered as a temporal modulation. Modulated waveguides provide an intensity variation of the pulse along the waveguide. Two different materials are used as substrate material for the waveguides; gallium lanthanum sulphide (GLS), which has a high third order nonlinear susceptibility and fused silica. We present numerical simulation results for photon generation from the modulated waveguides in GLS sample. We also characterise the nonlinear response and effects of the waveguides. In both substrates, we show that the lack of nonlinearity and different sources of losses prevents the creation of photon pairs.

Finally, we present an experimental method in which the group velocity dispersion (GVD) is modulated along a photonic crystal fiber. Measurements of the temporal correlations between the newly generated frequencies is presented with a coincident to accidental ratio (CAR) of 7.5: yielding proof of a quantum correlation between the generated photon pairs.

I DEDICATE THIS THESIS FOR MY LOVED ONES.

ACKNOWLEDGMENTS

First of all, I would like to thank my supervisor Prof. Daniele Faccio for providing me this opportunity and his kind support, patience and guidance throughout my PhD.

I am extremely thankful for invaluable support of Dr. Thomas Roger, Dr. Stefano Vezzoli , Julius Heitz, Rosie Hayward and Dr. Ashley Lyons. Thank you very much for being amazing advisors and friends. I am also grateful to Dr. Lucia Caspani, Dr. Matteo Clerici, Dr. Dr Constantine Aniculaesi for their kind support during my PhD. I learned so much from you.

I would like to thank Michael Marshall, Calum Maitland, Niclas Westerberg for their suggestions and advices. Furthermore, I would like to thank all the members of the Extreme Light Group.

My incredible Anechka, there are so much to be grateful for, but foremost for all your love, motivation and endless support. I am so lucky to have you in my life.

My wonderful parents, thank you very much for your invaluable and sincere support throughout whole my life. I would not be the person who I am today and where I am now without your endless love, support and motivations.

Table of Contents

1 Introduction

1.1 Quantum fluctuation and dynamical Casimir effect

Quantum field theory has profoundly changed our conception of empty space. Indeed, even by removing all the particles from a material enclosure and cooling its temperature down to absolute zero, thus eliminating thermal radiation, there is still within the enclosure irreducible quantum fluctuations of the electric field. These fluctuations, also called vacuum fluctuations or zero-point energy, correspond to an average energy of $\frac{1}{2}\hbar\omega$, where ω is the field frequency [1]. One of the amazing aspects of quantum field theory is that it predicts the possibility of generating real photon pairs from the vacuum state. Quantum vacuum fluctuations inherently lead to the generation of particles, which spontaneously pop into existence, if only for a very short period of time. The underlying phenomena behind some of the most exciting and fundamental theories about the physics of our Universe, such as Casimir force, Unruh effect, Hawking radiation and dynamical Casimir Effect (DCE), rely on these fluctuations [1]–[5]. In this thesis, we will focus our attention on DCE as a route to experimentally exploring the quantum vacuum.

In contrast to effects like the Casimir force, which are based on a static quantum vacuum and have already been verified experimentally, other effects such as the DCE, which are time dependent quantum vacuum effects, have not yet been observed in their pure form. The reason for this is due to the extreme experimental conditions required for these effects to become measurable. For instance, to observe the DCE one needs to oscillate the boundary conditions of the electromagnetic field extremely fast, with frequencies equal to that of light [6].

The DCE is often confused with the static Casimir effect, whose measurable quantity is the Casimir force. The Casimir force describes the attraction force felt between two parallel plates at rest in the vacuum, this force occurs because of the effective pressure of the quantum vacuum on the plates [1]. However, the DCE is a completely different effect. The DCE can be described by considering the two mirrors of a laser cavity. When one

considers a laser cavity there are certain allowed wavelengths (or modes) that can be supported by the cavity, which are dependent on the distance between the two mirrors. Since these modes depend on the length of the cavity, the frequency of the supported modes will change if one changes the distance between the mirrors. However, if we make this change to the cavity rapidly, for instance on a time scale comparable to the inverse of the frequency of the propagating light field, the effect becomes very different because the field can't keep up with such a fast-moving oscillation. According to quantum field theory the result of this non-adiabatic change to the cavity length is that photons will be spontaneously produced from the vacuum.

In fact, if we were to set up a cavity whose length was very rapidly oscillating we would expect a change in the vacuum density between the cavity mirrors. However, the radiation force due to vacuum fluctuations tends to oppose any movement of the mirrors [7]. The mirror therefore undergoes an average force opposing its movement [8]. By conserving energy, the mirror must spontaneously emit photon pairs. This radiation shows the reciprocal influence between the vacuum fluctuation and the mechanical movement of the cavity.

Directly studying photon production from an oscillating mirror requires extreme experimental conditions, therefore researchers have proposed analogue systems to verify this effect. The main task to study the photon generation as a consequence of the DCE is to oscillate the boundary conditions of the electromagnetic field. This only takes place when the acceleration depends on time (as for example in the case of a harmonic oscillation of the mirror). This is the most important criteria for the DCE and we will consider analogues of this effect. In this thesis, we focus our interest on optical analogues of DCE.

1.2 Dynamical Casimir effect in literature

The DCE was initially studied in 1970. In this seminal work Moore studied the photon generation at zero-point field energy from the moving mirror in one dimensional system [5]. The effect of photon generation from the vacuum state due to the oscillation of the environment geometry, was first presented in the context of the DCE by Yablonovitch and Schwinger [9], [10]. Following this, the connection between the zero-point energy and boundary motion was presented as the “nonstationary Casimir effect” in [11], [12]. Barton et.al [13] and Lambrecht et.al [14] proposed “mirror-induced

radiation" and "motion-induced radiation". Later "quantum time-dependant oscillators" and "parametric dynamical Cassimir effect" were proposed, where the photon pairs were created from parametric oscillation of vacuum fluctuation in a media rather than by physical movement or oscillating boundaries [15], [16]. However, these proposals proved experimentally out of reach.

In 2011 the possibility of the DCE photon production from the vacuum state by providing an efficient modulation of the effective optical length of a cavity mode in the near-infrared spectral region [17]. In this proposal authors consider the optical cavity resides within a photonic nanowire or waveguide and is externally excited by a periodic laser pulse train that modulates the cavity optical length through the nonlinear Kerr effect.

Considering the difficulties in the generation of photon pairs from mechanical oscillation, proposals mimicking the oscillation of the boundary conditions has attracted great interest among researchers. In 1988, Yablonovitch presented the first experimental proposal to use a medium with fast change in refractive index [9]. He also proposed that rapid changes of the dielectric properties of a semiconductor can be induced by sub-picosecond laser pulses. Ideas based on rapid change of the refractive index of semiconductors induced by pulsed laser beam and similar variations upon this scheme were developed in [18]–[20]. The concept behind this experimental proposal is to imitate an oscillating mirror with a "plasma mirror" formed by electron-hole pairs. This occurs in a thin semiconducting film when pumped with a pulsed laser beam. In this case, a layer with higher conducting properties will be periodically created in front of the semiconductor film. This happens if the carrier recombination time of the material is less than the time gap between laser pulses [21].

There has also been a similar proposal, in which superconducting layers are illuminated by intense laser pulses. However, the response of the superconductor to the laser pulse leads to the softening of the surface. Under these conditions the dielectric properties of the material will change as the result of local surface heating, which leads to the transition from the superconducting to normal conducting phase. Tsindlekht et.al reported the modulation of the frequency of a superconducting microwave resonator induced by laser excitation [22].

The idea of using the Josephson junctions with time-dependent parameters such as capacitance, inductance etc., were proposed in literature [23]–[26]. Eventually,

Wilson et.al presented the observation of DCE in a superconducting circuit [27]. In this experiment, they modulate the inductance of the superconducting quantum interference device at frequency higher than 10 GHz.

1.3 Nonlinear optical analogues of dynamical Casimir Effect

From the mathematical point of view, temporal modulation of any parameter in the wave equation leads to the modulation of electromagnetic field. In other words, the temporal modulation of any parameter in the wave equation is equivalent to the oscillation of the boundary conditions of electromagnetic field, which is indeed an analogue of DCE.

In this thesis, we consider three optical experiments for the verification of the DCE. In all these approaches, we imitate the mechanical boundary oscillation by the oscillation of the optical parameters, which correspond to nonlinear optical processes such as spontaneous parametric down conversion, intensity modulation of electromagnetic field and spontaneous four wave mixing.

1.3.1 Nonlinear wave equation

It is well known that electromagnetic waves are composed of an electric field and a transverse polarization magnetic field. When optical probes are used for the study of materials, a polarisation is therefore induced in the latter.

In linear optics, the induced dipole moment p (physical unit: C.m) can be modelled by an equation taking into account only the action of the electric field E (physical unit: V/m) [28]:

$$\vec{p} = \varepsilon_0 \alpha \vec{E} \tag{1.1}$$

where ε_0 is the permittivity of the vacuum, α (physical unit: m^3) is defined as the electrical polarisability of the atom of the molecule. This is generally written in the form of a tensor of rank *2* because the induced dipole moment is not necessarily oriented in the direction of the applied electric field, which gives:

$$\begin{bmatrix} p_x \\ p_y \\ p_z \end{bmatrix} = \varepsilon_0 \begin{bmatrix} \alpha_{xx} & \alpha_{xy} & \alpha_{xz} \\ \alpha_{yx} & \alpha_{yy} & \alpha_{yz} \\ \alpha_{zx} & \alpha_{zy} & \alpha_{zz} \end{bmatrix} \begin{bmatrix} E_x \\ E_y \\ E_z \end{bmatrix} \tag{1.2}$$

When one considers a more general expression involving the N atoms constituting the material, one obtains the polarization P (physical unit: C/m^2) induced by the electric field applied and defined by the combination of all the dipole moments induced p (per unit volume):

$$\vec{P} = \varepsilon_0 \chi \vec{\mathrm{E}} \tag{1.3}$$

where χ (without physical unit) is defined as the electrical susceptibility of the material. It is also a tensor of rank *2*.

Let us now turn to the relations between polarization and the electric field in the context of non-linear optics. Mathematically, the expressions (1.1) and (1.3) are only developments in series with respect to the electric field, limited to the first order. When the electric field becomes important, that is to say of the order of magnitude of the Coulomb field in the atom, we can no longer neglect the terms of higher order as in linear optics. Therefore, expressions (1.1) and (1.3) can be rewritten in the form of n-term series including the total polarisability and susceptibility of the atom and the material [28]:

$$\begin{aligned} \vec{\mathrm{p}} &= \varepsilon_0 \alpha \vec{\mathrm{E}} + \varepsilon_0 \beta \vec{\mathrm{E}} \times \vec{\mathrm{E}} + \varepsilon_0 \gamma \vec{\mathrm{E}} \times \vec{\mathrm{E}} \times \vec{\mathrm{E}} + \ldots \\ \vec{P} &= \varepsilon_0 \chi^{(1)} \vec{\mathrm{E}} + \varepsilon_0 \chi^{(2)} \vec{\mathrm{E}} \times \vec{\mathrm{E}} + \varepsilon_0 \chi^{(3)} \vec{\mathrm{E}} \times \vec{\mathrm{E}} \times \vec{\mathrm{E}} + \ldots \end{aligned} \tag{1.4}$$

where β *(m^4/V)* and γ *(m^5/V^2)* are the second and third order hyperpolarisabilities of the atom. $\chi^{(2)}$ *(m/V)* and $\chi^{(3)}$ *(m^2/V^2)* correspond to the second & third order nonlinear susceptibilities of the material whose generalised notation is $\chi^{(n)}$, indicating the susceptibility of order n of the material, that is to say a tensor of rank *(n + 1)*. $\chi^{(2)}$ is therefore a tensor of rank *3* comprising *27* components. Indeed, looking at (1.4), it is found that each of the *3* components *(x, y, z)* of $\chi^{(2)}$ is related to each of the components *(x, y, z)* of *2* electric fields. All these components are not necessarily different and some may be equivalent or null according to the classes of symmetry that appear in one or the other physical system studied. We will discuss this important aspect in the description of the samples studied. However, this brief overview already gives us an idea of the advantage of the polarization of the electric field of the laser beams (magnetic transverse or "**p**" for a polarization parallel to the plane of incidence of the electric field, electric transverse or "**s**" for a polarization perpendicular to the plane of incidence of the electric field): this allows the specific characterisation of the components of the nonlinear susceptibility of the solids in different directions.

1.3.2 Second- order nonlinear ($\chi^{(2)}$) effects

Now we show why second-order nonlinear phenomena in materials require the non-centrosymmetry of their electronic properties. Indeed, suppose that we have a centrosymmetric material subjected to two electromagnetic fields, and consider the expression of the polarization of the second order on the two drawings of Figure 1.1:

$$\begin{aligned} \vec{P}_{NL} &= \varepsilon_0 \chi^{(2)} \vec{\mathrm{E}} \times \vec{\mathrm{E}} \\ \vec{P'}_{NL} &= \varepsilon_0 \chi^{(2)} \vec{\mathrm{E}'} \times \vec{\mathrm{E}'} \end{aligned} \tag{1.5}$$

Considering the geometry of the polarisation properties of the system on the Figure 1.1, the electric fields and the nonlinear polarizations satisfy the following conditions:

$$\begin{aligned} \vec{\mathrm{E}'}_{NL} &= -\vec{\mathrm{E}}_{NL} \\ \vec{P'}_{NL} &= -\vec{P}_{NL} \end{aligned} \tag{1.6}$$

From which we write immediately by considering Equation (1.6):

$$\begin{aligned} \varepsilon_0 \chi^{(2)} \vec{\mathrm{E}} \times \vec{\mathrm{E}} &= -\varepsilon_0 \chi^{(2)} \vec{\mathrm{E}'} \times \vec{\mathrm{E}'} \\ \chi^{(2)} \vec{\mathrm{E}} \times \vec{\mathrm{E}} &= -\chi^{(2)} (-\vec{\mathrm{E}}) \times (-\vec{\mathrm{E}}) \\ \chi^{(2)} &= -\chi^{(2)} \\ \chi^{(2)} &= 0 \end{aligned} \tag{1.7}$$

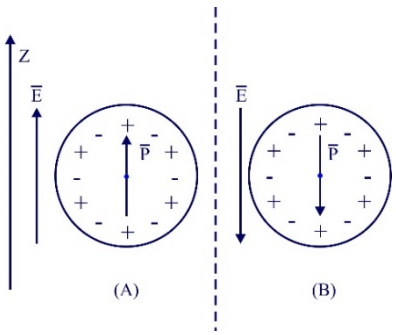

Figure 1.1 Diagrams illustrating the property of centrosymmetry in the electronic characteristics of a given system. The black dot in the centre of each circle is the symmetry inversion centre. (A): incident electric field oriented along the Z axis. (B): incident electric field oriented along -Z.

The only possible solution for the second-order nonlinear susceptibility is therefore zero in all directions, which means that centrosymmetric materials have no second order non-linear response in the electrical dipole approximation.

Non-centrosymmetric materials, which are less numerous, are used for particular applications. Some have been indispensable to the realisation of this thesis. These materials can generate different harmonics of higher order (2ω, 3ω, ...) or other non-linear phenomena such as frequency sum or difference generation.

We have seen that the study of the nonlinear susceptibility $\chi^{(2)}$ involved the components of two electric fields. From the experimental point of view, there are two laser beams. Let's to consider the case of two waves polarized in the same direction Z and propagate in the direction of the axis X as can be seen in Figure 1.2. Let us limit ourselves to the computation of the components of the polarization along the propagation axis X of the incident waves [28].

By taking the electrical components of the two incident waves of frequencies ω_1 and ω_2 in Figure 1.2:

$$\begin{aligned} \vec{E}_1 &= \vec{E}_{1z} = E_{0_1} \cos(\omega_1 t) \\ \vec{E}_2 &= \vec{E}_{2z} = E_{0_2} \cos(\omega_2 t) \end{aligned} \tag{1.8}$$

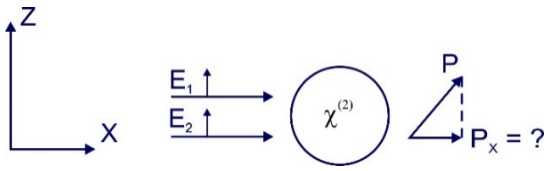

Figure 1.2 Diagram illustrating the computation of the polarization component of the molecule in the X direction for two electric fields polarized along the Z direction.

We write the X component of the polarisation field based on the Equation (1.4) and considering just the second order nonlinear part:

$$\begin{aligned} P_x = \varepsilon_0 \chi_{xz}^{(1)} (E_{1z} + E_{2z}) + \varepsilon_0 \chi_{xzz}^{(2)} (E_{1z} + E_{2z})^2 = \\ \varepsilon_0 \chi_{xz}^{(1)} E_{01} \cos(\omega_1 t) + \varepsilon_0 \chi_{xz}^{(1)} E_{02} \cos(\omega_2 t) \\ + \varepsilon_0 \chi_{xzz}^{(2)} E_{01}^2 \cos^2(\omega_1 t) + \varepsilon_0 \chi_{xzz}^{(2)} E_{02}^2 \cos^2(\omega_2 t) \\ + 2\varepsilon_0 \chi_{xzz}^{(2)} E_{01} E_{02} \cos(\omega_1 t) \cos(\omega_2 t) \end{aligned} \tag{1.9}$$

By some trigonometric manipulation and consider only the non-linear component of the second-order polarization, we obtain:

$$\begin{aligned} P_x^{(2)} = \frac{\varepsilon_0}{2} \chi_{xzz}^{(2)} [E_{01}^2 + E_{02}^2] + \frac{\varepsilon_0}{2} \chi_{xzz}^{(2)} [E_{01}^2 \cos(2\omega_1 t) + E_{02}^2 \cos(2\omega_2 t)] \\ + \varepsilon_0 \chi_{xzz}^{(2)} [E_{01} E_{02} \cos(\omega_1 t + \omega_2 t)] + \varepsilon_0 \chi_{xzz}^{(2)} [E_{01} E_{02} \cos(\omega_1 t - \omega_2 t)] \end{aligned} \tag{1.10}$$

We have therefore four contributions associated with this particular component of the susceptibility:

- Optical rectification (OR), which corresponds to the generation of DC polarisation;
- Second Harmonic Generation (SHG), when we have $2\omega_1$ or $2\omega_2$;
- Sum-Frequency generation (SFG), $\omega_3 = \omega_1 + \omega_2$ generated;
- Difference frequency generation (DFG), $\omega_3 = \omega_1 - \omega_2$ generated.

We can now derive an evolution equation for the fields, starting from Maxwell's equations which govern all electromagnetic phenomena for the electric field *E (r,t)*, the electric displacement *D (r,t)*, the magnetic field *B (r,t)* and the magnetic field *H (r,t)*:

$$\begin{aligned} \nabla \times E &= -\frac{1}{c}\frac{\partial B}{\partial t} \\ \nabla \times B &= \frac{1}{c}\frac{\partial D}{\partial t} \\ \nabla \cdot D &= 0 \\ \nabla \cdot B &= 0 \end{aligned} \tag{1.11}$$

where $B = H + 4\pi M$ and $D = E + 4\pi P$.

One can write the P as:

$$P = P_L + P_{NL} \tag{1.12}$$

where P_L is the part of the electric dipole polarization linear in the field amplitude and P_{NL} is the nonlinear part of this polarization.

For an isotropic and dispersionless material, the wave equation can be written as [28]:

$$\nabla^2 \mathrm{E} - \frac{\varepsilon^{(1)}}{c^2}\frac{\partial^2 \mathrm{E}}{\partial t^2} = \frac{1}{\varepsilon_0 c^2}\frac{\partial^2 P_{NL}}{\partial t^2} \tag{1.13}$$

The solution of the wave equation for the plane wave with the absence of the nonlinear source can be written as:

$$\mathrm{E}(z,t) = Ae^{i(kz-\omega t)} + c.c \tag{1.14}$$

where A is a constant and is the amplitude of the field, z is the propagation direction and k is the wave-vector, which can be defined by:

$$k = \frac{n\omega}{c} \tag{1.15}$$

In the case of DFG, we can substitute Equation (1.14) in Equation (1.13) and replace the Laplace operator by d^2/dz^2 as the field propagates along z axis:

$$\frac{d^2 A_3}{dz^2} + 2ik_3 \frac{dA_3}{dz} = \frac{-2\chi^{(2)}\omega_3^2}{c^2} A_1 A_2 e^{i(k_1 - k_2 - k_3)z} \tag{1.16}$$

Here index 3 corresponds to the idler, while index 1 and 2 correspond to the pump and seed.

By considering the slowly varying amplitude approximation one can neglect the first component in the left-hand side of Equation. (1.16):

$$\left| \frac{d^2 A_3}{dz^2} \right| \ll \left| k_3 \frac{dA_3}{dz} \right| \tag{1.17}$$

Now one can write:

$$\frac{dA_3}{dz} = \frac{2id_{eff}\omega_3^2}{k_3 c^2} A_1 A_2 e^{i(k_1 - k_2 - k_3)z} \tag{1.18}$$

One can also write:

$$\begin{aligned} \frac{dA_1}{dz} &= \frac{2id_{eff}\omega_1^2}{k_1 c^2} A_3 A_2^* e^{-i\Delta k z} \\ \frac{dA_2}{dz} &= \frac{2id_{eff}\omega_2^2}{k_2 c^2} A_3 A_1^* e^{-i\Delta k z} \end{aligned} \tag{1.19}$$

where Δk is the wave-vector mismatch and for DFG can be defined as:

$$\Delta k = k_1 - k_2 - k_3 \tag{1.20}$$

If the system will experience $\Delta k = 0$, this will define an ideal process, where the wave-vectors are matched. In this case the coherent length will tend to the infinity. This means the phase of the generated wave at any point of propagation along the nonlinear crystal will be the same as the first emitted wave in the nonlinear crystal at entrance. In other words, it means the amplitude of the emitted wave will increase proportionally to the length of the nonlinear crystal. This is clearly shown in the Figure 1.3. The straight line

corresponds to the condition of perfect phase matching. However, as was mentioned previously, $\Delta k = 0$ presents an ideal condition and in reality, one deals with quasi-phase matching Figure 1.3, which describes a case where the amplitude of the emitted field grows monotonically but not as fast as perfect matching conditions.

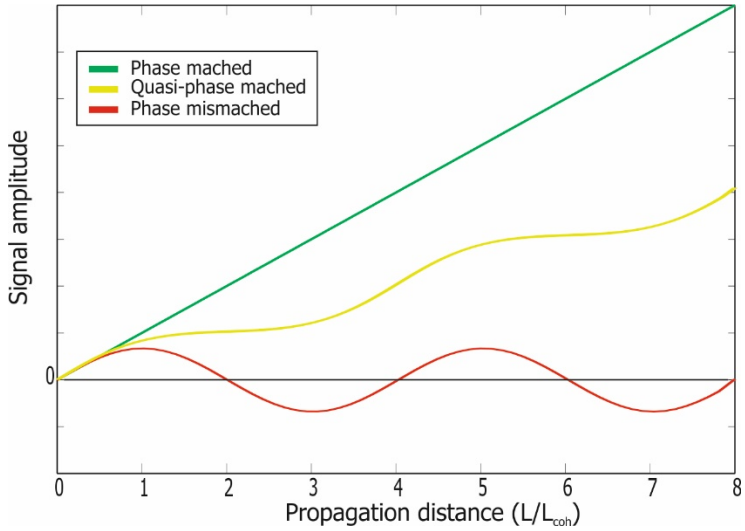

Figure 1.3 Spatial variation of three different scenarios for phase matching conditions. Green line corresponds to the ideal conditions, where wave-vectors are equal. Yellow line demonstrates the quasi-phase matched conditions. In this case the raise of the amplitude of the generated field is less than the perfect phase matching condition, but it still increases fast enough along the propagation axis. The red line presents the lack of phase matching condition.

By integrating the Equation (1.18) from z=0 to z=L, the amplitude of the idler is expressed as :

$$A_3 = \frac{2id_{eff}\omega_3^2 A_1 A_2}{k_3 c^2}\left(\frac{e^{i\Delta kL}-1}{i\Delta k}\right) \tag{1.21}$$

This solution leads to the intensity of the signal:

$$I_3 = \frac{8n_3\varepsilon_0 d_{eff}^2\omega_3^4 |A_1|^2 |A_2|^2}{k_3^2 c^3}\left|\frac{e^{i\Delta kL}-1}{\Delta k}\right|^2 \tag{1.22}$$

The square modulus in the right hand side of the Equation (1.22) can be expressed as:

$$\left|\frac{e^{i\Delta kL}-1}{\Delta k}\right|^2 = L^2\mathrm{sinc}^2(\Delta kL/2) \tag{1.23}$$

In an ideal system, when the phase matching condition is satisfied $(\Delta k \to 0)$ one can write the Equation (1.22) as:

$$I_3 = \frac{8\varepsilon_0 d_{eff}^2 \omega_3^2 I_1^{\,2} I_2^{\,2}}{n_1 n_2 n_3 \varepsilon_0 c^3} L^2 \tag{1.24}$$

where I_1 and I_2 are the pump and seed intensity. In stimulated (classical) nonlinear optical process we should have both pump and seed in order to generate the signal at ω_3.

1.3.3 Quantum explanation of three wave mixing

Equation (1.21) clearly shows that if one removes the seed *(A_2=0)* and keeps just the pump, the signal intensity will be zero. According to the equations, except for the pump field, we do not expect to generate any other field. However, experiments show new fields generate. In this process, the momentum and energy conservation are still satisfied. It is exactly the situation, where classical physics cannot describe nonlinear processes like Spontaneous Parametric Down Conversion (SPDC). This is the nonlinear process similar to DFG, where instead of having pump and seed field, one removes seed and keeps just the pump and measures a new signal at ω_3 and ω_2. In this process photons are created from the vacuum state and quantum fluctuations replace the second input field, which is considered in classical model. Hence, the generation of new fields is still possible if one will keep the pump field and remove the second field in the input. In quantum field theory, this process is referred as spontaneous as it is generated from quantum vacuum fluctuations, parametric because of the phase relationship between input and output fields and down-converted as a pair of photons is generated as the result of annihilation of a photon at higher energy level. Figure 1.4 shows the schematic view of the DFG and SPDC.

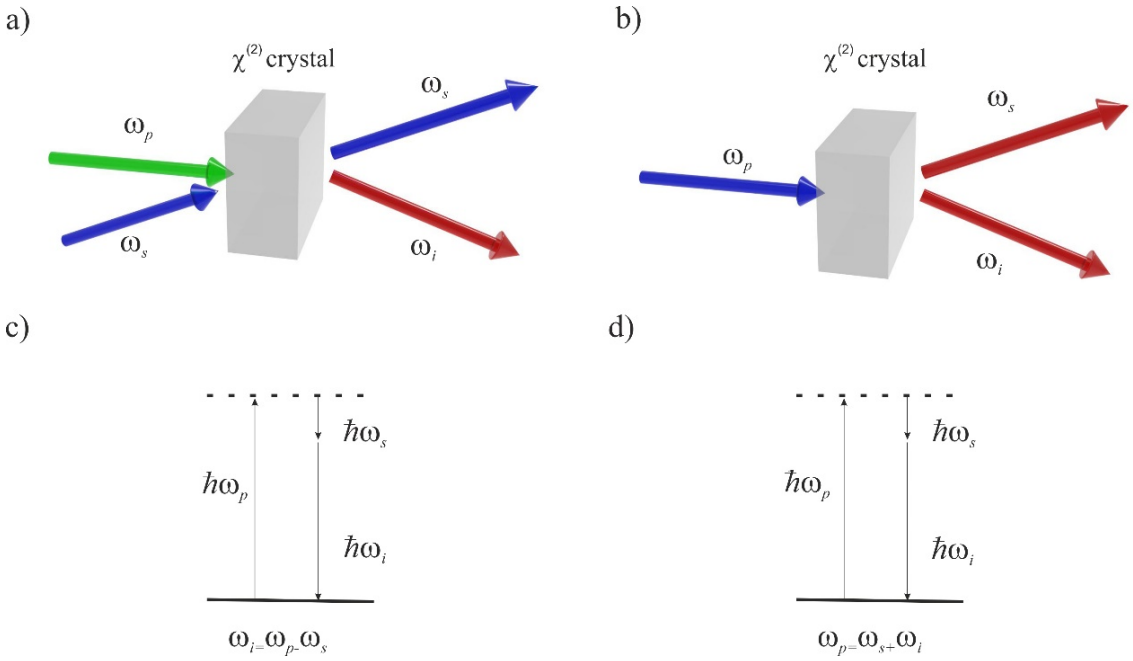

Figure 1.4 An illustration of DFG in a $\chi^{(2)}$ crystal (a), an illustration of SPDC in a $\chi^{(2)}$ crystal (b), energy conversion in DFG process (c), energy conversion in SPDC process (d).

The SPDC generation can be considered as the result of the amplification of vacuum fluctuations [29]. The rough classical estimation to this amplification can be considered as:

$$P_{SPDC} \approx \hbar\omega G_2(z)\frac{c}{2\Delta nz} \tag{1.25}$$

where $G_2(z)$ corresponds to the gain and $c/2\Delta nz$ corresponds to the bandwidth. A more precise method of the estimation of the SPDC power is the experimental measurement in a setup like Figure 1.5 [28], [30]. One can classically treat this phenomenon if the zero-point energy of the electromagnetic modes bring a sufficient input seed intensity equivalent to one photon per mode. Hence, by assuming that there is one idler photon per mode in the quantising volume V, the effective idler intensity can be defined as:

$$dI_i = \frac{dN_1 \hbar\omega_i c}{Vn_1} \tag{1.26}$$

where dN_1 corresponds to the number of modes between θ and $d\theta$ (θ is the angle between k vectors of signal and idler).

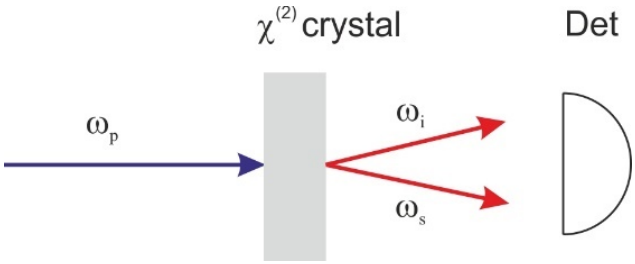

Figure 1.5 Schematic view of the setup for SPDC brightness measurement.

Here we aim to present the calculation of the SPDC brightness, as we use it for the estimation of the number of generated photons in Appendix I. The full approach of this calculation is beyond of this thesis and can be found in [31]. In this calculation, just one polarisation is considered for each field. Here is the field operator for the signal [32]:

$$E_{signal} = \frac{1}{2}[\hat{E}_s(x,t) + \hat{E}_s^{\dagger}(x,t)] \tag{1.27}$$

where $\hat{E}_s$ is the positive-frequency part. The interaction Hamiltonian for the SPDC process is determined by:

$$\hat{H}_I = -\frac{\varepsilon_0}{2} d_{eff} \int_v d^3x \{\hat{E}_p(x,t)\hat{E}_s^{\dagger}(x,t)\hat{E}_i^{\dagger}(x,t) + H.c.\} \tag{1.28}$$

where d_{eff} corresponds to the effective nonlinear susceptibility of the crystal. The Fermi's Golden Rule is used for as initial equation in order to calculate the signal power. According to Fermi's Golden Rule, the rate of the transition rate from initial state $|a\rangle$ to the final state $|b\rangle$ is given by [32]:

$$W = \frac{2\pi}{\hbar} \left| \langle b | \hat{H}_I | a \rangle \right|^2 \rho_b \tag{1.29}$$

where $\left| \langle b | \hat{H}_I | a \rangle \right|$ is the transition matrix element and ρ_b is the density matrix element of the final state. This formula assumes that the initial state contains just one pump photon and the final state consists of one signal and one idler photon. Energy conservation conditions are satisfied and the pump can be considered to be with a single frequency. The emitted signal power in the frequency interval, $d\omega_s$ and element d^2K_s can be obtained by multiplying Equation (1.29) by $\hbar\omega_s$ and integrating over unobserved idler transverse wave vector K_i:

$$dP_s = \hbar\omega_s \cdot d\omega_s \cdot \int W d^2K_s \tag{1.30}$$

where d^2K_s element is obtained by:

$$d^2K_s = \bar{k}_s^2 d^2u_s \tag{1.31}$$

where $\bar{k}_s$ is the wave vector of signal for the value of signal frequency for which the crystal is collinearly phase matched and u_s corresponds to the angle of wave vector in the crystal with respect to the z axis. This integration in the case of type II SPDC leads to the differential signal power [31]:

$$\delta P_s = \frac{\hbar d_{eff}^2 L\omega_s^3\omega_i^2}{\pi c^3 \varepsilon_0 n_p^2 \omega_p} P_p \delta\omega_s = (2\pi)^4 \frac{2\hbar c d_{eff}^2 L\lambda_p}{\varepsilon_0 n_p^2 \lambda_s^5 \lambda_i^2} P_p \delta\lambda_s \tag{1.32}$$

where $L, \omega_s, \omega_i, \omega_p$ and n_p correspond to the crystal length, signal frequency, idler frequency, pump frequency and refractive index at pump frequency. λ_s, λ_i and λ_p correspond to the wavelength of signal, idler and pump respectively.

DCE photon generation in $\chi^{(2)}$ crystals

As we mentioned in section 1.3, any oscillation of the boundary condition in time, is potentially an analogue of DCE and can lead to the emission of correlated photon pairs at a frequency which is a function of the oscillation frequency. This emission should also satisfy the energy conservation conditions. The idea of the modulation of the refractive index in time, which is equivalent to the effective length modulation were theoretically considered in the literature in [9], [20], [21], [33]–[35].

Here we consider the proposal of the type-I optical parametric oscillator (OPO) and design an experiment, where the SPDC from a thin nonlinear crystal with non-centrosymmetric structure at a subwavelength thickness $(L_{crystal} \leq 0.1\lambda_{pump})$ can be considered as an optical analogy for DCE [35]. In chapter two we discuss experimental realisation of this proposal by using 2D non-centrosymmetric crystal. Figure 1.6 demonstrates the schematic view of the OPO with a thin nonlinear crystal. Thickness of the nonlinear crystal plays a vital role to make it possible to consider the SPDC emission, which occurs because of the vacuum fluctuation from the $\chi^{(2)}$ crystal as DCE radiation.

The fact of using the OPO cavity in this proposal is to amplify the emitted SPDC signal and the SPDC signal by itself is the DCE emission [35].

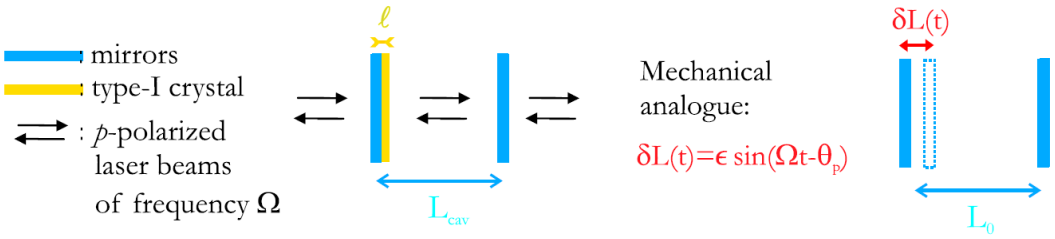

Figure 1.6 Schematic view of the optical parametric oscillator with a second order nonlinear medium in the left land side mirror [35].

The OPO system can be described by the Maxwell equations. As a $\chi^{(2)}$ crystal will be used in this system under the action of an intense beam, the second order nonlinear part of the polarisation should be considered in the polarisation and wave equation. For an intense beam one can write the polarisation vector:

$$\vec{P} = \varepsilon_0 \chi^{(1)} \vec{E}_p + \vec{P}_{NL} \tag{1.33}$$

where E_p corresponds to the electric field of the pump and nonlinear polarisation P_{NL} can be described by the interaction of the pump field and electric field of the seed (vacuum fluctuations):

$$\vec{P}_{NL} = \frac{\varepsilon_0}{2} \chi^{(2)} \vec{E}_p \times \vec{E}_s \tag{1.34}$$

where E_s corresponds to the electric field of the seed (vacuum fluctuation). One can write the pump electric field inside the crystal:

$$E_p = E_0 e^{i\theta_p} e^{-i\omega_p (t - n_p(\omega_p) x/c)} + c.c. \tag{1.35}$$

where θ_p corresponds to the pump phase at $x=0, \omega_p, n_p(\omega_p)$ and E_0 correspond to the pump frequency, refractive index of the crystal at pump frequency along the pump polarisation and field amplitude respectively. One can write the polarisation vector for the perpendicular direction to the pump polarisation as:

$$\vec{P_s} = \varepsilon_0 \chi_{eff} \vec{E}_s \tag{1.36}$$

With $\chi_{eff} = \overline{\chi^{(1)}} + \kappa \sin[\omega_p(t - \overline{n_p}x/c) - \theta_p]$, where $\kappa = E_{0_p}\overline{\chi^{(2)}}$ and $\overline{n_p}$ corresponds to the mean value of the refractive index along the pump polarisation. $\overline{\chi^{(1)}}$ and $\overline{\chi^{(2)}}$ correspond to the mean value of first and second order nonlinear susceptibility respectively. We use the mean value based on the assumption that the crystal is non-absorbent and dispersion-free in the spectral range of interest.

Now if one will pump the crystal in the system illustrated in Figure 1.6 along ***p*** polarisation, the crystal will behave as a linear dielectric medium in ***s*** direction with an effective refractive index [35]:

$$n_s(x,t)^2 = \chi_{eff}(x,t) + 1 \tag{1.37}$$

By assuming that the mean value of refractive index $\overline{n} \simeq 1$, one can expand the refractive index to the first order of κ:

$$n_s(x,t) \simeq \overline{n_s} + \frac{\kappa}{2\overline{n_s}} \sin[\omega_p(t - \overline{n_p}x/c) - \theta_p] \tag{1.38}$$

Based on the initial assumption regarding the crystal length (l) in comparison to the pump wavelength, the spatial dependence of the refractive index becomes negligible and one can consider just the temporal dependence of the refractive index:

$$n_s(t) = \overline{n_s} + \frac{\zeta_{opt}}{l} \sin[\omega_p(t) - \theta_p] \tag{1.39}$$

with $\zeta_{opt} \simeq \frac{l}{2\overline{n_s}} E_{0_p}\overline{\chi^{(2)}}$.

This temporal modulation of the refractive index is exactly the key condition of the DCE emission, which leads to the temporal modulation of the effective crystal length. In OPO this leads to the modulation of the effective length of the cavity. In this case SPDC from the crystal can be considered as the generation of photon pairs from vacuum state as the result of the temporal modulation of the effective length, which is the definition of the DCE.

1.3.4 Third-order nonlinear ($\chi^{(3)}$) effects

As can be seen from the Equation (1.4) the polarisation is written as a Taylor expansion, where the third part of this equation corresponds to the third order nonlinear effects. In contrast to the second order nonlinear effects, which are not expected from centrosymmetric materials, this class of nonlinearity is measurable regardless of the spatial symmetry of the material. The third order nonlinear susceptibility is the lowest order nonlinearity for the centrosymmetric materials, while all of the even-order nonlinear susceptibilities are equal to zero, based on the same principle as in Figure 1.2.

In this thesis, we consider two third-order nonlinear optical phenomena, self-phase modulation (SPM) and four-wave mixing (FWM).

Self-phase modulation in a ($\chi^{(3)}$) nonlinear medium

One of the important classes of nonlinear optical effects is the class of self-actions associated with the change in the refractive index of the medium as a result of the nonlinear polarization induced by the field of the light wave. The self-action of light waves is caused by the real component of the non-linear susceptibilities $Re\,\chi^{(3)}$.

Self-focusing is one of the examples of self-action nonlinear phenomena. The corresponding expression for the refractive index of a nonlinear medium follows from Equation (1.4) [28]:

$$n\ (\omega, E)\ = n(\omega) + n_{NL} E^2 \tag{1.40}$$

where n is the linear, and n_{NL} is the nonlinear part of the refractive index. The quantity n_{NL} in the general case is a complex function, the form of which is determined by the specific mechanism of the nonlinear response of the medium. In the simplest case, the nonlinear part of the refractive index can be represented in the form [28]:

$$n_{NL}\, E^2 = n_2 I \tag{1.41}$$

where

$$n_2 = \left(2\pi / n_0\right)^2 \chi^{(3)} \tag{1.42}$$

Self-phase modulation is a nonlinear effect that arises from the dependence of the refractive index on the radiation intensity and consists of the appearance of a self-

induced phase shift, which a light pulse acquires when propagating in a nonlinear medium. This leads to a symmetric spectral broadening of optical pulses. The nonlinear phase shift of the pulse in the medium after traveling the distance of the L, can be defined as [36]:

$$\Phi(t) = \frac{\omega}{c} n_2 I(t) L \tag{1.43}$$

The time dependence of the emitted light intensity makes the nonlinear phase shifting a time dependent function, which gives rise to the time-dependent frequency shift [36]:

$$\Delta\omega(t) = \frac{\omega}{c} n_2 L \frac{\partial I}{\partial t} \tag{1.44}$$

The resulting maximum frequency broadening can be defined as:

$$\Delta\omega = \frac{\omega}{c} n_2 L \frac{I_0}{\tau} \tag{1.45}$$

where I_0 is the peak intensity and τ is the pulse duration [36].

Figure 1.7 demonstrates a typical SPM for a sech-shaped pulse with τ=*30 fs* in a fused silica optical fibre.

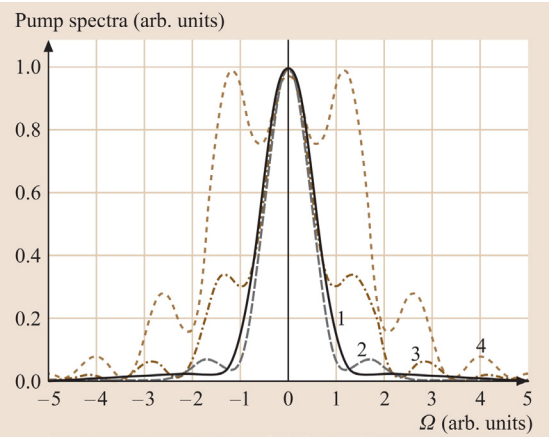

Figure 1.7 Typical SPM of a sech-shaped laser pulse with an initial pulse width of 30 fs in a fused-silica optical fibre with $n_2 = 3.2 \times 10^{-16}$ cm^2/W. Curve 1 presents the input spectrum of the pulse. The input pulse energy (2) 0.1 nJ, (3) 0.2 nJ, and (4) 0.3 nJ [36].

This third order nonlinear effect becomes important when we discuss another experimental approach to the DCE in chapter three. In this approach, we use the spatial intensity modulation of the pump along the waveguide. According to the Equation (1.40)

this intensity modulation leads to spectral broadening along the propagation. SPM is not exactly the effect, that we are interested in but this is a common third order nonlinear effect and it is more likely that in order to be able to measure DCE photon pairs, we should measure the expected SPM. First this criterion is considered by us as a necessary condition as a proof of the experimental nonlinearity estimation. In chapter three, this effect is discussed with more details for our experimental case.

Classical four wave mixing (FWM) and Spontaneous four wave mixing (SFWM)

In a classical approach, FWM phenomenon is a third order nonlinear effect, which describes the generation of new frequencies as the result of mixing three frequencies (Figure 1.8).

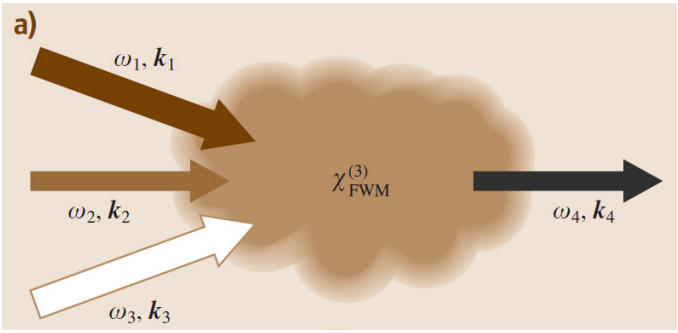

Figure 1.8 General type of FWM for $\chi^{(3)}$ crystal [36].

One can use Equation (1.4) to write the polarisation equation for FWM:

$$\vec{P} = \vec{P}_{linear} + \vec{P}_{NL} \tag{1.46}$$

where

$$\vec{P}_{NL} = \varepsilon_0 \chi^{(3)} \vdots \vec{E}_1 \vec{E}_2 \vec{E}_3 \tag{1.47}$$

The frequency of the new generated field will be defined as:

$$\omega_4 = \omega_1 \pm \omega_2 \pm \omega_3 \tag{1.48}$$

The general case, where we have three input electric fields and the interaction of these three fields in the $\chi^{(3)}$ crystal generates the new frequencies, is known as non-degenerate FWM. However, there is also possibility of new frequencies generation, when two frequencies coincide. This interaction is called “spontaneous FWM”. Figure 1.9 shows

the spontaneous FWM (SFWM). In this case the two new frequencies generate as the result of annihilation of two pump photons:

$$2\omega_p = \omega_s + \omega_i \tag{1.49}$$

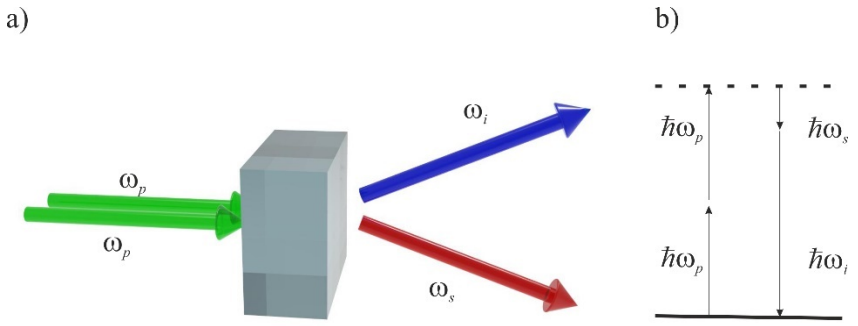

Figure 1.9 Spontaneous FWM as the result of annihilation of two pump photons (a), energy conversion of spontaneous FWM (b).

In chapter three we discuss an experimental approach to the DCE photon pairs generation from photonic crystal fiber with modulated dispersion. In this experiment the group velocity dispersion (GVD) is modulated along the fiber. This modulation of GVD leads to a modulation instability, which can be interpreted as SFWM in the spectral domain. In chapter three we establish the important criterion and conditions, where we can consider this spatial modulation along the waveguide or the fiber as temporal modulation of boundary conditions, which is the necessary and sufficient condition for DCE.

2 Transition Metal Dichalcogenides (TMDC) monolayer studies

2.1 Transition Metal Dichalcogenides (TMDC)

In 2004, the team of A. Geim at the University of Manchester highlighted the exceptional properties of graphene [37]. This major discovery showed that the thickness of a material could greatly influence its properties. This has increased the interest of researchers for two-dimensional (2D) crystals. There are many materials that can be isolated in the 2D form (Figure 2.1). Their properties are also very diverse. Among these 2D crystals, the family of TMDs (Transition Metal Dichalcogenides) has been studied extensively in the past few years because the associated materials have considerable potential for applications in nonlinear optics and electronics [38].

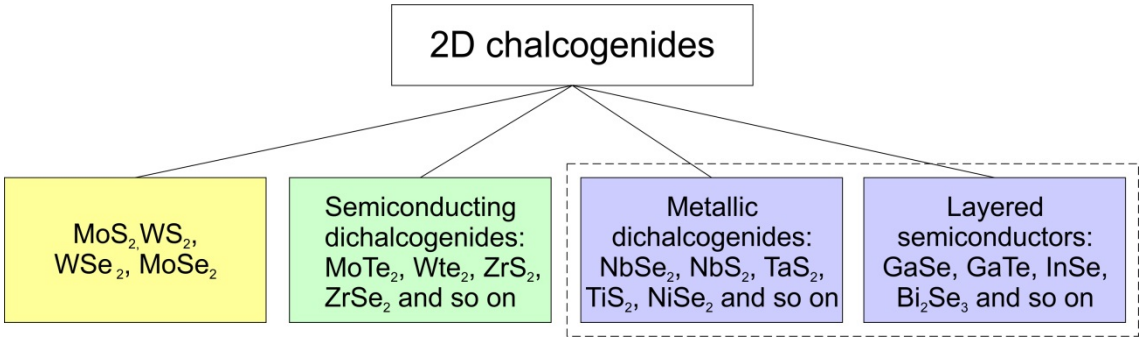

Figure 2.1 Table listing materials that can crystallize in the 2D form. In yellow, 2D crystals which are stable in air and at ambient temperature. In green, those which are probably stable in the air. In blue, those which are not stable in the air but which are probably stable under an inert atmosphere.

TMDs are a family of materials of the general formula MX_2, where M is a transition metal from group *4* to *10* (in the periodic classification of elements) and X is a chalcogenide (Figure 2.2). TMDs have different physical properties, ranging from superconductor to semiconductor (Table 2.1). From this group of TMDs, we are particularly interested in MoS_2.

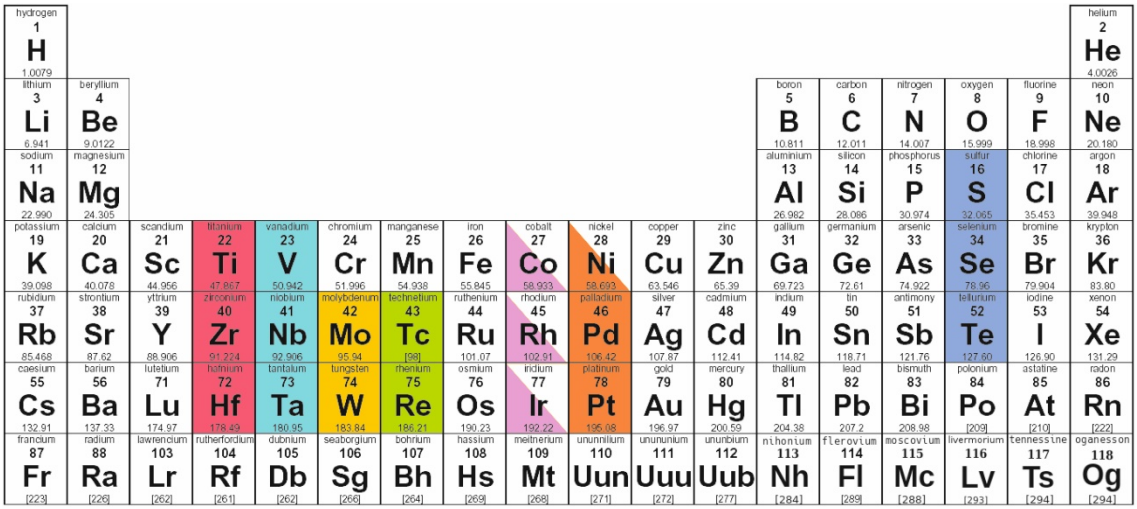

Figure 2.2 Mendeleev's periodic table of the elements on which the elements involved in the composition of 2D compounds of the TMD family are highlighted. The transition metals which crystallise in 2D form with the three chalcogens are completely coloured. Partially coloured transition metals only form 2D crystals with some of the chalcogens.

	-S_2	-Se_2	-Te_2
Mo	Semiconductor Monolayer: 1.8 eV Bulk: 1.2 eV	Semiconductor Monolayer: 1.5 eV Bulk: 1.1 eV	Semiconductor Monolayer: 1.1 eV Bulk: 1 eV
W	Semiconductor Monolayer: 1.9-2.1 eV Bulk: 1.2 eV	Semiconductor Monolayer: 1.7 eV Bulk: 1.2 eV	Semiconductor Monolayer: 1.7 eV
Ta	Metallic, superconductor	Metallic, superconductor	Metallic
Nb	Metallic, superconductor	Metallic, superconductor	Metallic

Table 2.1 Electronic properties of different TMDs, which can be prepared as 2D (monolayer) crystal.

2.2 Material structure of MoS_2

Molybdenum disulphide, a chemical compound of the formula MoS_2, is a naturally occurring crystal (Figure 2.3 (a)). Its structure has been known since the beginning of the 20th century [39]. It has a lamellar structure: it consists of a stack of layers each consisting of a plane of atoms of molybdenum situated between two planes of sulphur atoms; In each plane, the atoms are organized hexagonally (Figure 2.3 (b)). Within each layer, the atoms are covalently bonded, while the interlayer bonds are of the van der Waals type. This explains why the MoS_2 can be cleaved and that a monolayer of this material can be isolated. The isolation of a MoS_2 monolayer was first achieved in 1986 [40]. A monolayer of MoS_2 has a thickness of 0.65 nm [41]. The way in which the MoS_2 layers are stacked gives rise to three polytypes (Figure 2.3 (c)): the 1T and 3R polytypes are metastable whereas the most common naturally occurring polytype 2H is stable.

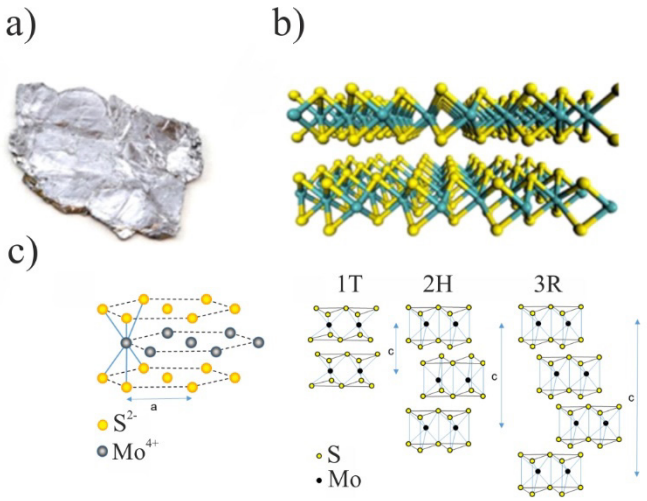

Figure 2.3 MoS_2 crystal (a). Diagram of a double layer of MoS_2 (b). Diagram of the structure of the different polytypes of MoS_2 (c).

2.3 MoS_2 monolayer Fabrication

There are different methods for MoS_2 monolayer fabrication. We will briefly discuss the most famous and popular methods.

2.3.1 Mechanical exfoliation

The first method is mechanical exfoliation. Due to the experimentally observed higher second order nonlinear susceptibility ($\chi^{(2)}$) response of the crystal from mechanically

exfoliated crystal in comparison to other methods, we decided to use this method of fabrication [42]. The reported value of $\chi^{(2)}$ for the mechanically exfoliated crystal is around $10^5\ pm/V$ while the $\chi^{(2)}$ for chemical vapor deposition (CVD) grown crystal is around $5\cdot10^3\ pm/V$ for SHG measured at the pump wavelength of *810 nm*. We also underline that this method of fabrication also limits us with the size of the monolayer crystal. The typical size of the fabricated monolayer with this method is between $5-20\mu m$ by $30-40\mu m$. The monolayers obtained by this method are in a limited number, of inhomogeneous thickness and distributed sparsely on the substrate.

In this method we use adhesive tape to separate a part of the bulk crystal. In order to do this, we take clean tape and then contact the sticky side of the tape with bulk crystal and add a little bit of pressure by cotton swab. We then use another clean part of the tape to contact with the other part of tape with crystals and again add gentle pressure with cotton swab. By then pulling the two tapes from each other we mechanically cleave the crystal step by step to fewer number of layers. We repeat the same procedure in order to increase the probability of obtaining monolayer crystals. We then we use a "sticky stamp", which is a soft double sided sticky layer of commercially available viscoelastic material (Gelpack) to transfer the crystals from a small area on the adhesive tape, where we expect to have a monolayer or few monolayer crystals with higher probability than other parts of the tape. We carefully place a small piece (roughly *5 mm* by *10 mm*) of the gel pad on a microscope slide. We then place the chosen part of the adhesive tape on the gel pad and gently add pressure with a cotton swab. We follow this procedure by holding down the corner of the gel pad and quick pulling off the tape from the gel stamp. Then this gel stamp is studied carefully under *50 x* Zeiss microscope to visibly identify the monolayer crystal and measure the size of the crystal. For further investigation of the crystal, it is very important to make sure that the microscope works in both back scattering and transmission modes. Later we present a method for the optical identification of the monolayer flakes based on the contrast of the illumination. It is also possible to carry out Raman spectroscopy and atomic force microscopy (AFM) to identify the number of layers of the crystal. We found that the brightness and optical contrast study of the crystals is enough at this stage to identify the monolayer crystals and distinguish them from bilayer and few-layer samples. We also discovered that the immediate transferring of the crystal from the adhesive tape to the gel pad after exfoliation is critically important for making a high quality sample. We confirm that the freshly transferred samples are more stable in

signal emission during experiments. After the identification of the monolayer crystal, the next step, which is the most delicate part of the process, is the deposition (transferring) of the fabricated monolayer crystal to the target substrate. In Appendix IV, we discuss about the choice of different types and structures of substrate. By using different methods, such as laser writing or scratching with diamond, we make a map on the substrate in order to track the crystal on the substrate easily during experiment. We fix the target substrate by strong double side tape on a heavy platform, which is placed on the 3D (x-y & rotation) stage. The microscope slide with the gel pad is placed upside down on the 3D (x-y-z) stage shown in Figure 2.4. At this point we need to find the crystal by using microscope and bring it to the marked part of the substrate where we want to transfer the crystal. After that we gently reduce the height of the microscope slide and step by step bring it to the substrate. It is very important to reduce the distance slowly and it is very clear when the stamp starts to touch the substrate surface. It is very important to give the crystal a minute to relax on the substrate. Because of the Van der Waals force the crystal will stick on the substrate. The final stage is to gently detach the stamp from substrate.

Figure 2.5 (b) presents our largest sample $100\mu m \times 50\mu m$, which was mechanically exfoliated.At this point, our sample is ready for inspection by atomic force microscope (AFM). We use this method to be sure about the number of layers of the crystal. Notwithstanding that the optical inspection is a confident method for us to make sure about the number of layers, we use AFM inspection as an additional check. Figure 2.5 (c) demonstrates a typical AFM result for one of our samples.

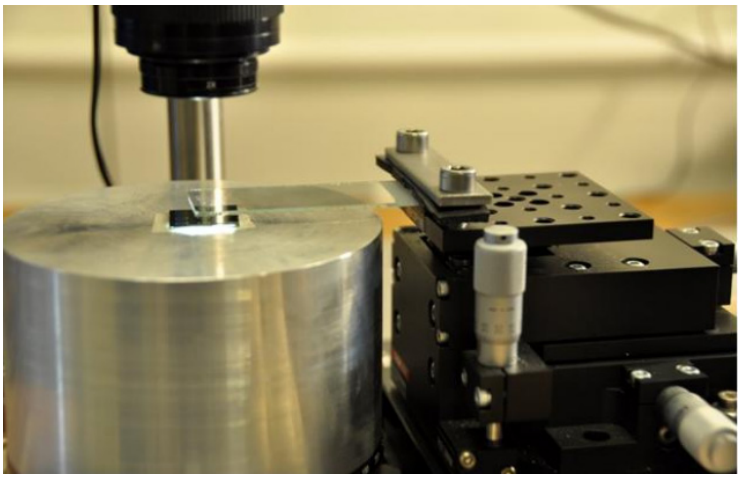

Figure 2.4 Combination of X-Y and rotational stage (left hand side) with linear X-Y-Z translation stage (right hand side) for flake transfering from gelpad to substrate.

There are also other methods to produce a large area of MoS_2 monolayer: liquid exfoliation associated with a filtration or spin coating type deposition method, direct sulphurization of films containing molybdenum-containing compounds [43]–[45] and deposition Chemical vapor deposition (CVD) [42], [46], [47]. We will briefly describe CVD method of fabrication as this method is the alternative method of fabrication of the MoS_2 monolayer for optical purposes.

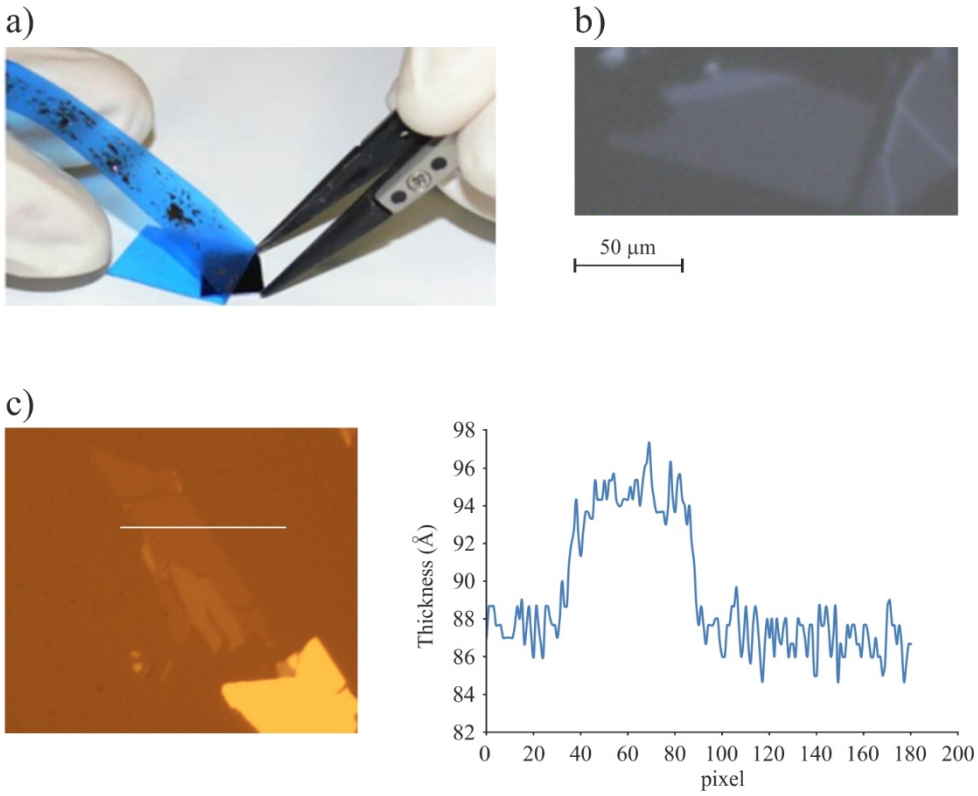

Figure 2.5 Photograph illustrating the mechanical exfoliation technique of MoS_2 (a), large mechanically exfoliated crystal (b), AFM image of a mechanically exfoliated MoS_2 sheet (c).

2.3.2 Chemical vapor deposition (CVD)

Chemical vapor deposition (CVD) is the reaction in the gas phase of precursors containing molybdenum and sulphur. In general, elemental sulphur and molybdenum trioxide (MoO_3) are used. The schematic of an oven typically used for MoS_2 CVD growth is shown in Figure 2.7. Generally, two different crucibles are used to arrange the MoO_3 and sulphur powders. Indeed, MoO_3 and sulphur have very different evaporation temperatures (*750 °C*. and *250 °C*. respectively): it is preferable to heat the two compounds at two

different temperatures so that the sulphur does not evaporate too soon. The substrate on which MoS_2 will grow is located above the MoO_3 crucible, face down. Heating of the furnace results in the evaporation of the precursors, which are transported by the carrier gas (typically argon or nitrogen) to the growth substrate. MoO_3 is reduced in the gas phase by sulphur to MoO_{3-x}. Sulphur and MoO_{3-x} then react on the surface of the substrate to form MoS_2.

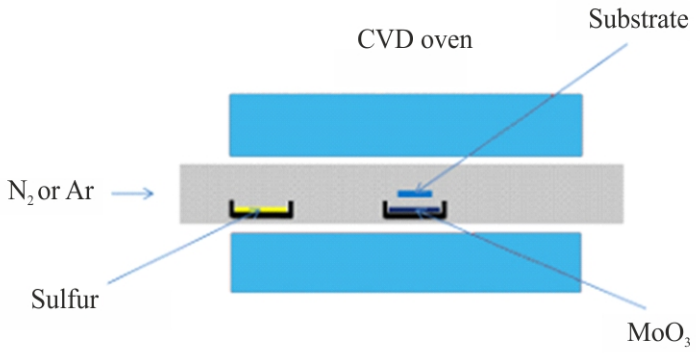

Figure 2.6 Schematic of a tubular furnace typically used for MoS_2 CVD growth [42].

Large areas of MoS_2 monolayers were obtained for the first time by this method in 2012 by the T.W team of Tunghai University of Taiwan (Figure 2.7) [42]. After characterizing the material by Raman spectroscopy and photoluminescence, they evaluated its electronic performance by making transistors based on this material. The transistor studied in the article has an I_{ON} / I_{OFF} ratio of *104* and a mobility of *0.02 cm²/(V.s)*. Despite a suitable I_{ON} / I_{OFF} ratio, mobility is well below those obtained from MoS_2 exfoliated. In order to get closer to the quality of the exfoliated MoS_2 sheets, it is necessary to optimize the growth parameters. However, the growth of MoS_2 is affected by numerous experimental parameters, notably:

- The temperature profile;
- The quantity of precursors and the ratio between the two quantities;
- The distance between the crucibles;
- The position of the substrates with respect to the precursor crucibles;
- The flow rate and the pressure of the carrier gas.

These parameters are also interdependent: for example, the distance between the crucibles influences the ratio of concentrations of the two precursors in the gas phase at the level of the growth substrate. Therefore, it is difficult to study one parameter independently of

the others. This complexity is also reflected in the literature by a set of experimental protocols that are very different but functional [42].

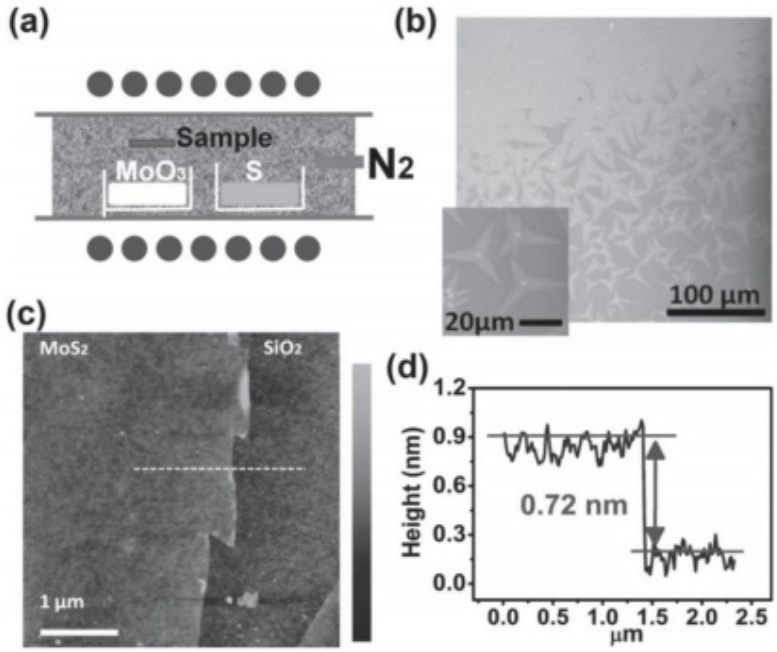

Figure 2.7 Diagram illustrating the CVD furnace used by the T.W. team at Tunghai University of Taiwan for the synthesis of MoS_2(a). Images under an optical microscope showing the synthesized MoS_2 domains (b). Atomic force microscopic image of a monolayer MoS2 domain (c). Height profile of the MoS_2 domain presented in (c) (d). Its thickness is *0.72 nm*. Figure from [42].

2.3.3 Visible contrast identification of monolayer up to few layers of MoS_2

Using the optical microscope is the most efficient and convenient way to identify monolayer flakes. However, identification of the monolayer flake from bilayer is not straightforward. To calculate the reflected light intensity and the optical contrast of the flakes the Transfer Matrix Method (TMM) can be used, which yields compact expressions for stacked optical media. We use this method for initial identification of monolayer flakes. Here we consider the slabs of the optical media stack along a horizontal axis, illuminated with a light beam at normal incidence. The transfer matrix *M* that relates the right going (a) and left going (b) wave amplitudes of the electromagnetic field at the start (in) and the end (out) of the stack of optical media is:

$$\begin{bmatrix} a_{in} \\ b_{in} \end{bmatrix} = M \begin{bmatrix} a_{out} \\ b_{out} \end{bmatrix} = \begin{bmatrix} m_{11} & m_{12} \\ m_{21} & m_{22} \end{bmatrix} \begin{bmatrix} a_{out} \\ b_{out} \end{bmatrix} \tag{2.1}$$

In order to simplify the optical identification process, it is interesting to measure a quantity that does not depend on the illumination intensity I_0. The optical contrast C, also named Michelson contrast in the literature, between two objects (the bare substrate and the substrate with a MoS_2 flake on top) is defined as [41]:

$$C = \frac{I_{crystal} - I_{substrate}}{I_{crystal} + I_{substrate}} \tag{2.2}$$

Where $I_{crystal}$ and $I_{substrate}$ are the reflected intensity from the crystal and the substrate. This value is independent from the I_0. The coefficient of the reflected intensity R for a media stack is:

$$R = \left|\frac{b_{in}}{a_{in}}\right|^2 ; \quad I_{reflected} = R.I_0 , \tag{2.3}$$

where b_{in} is the amplitude of the reflected (right going) wave and a_{in} is the amplitude of the incident (left going) wave.

If the medium $j = N+1$ is semi-infinite then $b_{out} = 0$. Using Eq. 3.1 with $M = M_{flake}$ we find:

$$\frac{1}{R} = \left|\frac{a_{in}}{b_{in}}\right|^2 = \left|\frac{m_{11}a_{out}}{m_{21}b_{out}}\right|^2 , \tag{2.4}$$

Which gives:

$$R_{crystal} = \frac{I_{reflected}}{I_0} = \left|\frac{m_{21}}{m_{11}}\right|^2 \tag{2.5}$$

For the regions without a flake deposited, the Expression 3.5 is also valid with $M = M_{substrate}$. The optical contrast, Equation 2.2, can be now written as:

$$C = \frac{I_{crystal} - I_{substrate}}{I_{crystal} + I_{substrate}} = \frac{I_0(R_{crystal} - R_{substrate})}{I_0(R_{crystal} + R_{substrate})} = \frac{(R_{crystal} - R_{substrate})}{(R_{crystal} + R_{substrate})}, \tag{2.6}$$

We use s numerical code in MATHEMATICA to determine the optical contrast. This method works if the individual layers are thiner than the coherence length of the typical white light.

2.4 MoS_2 Optical properties characterisation

In this section, we present the characterisation of optical properties of MoS_2.

2.4.1 MoS_2 band-gap

The intrinsic band-gap of TMDCs is in the visible side of the spectrum and is tuneable with the number of layers, thus making this group of materials of interest for photonic applications. Molybdenum disulphide is the most extensively studied in among TMDC materials. MoS_2 is a semiconductor with a band gap whose width depends on the number of layers. It is *1.2 eV* for the bulk MoS_2 crystal [48]. The MoS_2 has a direct bandgap when it is in monolayer and indirect for two or more layers (Figure 2.8). The direct band gap is at point *K*. As for the indirect band gap, the top of the valence band is at point *Γ* while the bottom of the conduction band is midway between point *Γ* and the point *K*. When the number of MoS_2 layers decreases, the energy of the bottom of the conduction band increases due to quantum confinement, which causes the indirect / direct band gap transition. Due to this, MoS_2 monolayer strongly emits photoluminescence as reported in [49].

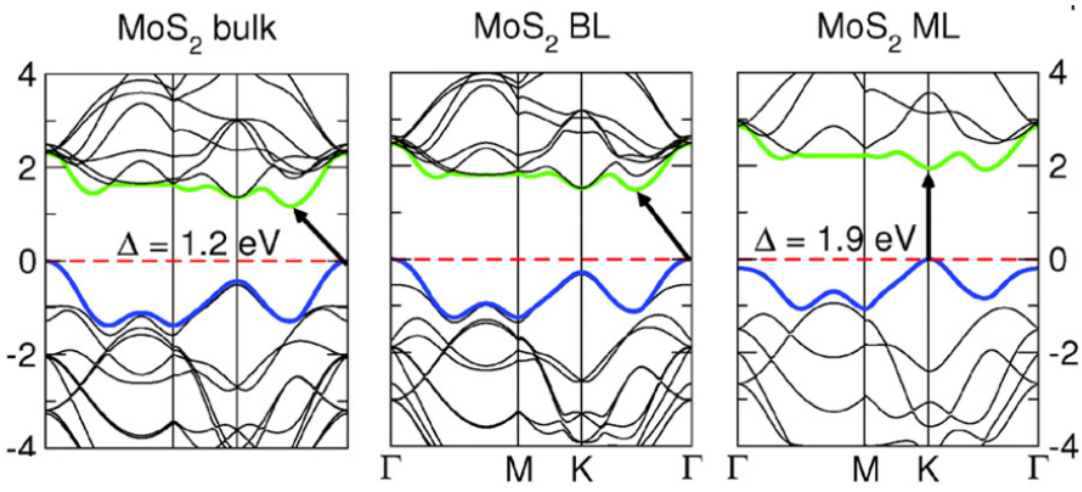

Figure 2.8 Band structures of bulk, bilayer and monolayer of MoS2 . Figure from [48].

2.4.2 Photoluminescence emission from MoS_2 monolayer

For the characterisation of MoS_2 monolayers the photoluminescence signal from the monolayer is measured. This measurement is performed with a CW laser source and we use and an Andor Technologies EMCCD camera integrated with the Andor Shamrock spectrometer. Figure 2.9 (a) shows the photoluminescence emission from the MoS_2

monolayer under blue (*405 nm*) and green (*532 nm*) CW excitation. Notwithstanding that the main peak around *684 nm* under blue pump looks broader than the peak around *675 nm* under green excitation, the shape of these two photoluminescence signals are very similar. These curves are background corrected. This background includes the photoluminescence from the objectives and other optical elements. Figure 2.9 (b) presents the photoluminescence emission from the substrate and other optical elements in the setup. We also performed a photoluminescence measurement under blue (405 nm) excitation in a cryogenic chamber at *4 K*. Figure 2.10 shows the results for this measurement. In this measurement, the crystal on a Fused Silica substrate is placed on the 3D (x-y-z) piezo stage with nanometre precision. We make a 3D map of the MoS_2 monolayer, where the colour corresponds to the signal intensity in given wavelength diapason in Figure 2.10 (a, b, c, d). By comparing (c) and (d), we see that the intensity of the photoluminescence signal is localised for different wavelengths and we see enhancement of the emission for different wavelengths from different parts.

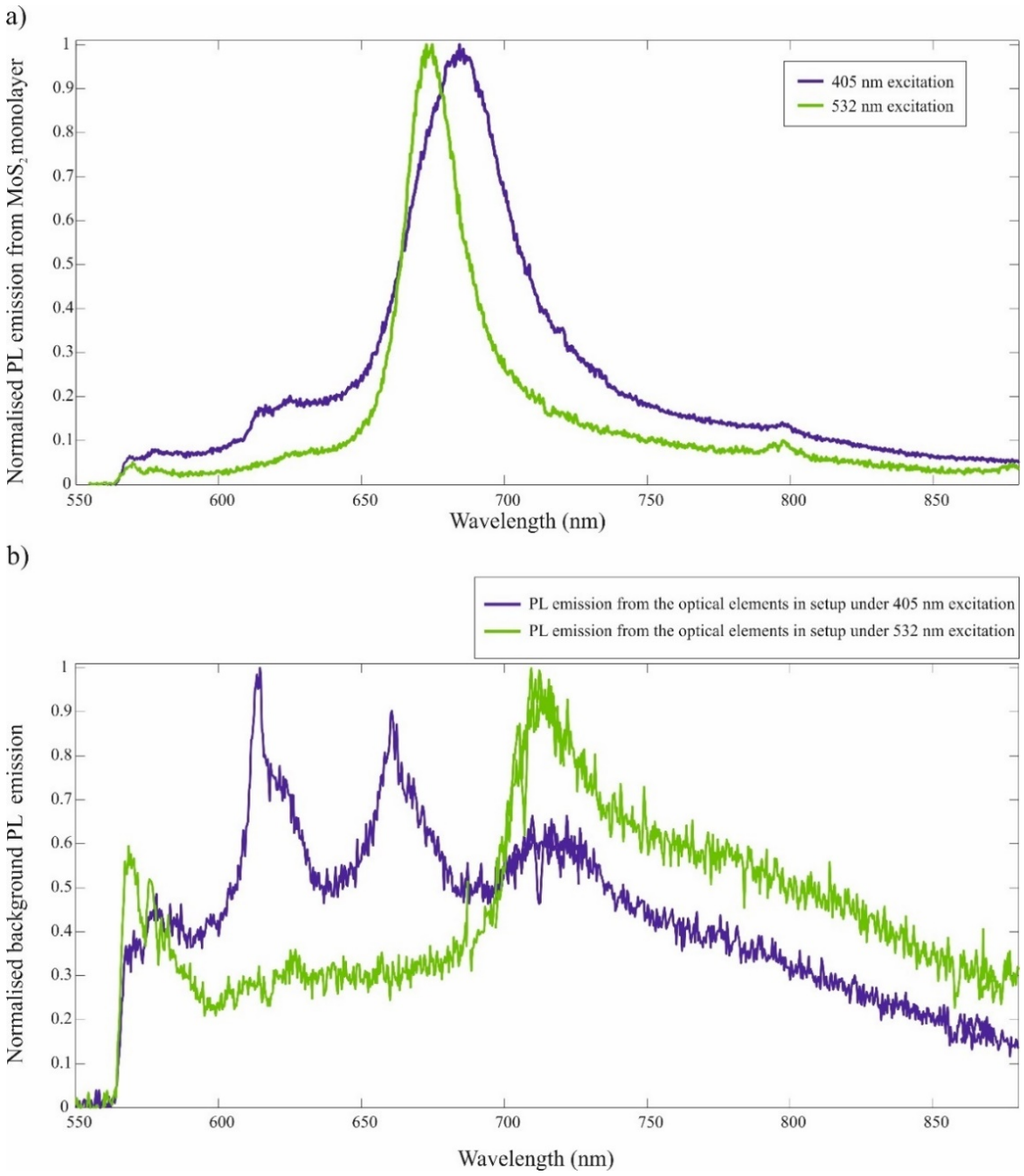

Figure 2.9 Photoluminescence emission from the MoS_2 monolayer. Green line corresponds to the signal under the 532 nm excitation and the blue line corresponds to the emitted signal from monolayer crystal under 405 nm pump. The pump power for both measurement was 10 mW (a). Photoluminescence emission from the optical elements in the setup. Green line corresponds to the signal under the 532 nm excitation and the blue line corresponds to the emitted signal from monolayer crystal under 405 nm pump. The pump power for both cases is 10 mW (b).

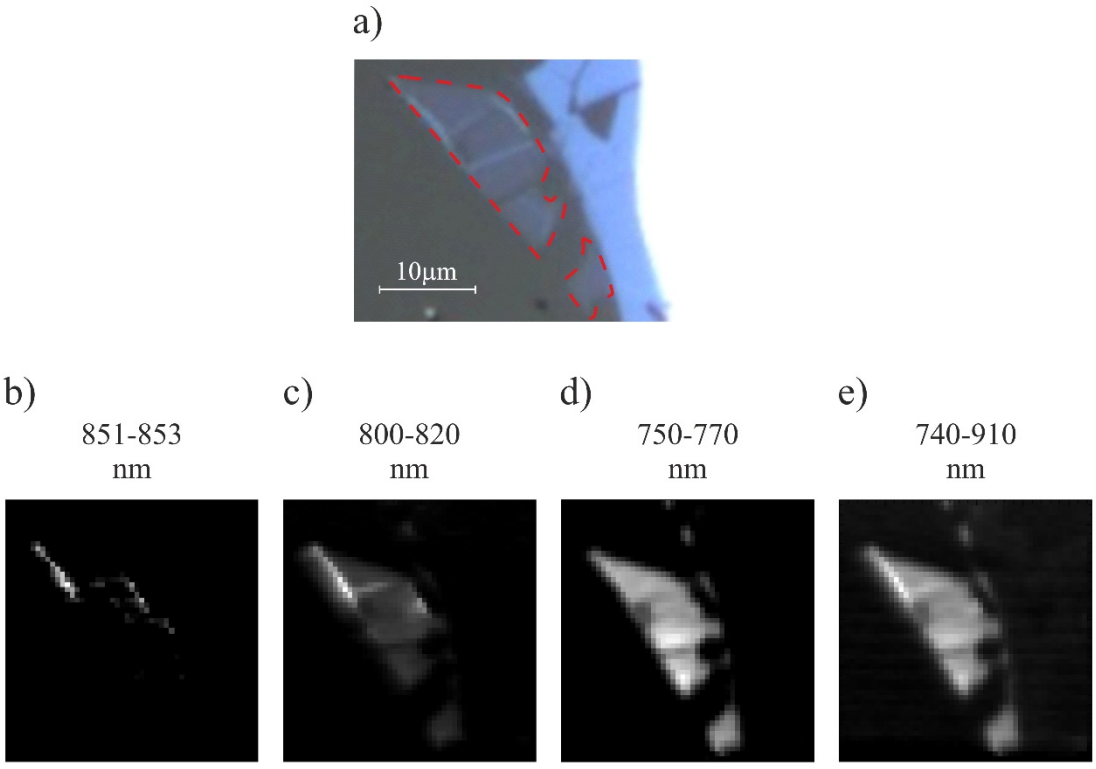

Figure 2.10 Photoluminescence emission map of the MoS_2 monolayer at 4 K. Brightness of the pixels correspond to the intensity of the collected signal in (b, c, d, e,). The dash line corresponds to area of the monolayer crystal (a). We observe a very intense and narrow peak centred at 852 nm from the edge area where the monolayer crystal during transferring procedure to the substrate is screwed and applies mechanical strain to the crystal in these regions (b). The integrated signal in diapason of the wavelength from 800-820 nm (c). The integrated signal in diapason of the wavelength from 750-770 nm (d). The integrated signal in diapason of the wavelength from 740-910 nm (e).

2.4.3 Nonlinear response of the MoS_2 monolayer

In the 2H stacking order (see Figure 2.3), MoS_2 displays a layered structure where a layer of molybdenum is surrounded by two layers of sulphide DD_{6h} crystal symmetry. This structure presents a centrosymmetric structure. As it was mentioned in the chapter one, the second order nonlinear susceptibility $(\chi^{(2)})$ vanishes in the centrosymmetric structure and the third order nonlinear susceptibility $(\chi^{(3)})$ becomes a lowest order nonlinear susceptibility for these materials with centrosymmetric structure. However, in the odd number of layers of MoS_2 the inversion symmetry is broken and one can expect a second

order nonlinear effect such as second harmonic generation (SHG) and spontaneous parametric down conversion (SPDC) [50]–[52].

The second order nonlinear susceptibility from a MoS_2 reported [from *7000 to 9000 pm/V*] is a few orders of magnitude higher than for typical bulk crystals such as Lithium Niobate ($LiNbO_3$) and beta Barium borate (β- BaB_2O_4) (BBO). However, different values for the $\chi^{(2)}$ are reported in publications, which vary within three orders of magnitude [50]–[53]. Also, as was mentioned in the section 3 of this chapter, the monolayer obtained from mechanically exfoliation method presents about 20 times higher $\chi^{(2)}$ than the monolayer made with CVD method [50], [54].

$\chi^{(2)}$ value (pm/V)	Wavelength range (nm)	Estimation method/ Crystal fabrication method	Ref.
100	750	Theoretical	[53]
10^5	810	Experimental/ mech. exf.	[50]
$5 \cdot 10^3$	810	Experimental/ CVD	[50]
$0.8 \cdot 10^4$	860	Experimental/ mech. exf.	[51]
400	1100	Experimental CVD	[55]

Table 2.2 Comparison of second order nonlinear susceptibility of MoS_2 monolayer in literature.

2.4.4 Second order nonlinear susceptibility ($\chi^{(2)}$) and photoluminescence measurement of the MoS_2 monolayer

As discussed in section 2.5.2, reported $\chi^{(2)}$ values are very different (see Table 2.2). It was described in chapter one that the $\chi^{(2)}$ value has a quadratic contribution in the intensity of SHG and SPDC. It is therefore necessary for us to measure the $\chi^{(2)}$ value experimentally by ourselves. Figure 2.11 presents the experimental setup for this measurement. In this case, we use a tunable Ti-Sapphire femtosecond laser source at *80 MHz*. In order to do this measurement, we found the position of half wave-plate and the polariser where we get the max value for the intensity of the SHG.

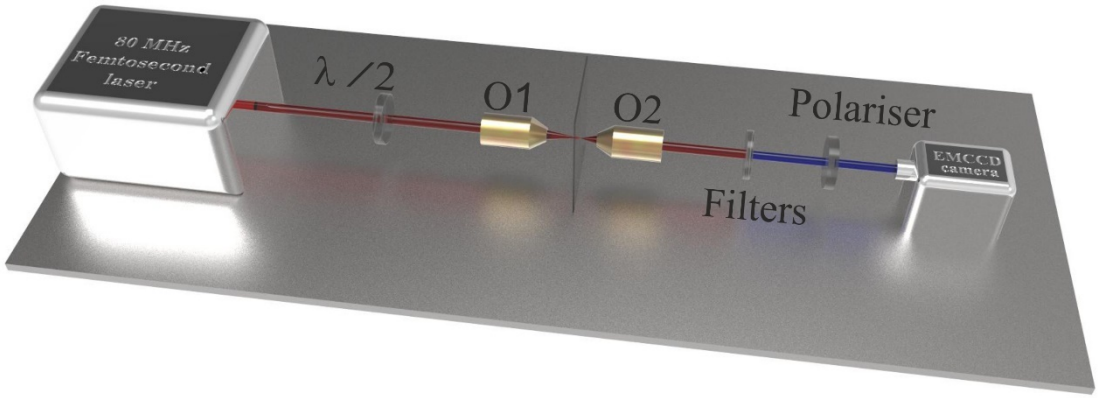

Figure 2.11 Experimental setup for pump wavelength dependence of the MoS_2second order nonlinear susceptibility.

We aim to characterise the SHG intensity as a function of pump wavelength, which leads us to the estimation of the $\chi^{(2)}$ value. The operational wavelength range for this experiment is from *710 nm (1.75 eV)* to *1000 nm (1.24 eV)*. In order to estimate the value of the $\chi^{(2)}$ we used the following formula [50]:

$$I_{2\omega} = \frac{1}{8}\left(\frac{\omega . d^2}{n_{2\omega} . n_{\omega}^3 . c^3 . \varepsilon_0}\right) . \left|\chi^{(2)}\right|^2 . I_{\omega}^2 . \tag{2.7}$$

where $n_{2\omega} \approx 4.5$, $n_{\omega} \approx 6$ [41], ω is the pump frequency and the thickness of the monolayer is $d=0.65\ nm$. Figure 2.12 demonstrates the experimental results for our measurement and the reported results in reference [56]. As one can see the measured spectral dependence of the $\chi^{(2)}$ looks very similar to the reported one. However the published data in [51] are roughly *20* times lower than our experimental results.

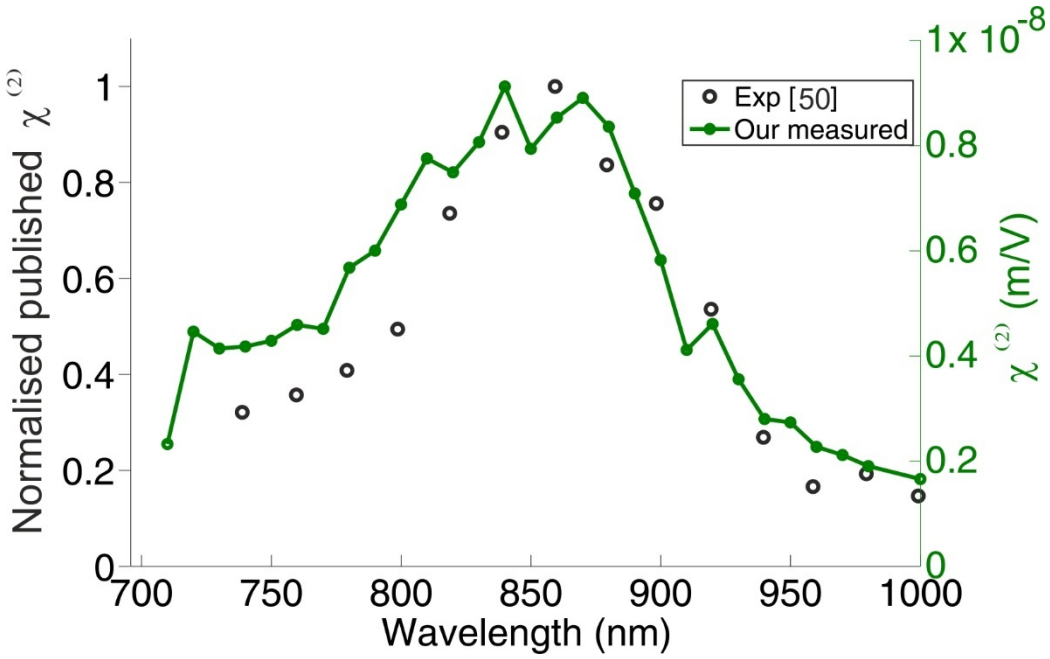

Figure 2.12 Black circles are normalised $\chi^{(2)}$ values measured in literature [51] (not in scale, magnified *20* times), Green line with dots are our experimental data for $\chi^{(2)}$ measurement, where the left hand side y-axis corresponds to the real calculated value of $\chi^{(2)}$ in our experiment.

2.4.5 Polarisation study of second harmonic generation (SHG) from MoS_2 monolayer

We also performed a polarisation-dependence analysis of SHG from the MoS_2 monolayer. In contrast to polarisation dependence of the spontaneous parametric down conversion signal which is not studied in literature, the features of the SHG polarisation dependence is measured and studied in literature. We use this measurement as an additional test to confirm that the target flake is a monolayer crystal. In order to do this measurement, we use the *100 Hz* femtosecond laser at *790 nm*. Figure 2.13 demonstrates the schematic view of the experimental setup of this experiment. Figure 2.14 (b) shows the MoS_2 flake which was used to study the SHG signal from MoS_2 monolayer. We pump the crystal with a 10x Nikon objective and a relatively large beam size $\sim 15\mu m$. Flake is transferred on the fused silica substrate and both of focusing and collimating objectives were placed on the 3D (x-y-z) stages. In order to study the polarisation dependence of the SHG from MoS_2 monolayer we place a half wave-plate before the focusing objective (*O1*) and a polariser before the Andor EMCCD camera. Two band-pass filters centred at *395 nm* with total

OD of *10* and *5 nm* bandwidth were placed after the collimating objective (*O2*) in order to block the pump efficiently.

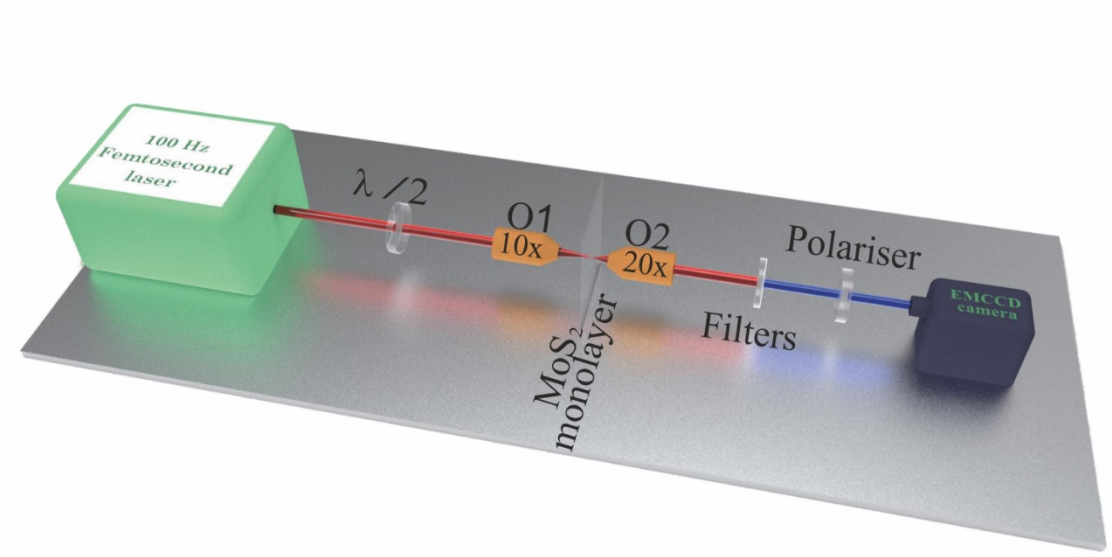

Figure 2.13 Schematic view of the experimental setup for the SHG polarisation dependence measurements. Excitation wave length is at *790 nm*. Two band-pass filters around *395 nm* are placed for the pump filtering. The laser is a tunable Ti-Sapphire laser.

In contrast to other experiments from literature, for the polarisation dependence study of the SHG emission from the flake, we keep the sample and polariser fixed and rotate the fundamental beam polarisation from 0° to 360° in intervals of 10°. Figure 2.14 (a) demonstrates the image of the flake for the input beam's polarisation at position at $45^{\circ}, 90^{\circ}$.

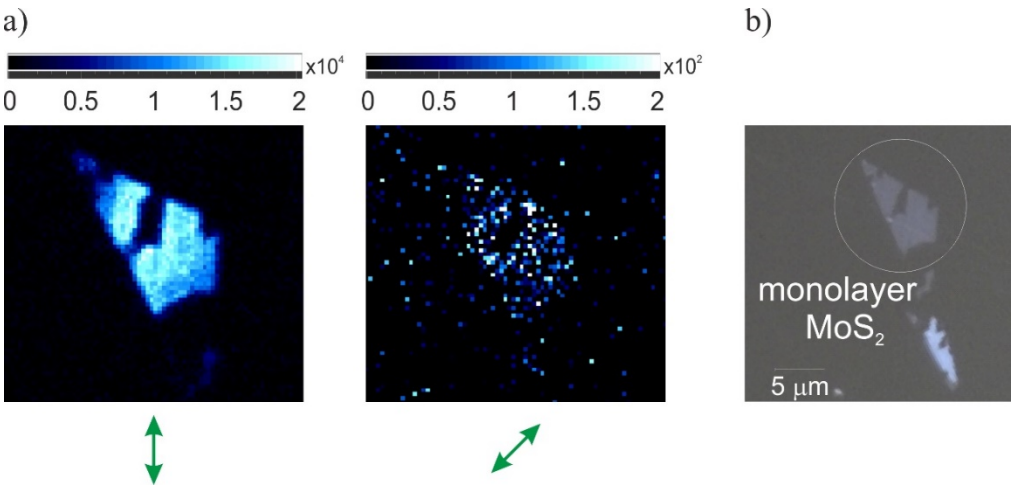

Figure 2.14 Image of the MoS_2 monolayer from EMCCD camera. The arrows correspond to the angle of the input beam's polarisation, while the crystal and the polariser before the EMCCD camera are fixed (a), MoS_2 monolayer crystal under microscope (b).

Figure 2.15 (a) presents a polar plot of the polarisation dependence of the emitted SHG signal. In comparison to the common six-fold patterns from literature, with this method we see four-folded pattern, which is indeed an equivalent to the same six-fold pattern. If we keep the sample axis fixed, choose a polarisation at the output by fixing the polariser's axis fixed at a random angle α_0° and rotate the pump polarisation by θ, the intensity of the measured SHG signal along α_0° is proportional to:

$$I_{\alpha_0}(2\omega) \propto (\cos(2\theta)\cos(\alpha_0) - \sin(2\theta)\sin(\alpha_0))^2 \tag{2.8}$$

However, if we keep the sample fixed and rotate both pump polarisation and the polariser before the EMCCD camera by θ° in the same direction, we measure the six-folded pattern shown in Figure 2.15 (b), which indeed is a popular measured pattern in literature, for instance in [57]. In this case the intensity of the measured SHG along parallel and perpendicular ($\alpha = \theta$, $\alpha = \theta + \pi/2$) polarisation are proportional to:

$$\begin{cases} I_{\parallel}(2\omega) \propto \cos^2(3\theta) \\ I_{\perp}(2\omega) \propto \sin^2(3\theta) \end{cases} \tag{2.9}$$

In Figure 2.15 (c), we present another method of polarisation dependence measurement of the same SHG signal. In this method, we keep the crystal fixed and rotate the

polarisation of the fundamental beam θ° clockwise, while rotating the polariser by θ° anticlockwise. As one can see in this case we get a two-fold pattern.

In Appendix II, we present a detailed calculation to demonstrate how the different methods of measurement are equivalent and all three methods give us the expected results from calculation. Our different methods of measurement can be a reference for further studies and one can use the preferred method of measurement and confrim that the measured signal is the SHG signal.

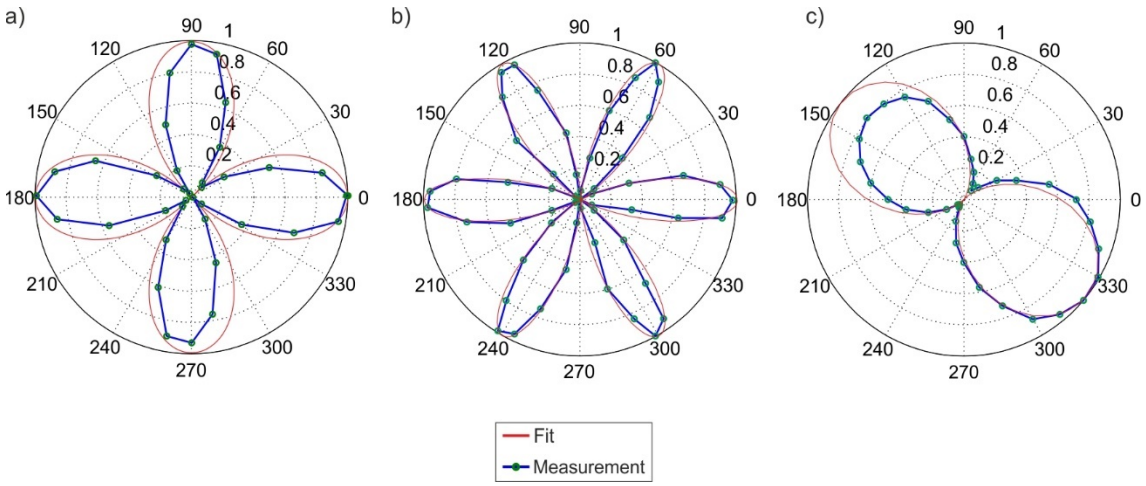

Figure 2.15 Polarisation dependence of the SHG signal. SHG polarisation dependence measurement with a pump wavelength at 790 nm. We keep the crystal and polariser before the EMCCD camera fixed, then rotate the pump polarisation (a) We keep the crystal fixed and rotate the pump polarisation by θ clockwise and the polariser by θ also clockwise (b) We keep the crystal fixed and then rotate the fundamental beam polarisation by θ clockwise and the polariser by θ anticlockwise (c).

2.5 Spontaneous parametric down conversion (SPDC) measurement

In this section we present the experimental study of the SPDC from MoS_2 monolayer in both visible and IR regime.

2.5.1 SPDC measurement in NIR regime

As mentioned in Chapter 1 section 1.3.3.1, the proposal of using the optical parametric oscillator (OPO) as an optical analogue of DCE with a subwavelength thickness of non-centrosymmetric crystal as a nonlinear medium was published in 2009 [35]. The main idea here for studying the TMDC monolayer, was based on the application as a

subwavelength $\chi^{(2)}$ crystal for the DCE analogue. In this section, we show different approaches and attempts for SPDC photon pair measurement from a MoS_2 monolayer.

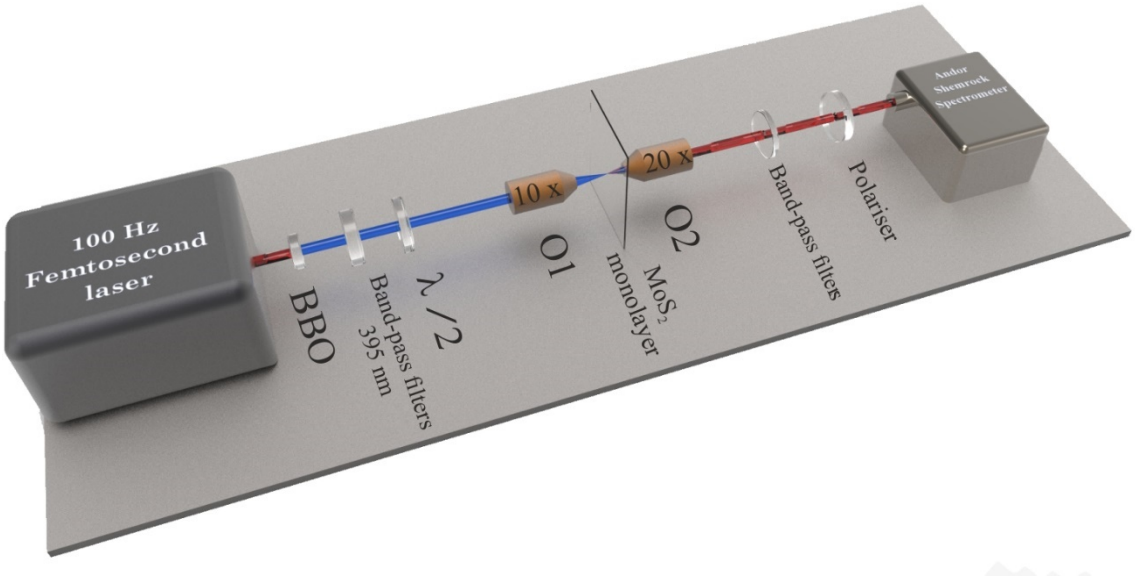

Figure 2.16 Experimental setup for the SPDC signal measurement with spectrometer. The supersensitive EMCCD camera integrated into the spectrometer is used in this setup to detect the expected SDPC signal from the MoS_2 monolayer.

As a first step, we use the Andor Shamrock spectrometer with an EMCCD camera to measure the SPDC signal at *790 nm* under *395 nm* excitation. For this experiment, we used a *100 Hz*, *110 femtosecond* laser. Figure 2.16 presents the experimental setup for this experiment. We used the BBO crystal to generate SHG from *790 nm* pump and use two band-pass filters centred at *395 nm* with OD of *10* for the pump for the efficient filtering of the *790 nm*. The filtering of the pump signal is critically important as our aim is to measure the SPDC signal exactly at this wavelength. The experiment on MoS_2 monolayer confirmed that the absorption of the MoS_2 crystal for this wavelength is about one order of magnitude higher than for the *790 nm*. This potentially means that we cannot use the same level of energy (*100 μJ at 790 nm*), which can be used for the SHG. Such a high pump energy leads to the immediate damage of the flake. Figure 2.17 presents the damage threshold measurement for the MoS_2 monolayer under *395 nm* excitation for the *100 Hz* femtosecond laser. It is important to note that the damage threshold for irreversible change of the properties of the MoS_2 monolayer is less than the physical (i.e. complete ablation) damage threshold. After a certain intensity, which is about the *60%* to *80%* (it is different from one crystal to another one) of physical damage threshold, the life-time

and number of counts in detector is not stable anymore and changes in time. In order to be sure about the stability of the detected signal, it is recommended to keep the intensity below *50%* of the physical damage threshold. As the SPDC process depends on the average power instead of the peak power, we decide to use the CW source instead of the pulsed laser source with high peak intensity.

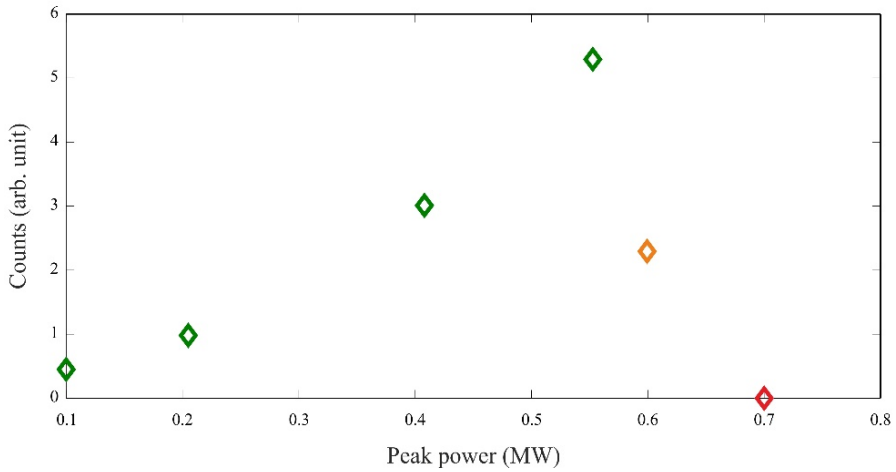

Figure 2.17 Damage threshold measurement of the MoS_2 monolayer. This measurement is taken under *790 nm*, in the setup of Figure 2.13. Green lozenge corresponds to the peak power, where the SHG signal is stable. Yellow colour corresponds to the peak power where we observe decay in the signal. Red colour corresponds to the peak power where we observe an immediate physical damage and monolayer crystal immediately disappears.

Figure 2.9 (a) shows a photoluminescence signal from the MoS_2 monolayer and as it clear that around *810 nm* we have just the tail of the photoluminescence signal. However, the expected SPDC and photoluminescence signals both increase linearly with the pump power, the increasing of the pump power or the exposure time cannot extract the SPDC signal from the typical photoluminescence. Notwithstanding the mentioned argument, potentially the SPDC signal can be considered in two different regimes: low gain and high gain regime. Here one of the possible and simple approaches for this experimental issue, is to use the photoluminescence emission with 405 nm pumping for a very low power and use its normalised spectrum to subtract from the normalised signal measure under a higher power. This method can work if one assumes that SPDC process has a threshold value for the pump power below which the probability of the photon pair generation is very low and one does not expect to detect photons around double wavelength of the pump. Figure 2.18 demonstrates the normalised emitted signal under

50 μW excitation subtracted from the normalised photoluminescence signal under *20 mW* for the same spot size. As it is clear, there is no peak around the *810 nm* by using this method.

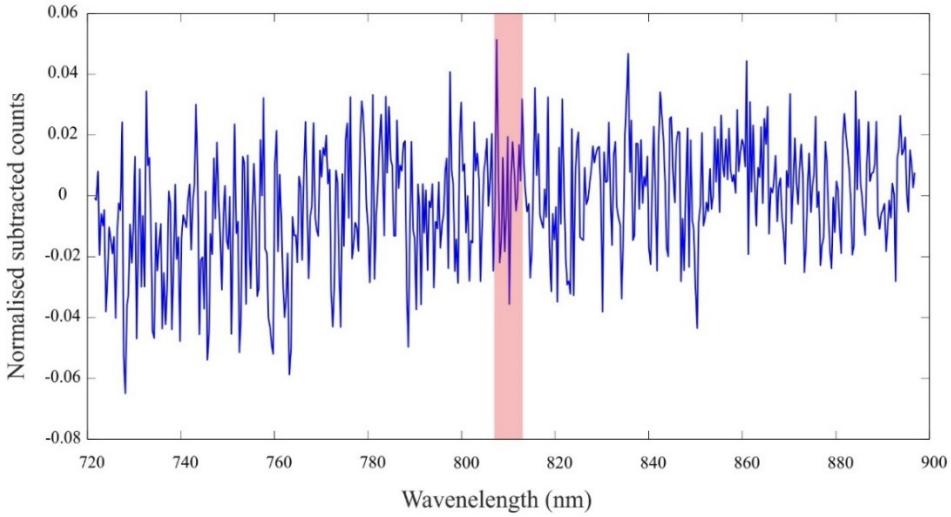

Figure 2.18 Subtracted of normalised signal from the MoS_2 under 405 nm with 50μW from the same pump wavelength with 20 mW. The red line corresponds to the region of expected SPDC peak.

The other idea is to use normalised photoluminescence emission from the MoS_2 monolayer under *532 nm* pump and to subtract this from the normalised collected signal from the MoS_2 monolayer under the *405 nm* excitation. The reasoning behind this idea is that we do not expect to have a SPDC signal centred around *810 nm* under the excitation at *532 nm*, while the expected SPDC from the MoS_2 monolayer under the *405 nm* excitation is expected to be centred around *810 nm*. However, by looking at the Figure 2.9 (a), it is obvious that we cannot use this method, as the photoluminescence signal for *405 nm* and *532 nm* excitations are not identical.

As we did not see any indication for a peak centred around *810 nm*, we assume that the SPDC is dominated by the photoluminescence emission from the monolayer crystal while we aim to measure the quantum cross-correlation of the expected SPDC signal as a reliable approach for the SPDC measurement. Figure 2.19 presents the experimental setup for the cross-correlation measurement of the expected SDPC signal. We use Excelitas NIR SPAD [58] for this measurement. As seen in the green region in the Figure 2.20 (a) the maximum of the $\chi^{(2)}$ is between *840 nm* and *880 nm*, and two maxima indicated by red vertical transparent lines are at *840 nm* and *870 nm*.

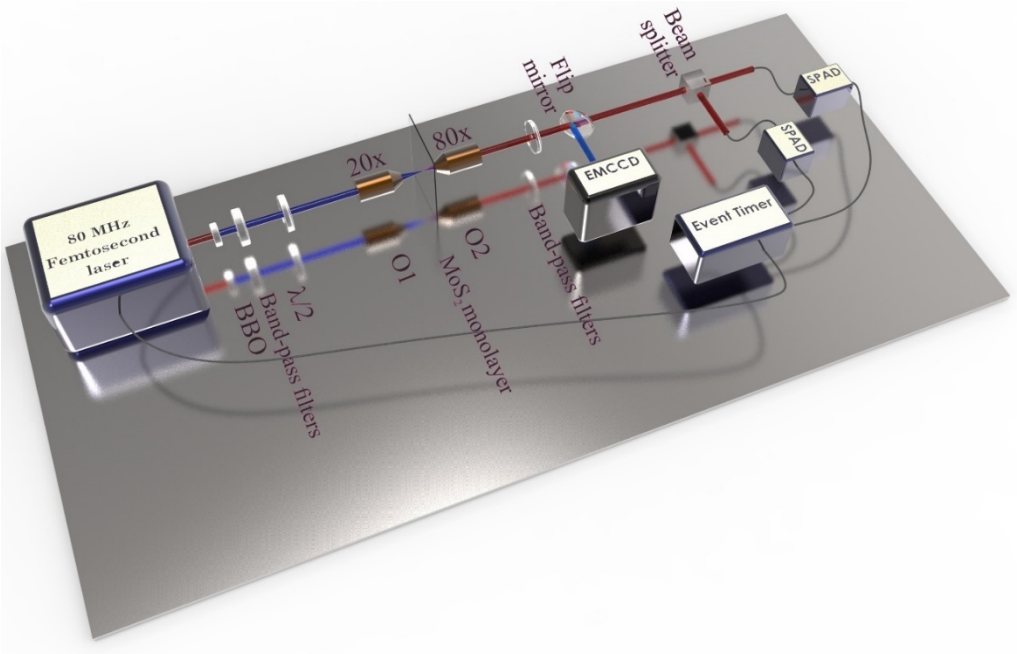

Figure 2.19 Experimental setup for the cross-correlation measurement of the signal centred around 875 nm.

Based on this information and considering the quantum efficiency of the detectors (see Figure 2.20 (b)), band-pass filters in the market and the stability of the tunable *80 MHz* Ti-Sapphire femtosecond laser, it was decided to investigate SPDC signal generation around *875 nm* using BBO crystal to generate the pump at $\sim 437\,nm$.

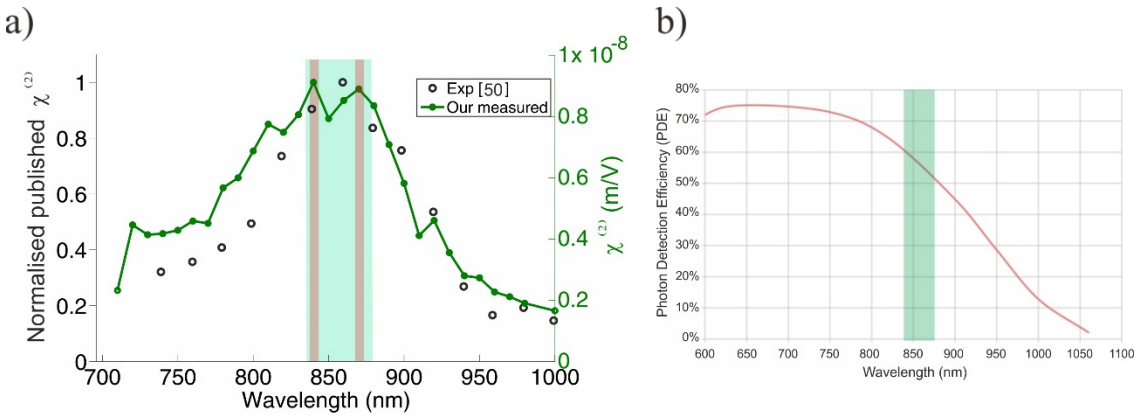

Figure 2.20 Comparison of the $\chi^{(2)}$ versus wavelength with the quantum efficiency of the detector. Green area presents the most efficient part of the $\chi^{(2)}$ and red lines indicate the two maximums for the $\chi^{(2)}$ (a), Quantum efficiency curve of the Excelitas NIR single photon detectors. The green area corresponds to the same wavelengths, where we have maximum of the $\chi^{(2)}$ [58] .

We use the signal from BBO crystal and efficiently filter it with a combination of two band-pass filters centred around *440 nm* and a short-pass filter (*<550 nm*) to block the fundamental beam at *875 nm* with OD *18*. We also use the combination of a long-pass (*>850nm*) and a short-pass (*<900 nm*) filter to make a band pass-filter centred at *875 nm* with 50 nm bandwidth. As one can see in this setup we collect the emitted signal in the transmission direction and use the *50-50* beam splitter to split the signal between two single photon counting module. Figure 2.21 (a) presents the results from cross-correlation measurement of generated photons over two hours. With the EMCCD camera and flip mirror in the setup we can easily control the region of excitation. For this experiment, we excited the region of the MoS_2 monolayer from where we get the max SHG signal with the *5 μm* focused spot size, power at *18 μW* and measure *37 kHz* counts in each detector. Figure 2.22 demonstrates the time-resolved signal in this experiment. As one can see this time-resolved signal from the crystal is longer than the response function of the detector, which is presented by the green dash line. This confirms the hypothesis that the signal is mainly due to the photoluminescence (SPDC is expected to be instantaneous) and it is why the ratio of the zero-delay peak (correlated peak) in respect to accidental peaks is around one. In order to estimate the number of expected detectable correlated photon pairs ($N_{expected}$), we use the Equation 1.32 and compare it with the standard deviation of the measurement in Figure 2.21 (b) to check the compatibility of the results with theory. Detailed calculations for the expected detectable correlated photon pairs can be found in Appendix I. Due to the additional source of noise from electronics, which binds the minimum error to a fixed percentage of the total counts, we get a higher experimental standard deviation in comparison to the theoretical standard deviation. This means that we cannot improve the Coincident to Accidental Ratio (CAR) simply by increasing the integration time. The expected number of detectable correlated photon pairs, which is about 1930 during two hours integration, still about *14* times less than the experimental standard deviation, which is about *27kHz* counts as illustrated in Figure 2.21 (b). We should mention that this calculation is an estimation and the main assumption is the isotropic emission from the crystal, i.e. because of the lack of phase-matching inside the crystal, the photon pairs will be emitted in all directions. Measuring the long life-time of the emitted signal and the lack of a CAR larger than one from the MoS_2 monolayer in the visible range, leads us to make a conclusion that this signal is mainly due to the strong photoluminescence signal in the visible range. In order to work around this issue, it is proposed to look for the SPDC signal from the MoS_2 monolayer in the IR region.

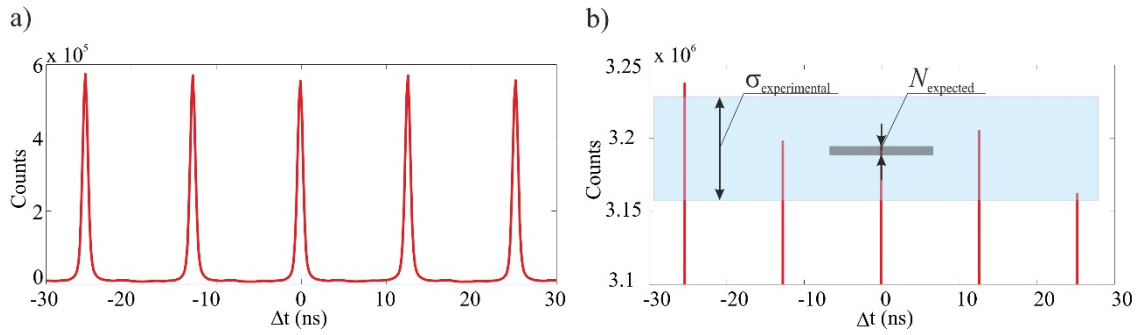

Figure 2.21 Cross-correlation measurement of the emitted signal from MoS_2 monolayer, centred around 875 nm with 50 nm of bandwidth (a). We investigate the contribution of the expected number of detectable photon pairs from the SPDC process in the cross-correlation measurement and compare it with the experimental standard deviation of the measurement (b).

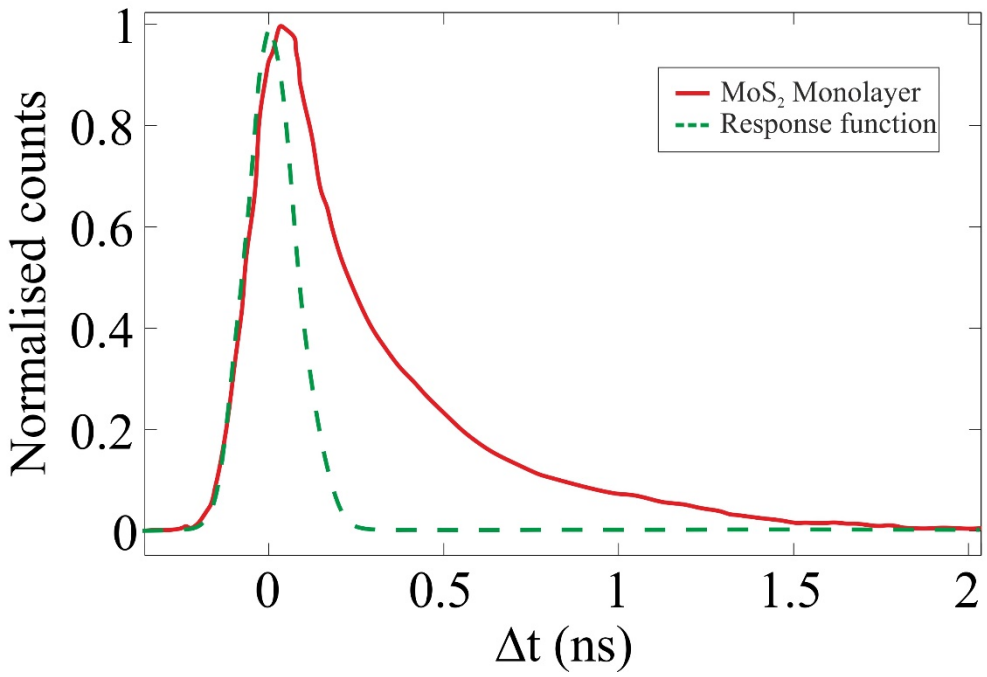

Figure 2.22 Time-resolved visible signal from MoS_2 monolayer centred around 875 nm with 50 nm bandwidth.

2.5.2 SPDC measurement in IR regime

Although we assume that the second order nonlinear susceptibility of the MoS_2 monolayer in IR regime should be less than that in the visible regime, we do not expect a significant photoluminescence signal. Pumping the crystal at around 800 nm and measuring the signal the IR region should eliminate the residual photoluminescence.

Considering the quantum efficiency of our ultra-low noise single photon detectors (ID 230) and available efficient band-pass filters, we decided to pump the crystal at *770 nm* and measure the quantum cross-correlation of the signal in both transmission and transmission-reflection configuration within *80 nm* of bandwidth centred around *1540 nm*. Figure 2.23 shows the two configurations of the setup for the cross-correlation measurement.

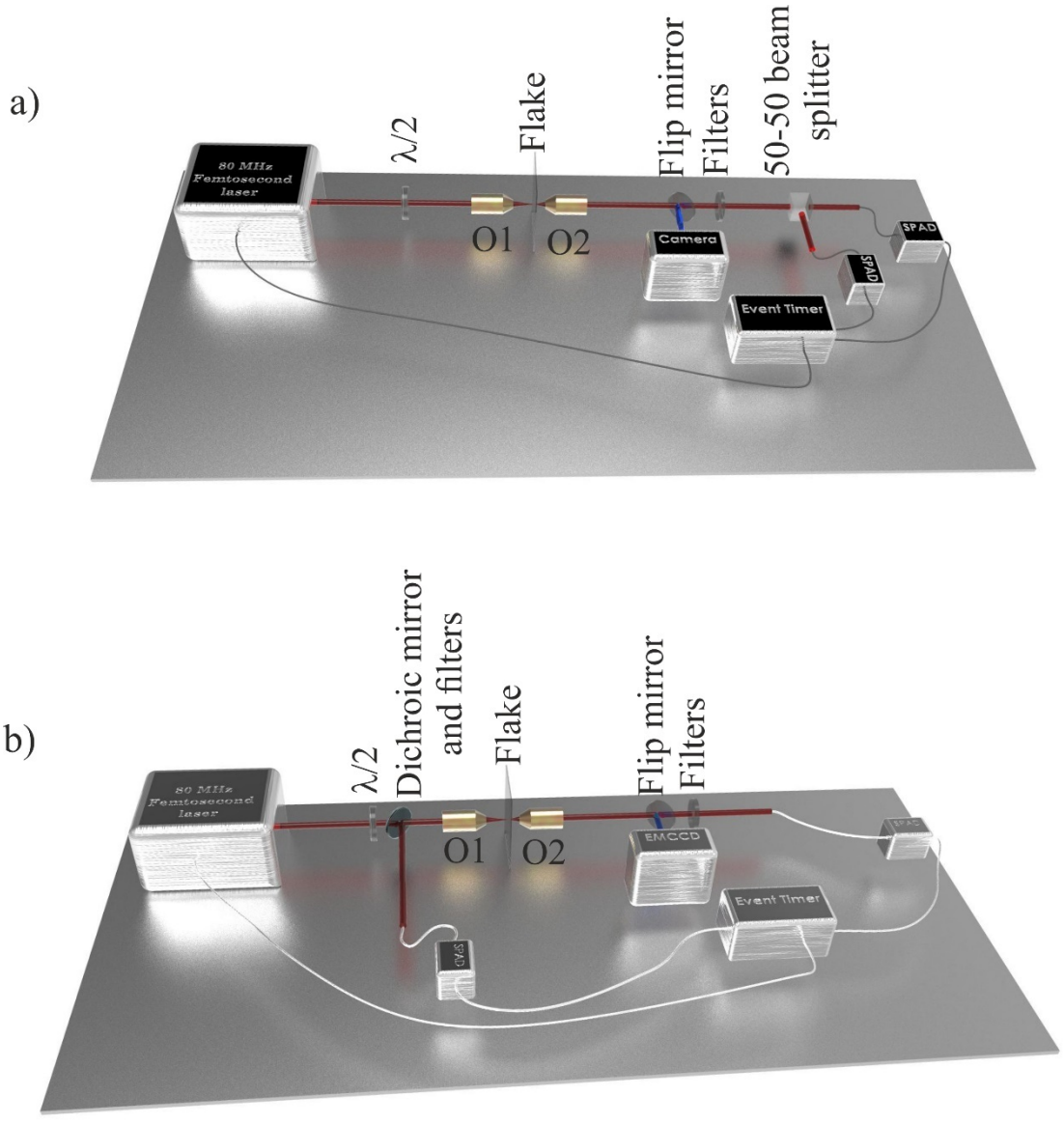

Figure 2.23 Two configurations of setup for cross-correlation measurement. Transmission configuration with beam splitter. In this configuration, we collect signal from the second objective and split it by a 50-50 beam splitter between two detectors (a), We use the collected signal from the first and second objective. In this configuration we use dichroic mirror between HWP and first objective to direct the selected wavelength in the reflection to the SPAD.

As a first step, we investigate the IR signal emission from the MoS_2 monolayer attached to the bulk crystal (few layers) with a spatial resolution of *2 μm* Figure 2.24 (b). In order to perform this measurement, we keep the position of the focusing and collimating objectives fixed and scan the position of the crystal with respect to the focusing beam. As one can see the intensity of the IR signal from the bulk crystal is about two orders of magnitude higher than the IR signal from the monolayer or a few layer crystal. In particular points, the intensity of the IR signal from the bulk crystal's edge is even more intense than the bulk mid area. In order to compare the IR signal and the SHG signal from the monolayer and several layers of the MoS_2 we make a spatial map of the SHG signal from the same area of the crystal with the same spatial resolution. Figure 2.24 (c) shows the intensity of the SHG signal collected with a 770 nm pump. We see that a very intense signal comes from the monolayer area and some bright spots from the right edge of the bulk crystal. We study the power dependence of the SHG and IR signal, which are demonstrated in Figure 2.24 (e & d). Power dependence of the SHG signal perfectly fits a typical quadratic function while the IR dependence has a linear fit, which completely matches the SDPC model and it also can be associated to the photoluminescence signal as well.

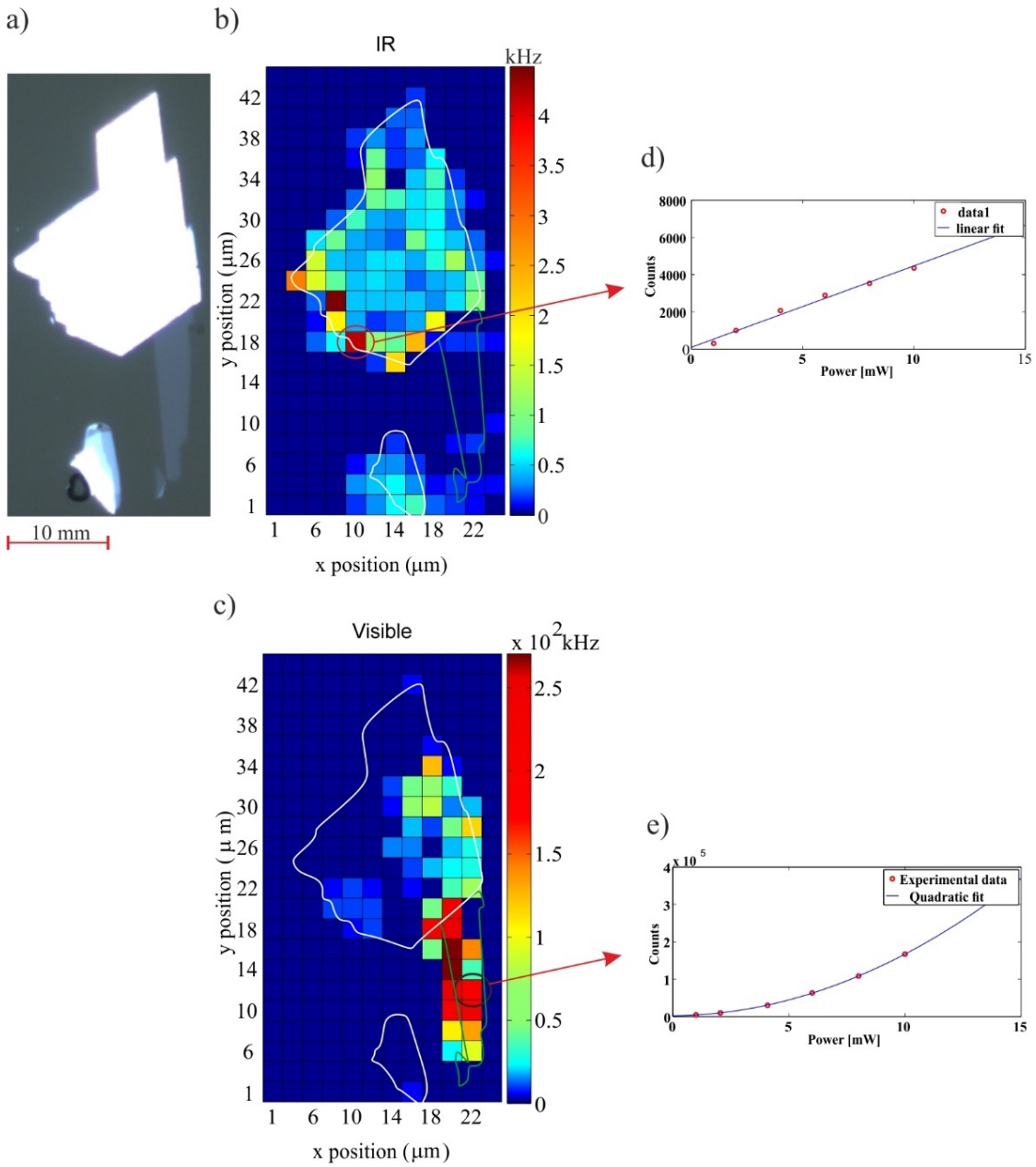

Figure 2.24 Microscope image of the crystal (a). IR signal intensity from the monolayer and bulk crystal (b). SHG signal intensity from monolayer and bulk crystal of MoS2 with 2 µm resolution. The pump wavelength for this measurement and measurement of IR signal is 780 nm (c). Pump-power dependence of the IR signal (d). Pump-power dependence of the SHG signal (e). The white borders in b&c correspond to the bulk and multilayer parts, while the green border correspond to the monolayer parts.

In Figure 2.25 we measure the lifetime properties of the IR signal by time-correlated single photon counting, using a trigger pulse from the femtosecond laser. Surprisingly we measure different lifetimes from different points on the bulk edges, as can be seen by comparing the black, blue and green curves. When fitted the curves always reveal two

exponential contributions, with roughly the same decay times of *0.15 ns* and *4.7 ns* but with different weights from point to point. We verify that the fast component corresponds to the response function of the detectors and the electronics, thus indicating a lifetime shorter than *0.15 ns* for this process. Strikingly the signal from the monolayer only presents the fast component. Figure 2.26 presents the fit for the black and red curves, which correspond to the signal from the bulk edge and monolayer crystals, respectively.

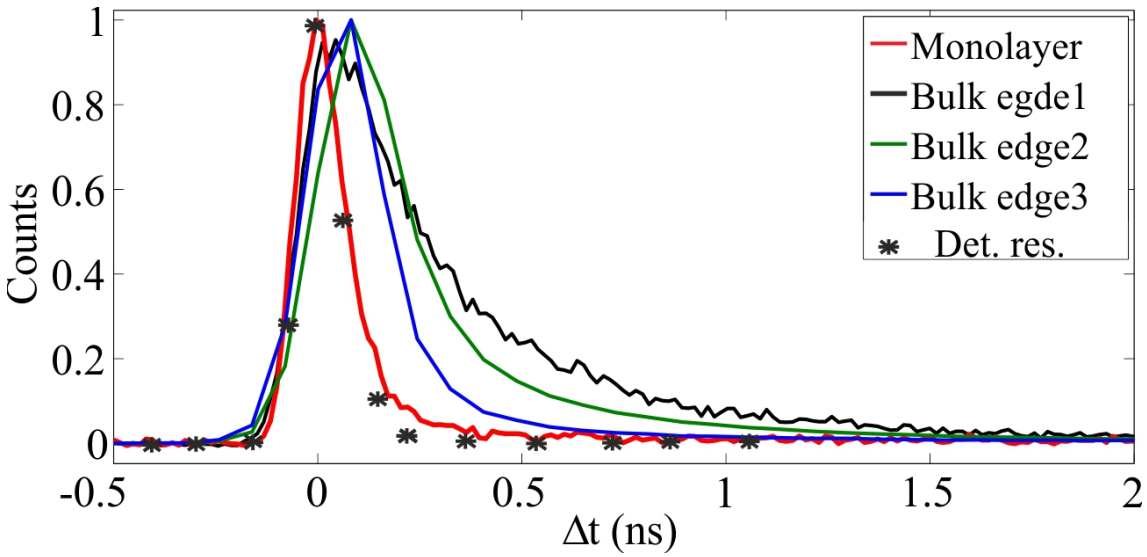

Figure 2.25 Time-resolved IR signal from the monolayer (red curve) and three different point from the bulk edge (blue, black and green curves). Black stars correspond to the detectors response function.

We proceeded to measure the cross-correlation between the two detectors for the signal emitted from the monolayer (see Figure 2.27). We pump the monolayer with a *2 μm* beam at *770 nm* and power of *100 mW*, just below the damage threshold, obtaining a typical count rate of *1.44 kHz* against a background of *850 Hz* (PL from the fused silica substrate and detector dark counts). We also use band-pass filters with 80 nm bandwidth and centred around *1540 nm*. Here by damage threshold, instead of the physical damage of the crystal we mean the power above which the signal from the crystal is not stable and experiences decay in time. We need to integrate for about 90 hours in order to obtain the results illustrated in Figure 2.27. As in the measurement for the visible range, a CAR (coincidence to accidental ratio) of 1 is reported.

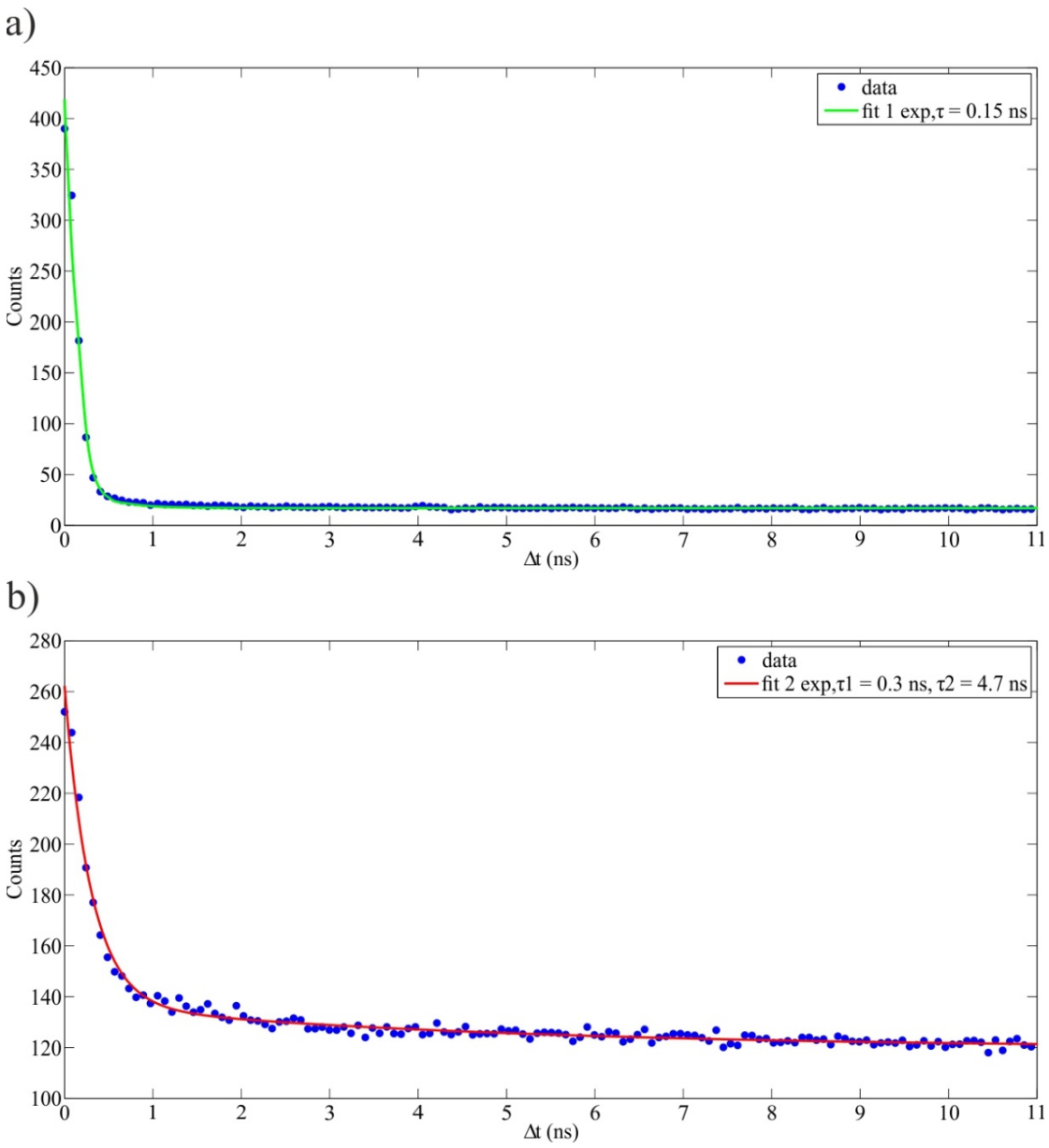

Figure 2.26 Fit of the IR emitted signal. Fit for the time-resolved IR signal from MoS_2 monolayer (a) Fit for the time-resolved emitted IR signal from the bulk edge (b).

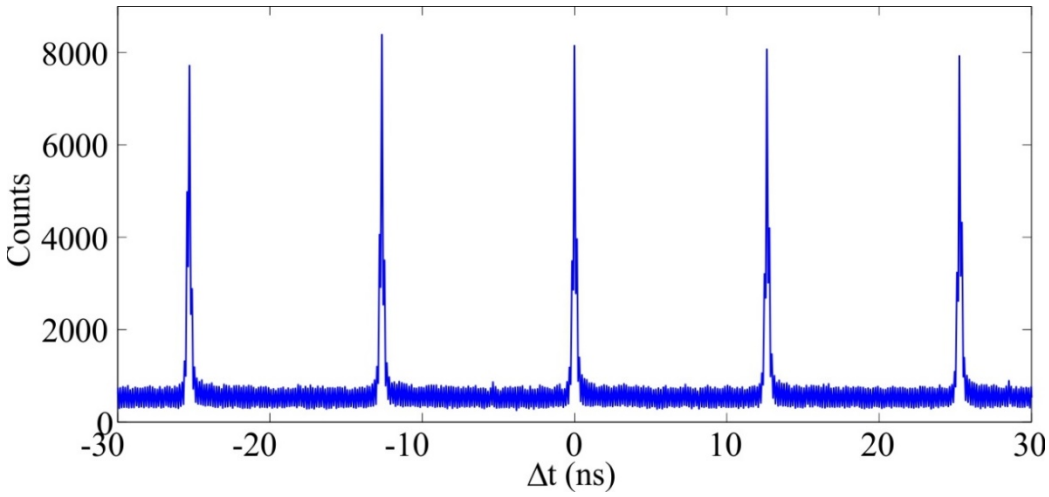

Figure 2.27 Cross-correlation measurement of the emitted IR signal from MoS_2 monolayer. This results are achieved by the signal from the collected signal on the objective 2 in Figure 2.23 (a).

In Figure 2.28 we perform the same measurement for the emitted signal from an area on the bulk crystal and integrate for about 2 hours. In this case, we pump the crystal again with a *2 μm* beam at *770 nm* and power of *20 mW*. We use the same band-pass filters with *80 nm* width and centred around *1540 nm*. This is the safe power for the bulk edge. We will see a clear decay in number of counts if we pump the edge area with higher intensity. We measure about *55 kHz* counts in each detector.

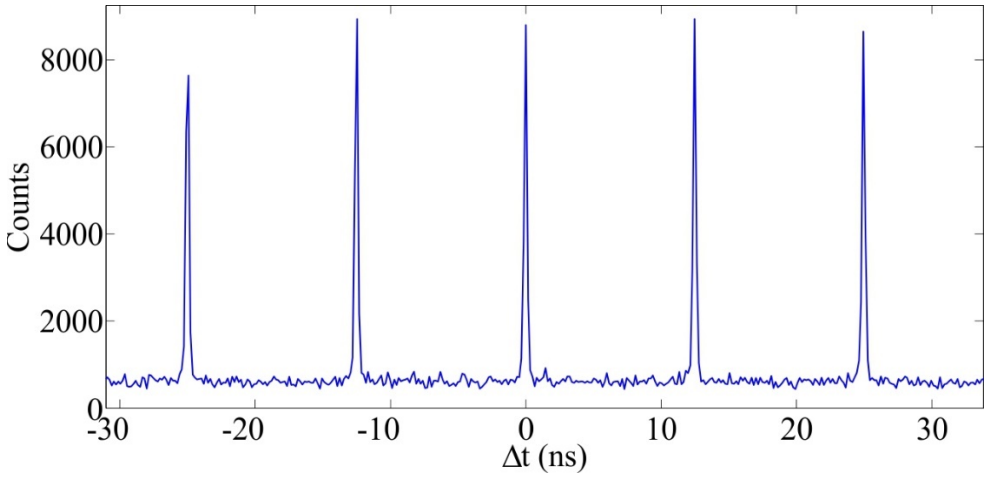

Figure 2.28 Cross-correlation measurement of the emitted IR signal from MoS_2 bulk edge.

We also measure the cross-correlation of the IR signal from monolayer crystal between a detector collecting the signal from objective *O1* and second detector collecting the signal from *O2* (transmission-reflection configuration) and obtaine similar results for CAR.

This measurement is taken over 52 hours of integration. Figure 2.29 presents the results of the cross-correlation for the transmission-reflection configuration. We still use the same pump intensity, wavelength and band-pass filters as in transmission configuration.

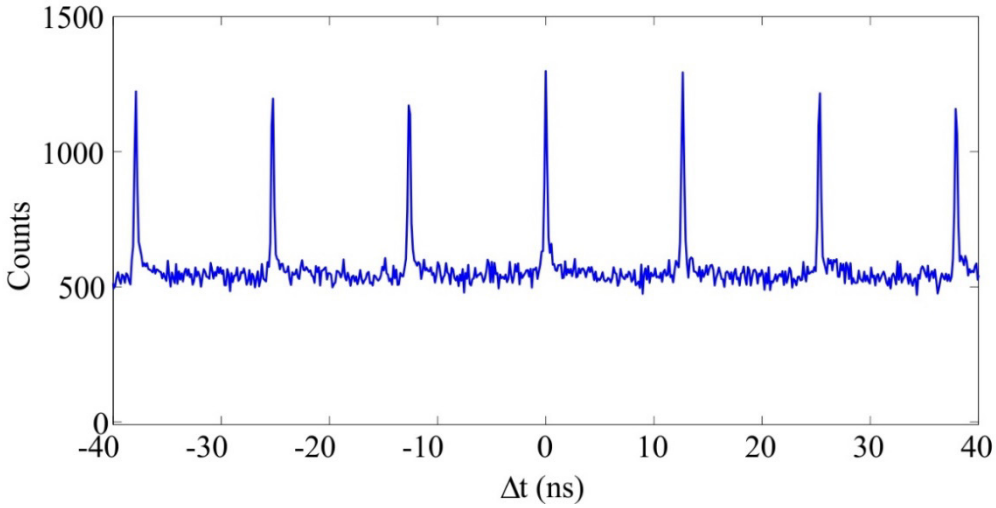

Figure 2.29 Cross-correlation of the IR signal from the MoS_2 monolayer for the transmission-reflection configuration of the detectors.

We also study the polarisation dependence and polarisation properties of the emitted signal from monolayer and bulk edges. The collected signal from the monolayer crystal does not depend on the pump polarisation and the signal by itself is not polarised. Figure 2.30 presents the polar plot of the polarisation dependence. This behaviour of the monolayer crystal completely accounted for by the theoretical prediction of the polarisation dependence and polarisation of the generated signal for SPDC, which is presented in Appendix II.

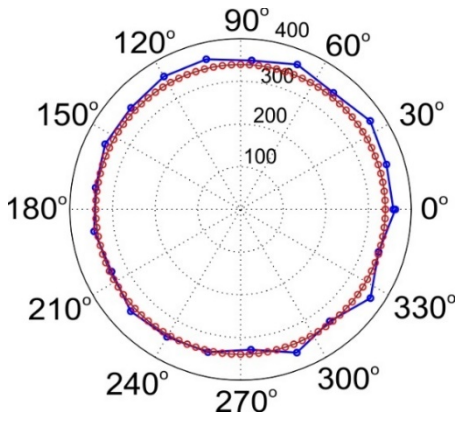

Figure 2.30 Polarisation dependence of the emitted IR signal from the MoS_2 monolayer. Blue circles correspond to our measured data and red circles correspond to the theoretical calculation of polarisation dependence of the SPDC signal.

We also investigated the polarisation dependence and the polarisation properties of the emitted signal in the IR regime from the bulk and bulk edge. In contrast to the signal from monolayer, we observe an unexpected behaviour from bulk and bulk edge. Figure 2.31 shows different dependence of emitted photons polarisation and how it depends on pump polarisation. In order to perform this measurement, we measured the dependence for different spatial points of the same bulk crystal. We found 5 different kind of dependence. There are points where the emitted signal is well polarised (about *50%*) and at the same ratio emitted signal depends on pump polarisation (see Figure 2.31 (a)), while in other points, the brightness of the signal is higher but the visibility is less and the signal mostly depends on pump polarisation or polariser angle (see Figure 2.31 (b)). Figure 2.31 (c) shows a point where for the same brightness of the signal we have less dependence of pump polarisation, while the signal is mostly polarised (about 80%). We also found points where the emitted signal just depends on pump polarisation or polariser's angle Figure 2.31 (d&e). In general, the signal depends on both the pump polarisation and polariser angle but with different brightness's for different points. This behaviour from bulk and edge state is not fully understood yet.

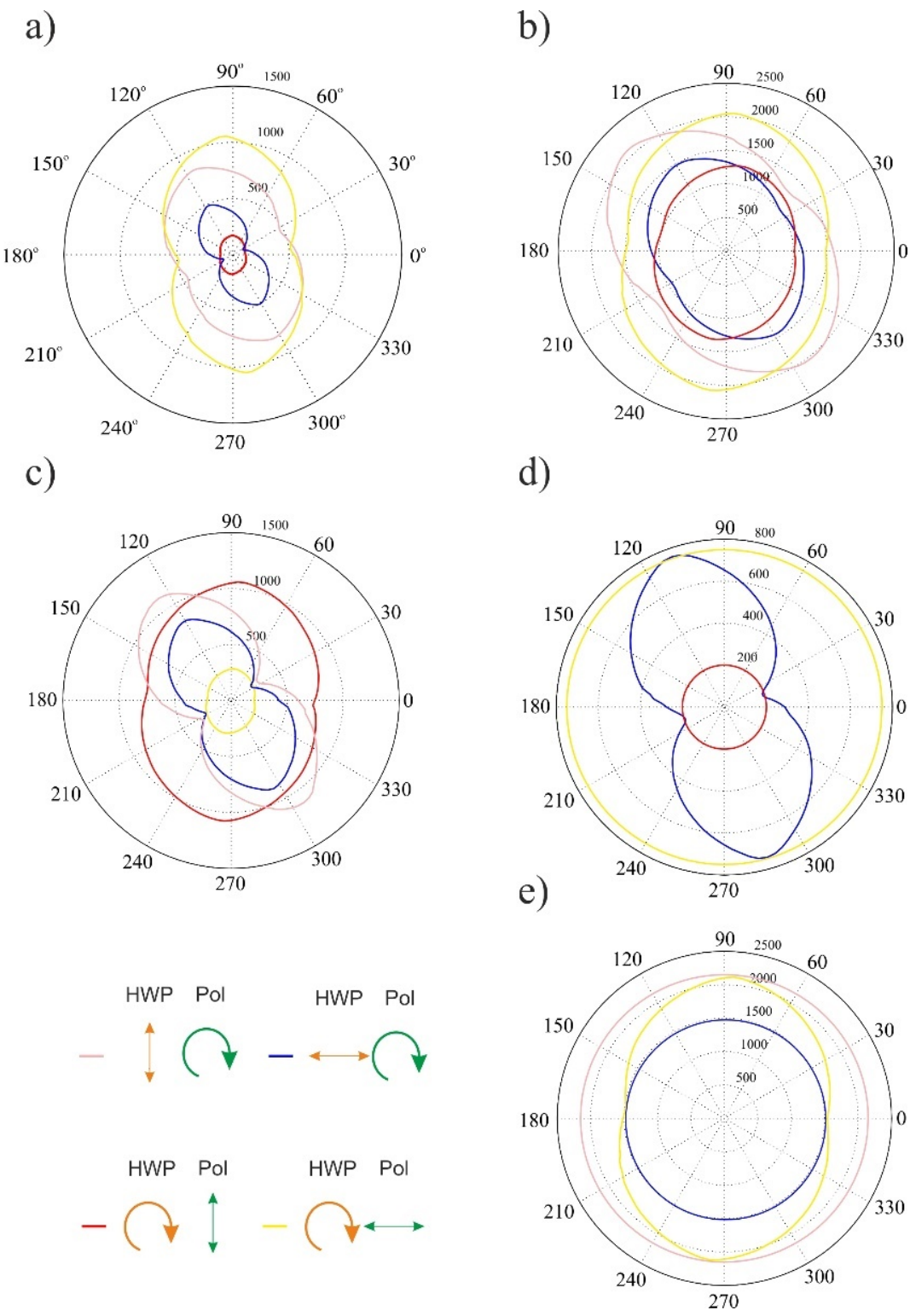

Figure 2.31 Polarisation characteristics of different points of the bulk MoS_2. The pink and blue curves correspond to the measurements, where the pump has a fixed polarisation along vertical and horizontal axis and we rotate the analyser before the detector. The red and yellow curves present the measurement, where the analyser's axis is fixed horizontally and vertically while we rotate the polarisation of the pump. The crystal axis for all these measurements is fixed.

2.6 Conclusion

As we mentioned in 2.6.2 we get different life-time and polarisation dependence and polarisation properties of the emitted signals from monolayer and bulk crystal. In the case of the investigated signal from monolayer, this signal completely fits the theoretical prediction for the polarisation characteristics and the dependence on the pump polarisation for the SPDC signal, whilst we keep the question open to understand the nature of the signal from bulk and bulk edge. The main point here is that based on these obvious differences we believe that these two signals from monolayer and bulk belong to different physical processes. Notwithstanding that the measured polarisation dependence and the life-time of the signal in IR regime completely follows the expectation for the SPDC signal, the cross-correlation measurement with CAR higher than 1 is the undeniable and the final proof of the quantum correlation of SPDC emission.

Based on the calculation, presented in the Appendix I, the use of a cavity for the detection of SPDC signal can be a solution to increase the CAR. We also recommend the fabrication of the sandwiched multilayers of MoS_2, still in the subwavelength order. This can be another solution to increase the number of photon from SPDC processes to make it measurable with current electronics.

3 Dynamical Casimir effect in modulated waveguide and modulated photonic crystal fiber

As described in the introduction chapter, the dynamical Casimir effect (DCE) in its original form, i.e. the generation of the entangled photon pairs form the vacuum state as the result of the oscillation of the two parallel mirrors at optical frequency, is very difficult to realise.

However, we can replace this pure modulation of the real length of a cavity between two mirrors by temporal modulation of any parameter, which leads to the temporally varying of the boundary condition. Optical analogues of this temporal modulation can be induced by a change of the refractive index in time. A refractive index modulation can be done in different ways and can lead to the temporal modulation of boundary conditions.

In this chapter, we present different experimental approaches to the optical analogy of the dynamical Casimir effect. The first method considers the experimental approach, where we use the spatial modulation of the refractive index along a waveguide. In this method, we modulate the intensity of the pulsed laser beam along the propagating axis in the waveguide. In order to achieve this intensity modulation, we periodically modulate the waveguide diameter. For a fixed pulse energy, this modulation of the diameter leads to a periodic modulation of the intensity. This modulation of the intensity occurs along the propagation distance z, where the lab frame is our reference. However, one can consider this modulation as the modulation of boundaries in time, which is the concept of the dynamical Casimir effect, when one considers the travelling pulse as the new reference frame. In other words, for the traveling pulse the changing of the refractive index of the waveguide, which leads to the intensity modulation of the pulse occurs in time instead of space. Figure 3.1 presents the schematic view of the concept of the intensity modulation in the waveguide. Conceptually, the modulation in space (and not time) in the lab frame, can be considered as the modulation in time if we are to transform into the comoving frame of the pulse where the modulation happens in time and time only. For this transform

to be valid, we need the pulse duration to be less than the modulation frequency, as otherwise we see both time and space modulation in the comoving frame.

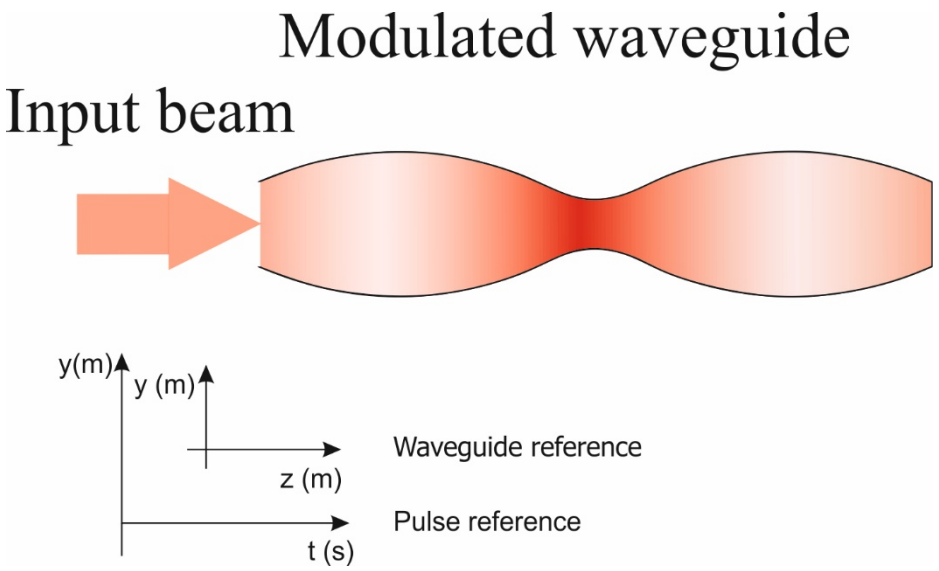

Figure 3.1 Schematic view of the intensity modulation of the pulse in space & time. From the point of view of the observer looking at the system from the lab coordination the modulation of the intensity of the pulse is special modulation along z axis, while the observer located on the pulse considers this periodic modulation in time.

As a result of this modulation, we expect to generate entangled photon pairs according to the dynamical Casimir effect at detuned frequency $\Delta\varpi_{DCE} = \pm\frac{\Omega}{2}$ with respect to the pump frequency, where Ω is the frequency of modulation seen by the pulse as an observer [60]. Using this concept, we prepare a dynamical Casimir like process, without using a temporal modulation of a cavity. We expect the generated photon pairs to increase in number along the waveguide length and, coupled into the waveguide mode, to thus produce a measurable intensity in the spectrum.

We use a nonlinear material as the substrate for the waveguide. As is described in section 1.3.4 for intense pulses the refractive index of the material can be considered as the combination of the linear and nonlinear part, and we also expect to have other third order nonlinear effects such as self-phase modulation (SPM). In 3.3 we will provide the results of numerical studies of the modulated waveguides for different pulse durations and periodicity of the modulation and intensities, which gives us references for the prediction of the frequency dynamical Casimir photon pairs.

3.1 Modulated waveguides in gallium lanthanum sulphide (GLS) substrate

3.1.1 Gallium lanthanum sulphide (GLS)

GLS is a member of chalcogenide glass family. The "chalcogens" include the elements of the group 16 in Mendeleev periodic table. Chalcogenide glasses contain at least one of the chalcogen elements. The density of the chalcogenide glasses is relatively high in comparison to the oxide glasses. Density of the GLS material is relatively high and therefore has a large refractive index ($n \approx 2-3$). The transmission window of the GLS is from the visible range to around five micrometres [61]. The atomic structure of the GLS is centrosymmetric, which means in normal conditions the second order nonlinearity vanishes in this nonlinear glass [62]. The third order nonlinear susceptibility for sulphide glasses is reported to be very large due to the high hyperpolarisability of the sulphide ions [63], [64]. The optical Kerr nonlinearity is reported to be about 35 times higher than silica [61]. The third order nonlinearity of GLS is reported to be around $1.189 \cdot 10^{-20}\ m^2 / V^2$ in literature [61]. The wavelength of the zero dispersion of the chalcogenide glasses is in the mid-infrared [65]. In comparison to other chalcogenide glasses, GLS has the most exciting nonlinear optical properties [66]. Given these outstanding optical properties of the GLS, we consider it as a suitable candidate for the waveguide substrate.

3.1.2 Numerical study results

We studied different modulation periodicities, amplitude of the modulation and different pulse durations in order to optimise the amplification of the dynamical Casimir effect side-bands. We used numerical simulations to predict the frequency of dynamical Casimir effect side-bands. These are based on the Pseudospectral spatial-domain (PSSD) technique, which is a variant of the finite-difference time-domain (FDTD) method. This code was developed in [67] where the details of the code can be found.

We first use a pulse duration of *500 fs* with *10 mm* propagation to demonstrate the Optical Wave Breaking (OWB) before searching for any dynamical Casimir effect side-bands as shown in Figure 3.2.

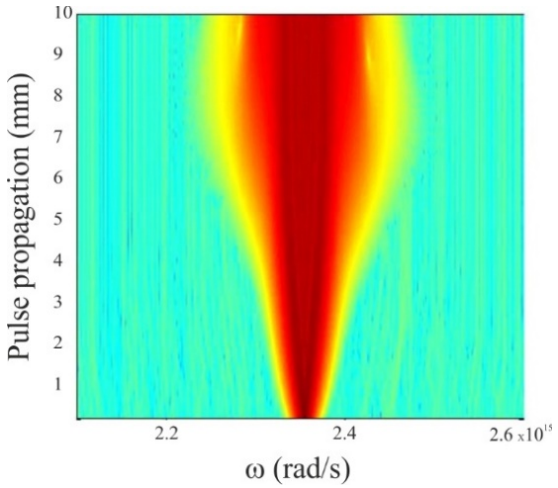

Figure 3.2 Optical wave-breaking in a 500 fs pulse [68].

To minimise OWB, we increase the pulse duration to the picosecond level and vary it between *1-5 ps*. Numerical simulations show clear dynamical Casimir side-bands outside of the OWB in the region of the *3* to *5 ps*. Figure 3.3 presents the Casimir side-bands for a 5 ps pump pulse duration along the *30 mm* of the propagation in a modulated waveguide with *200 μm* modulation wavelength.

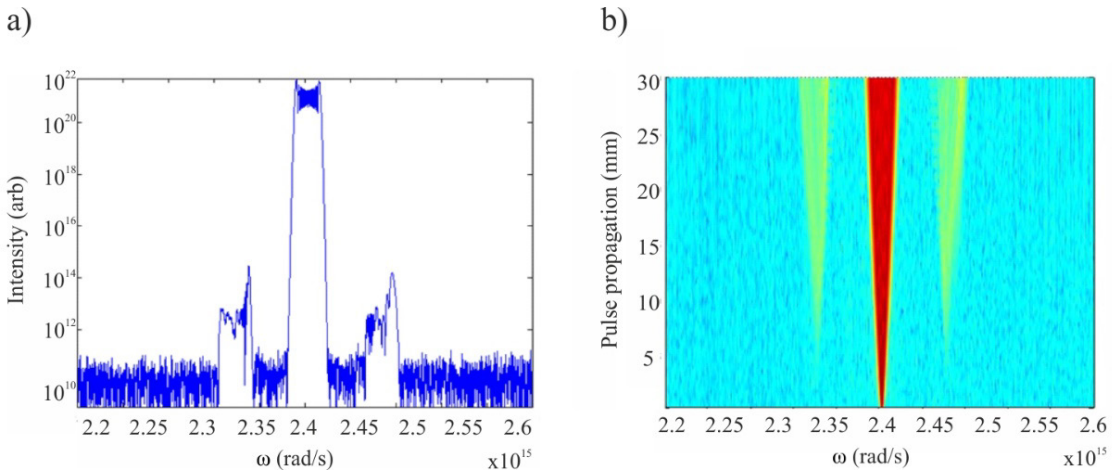

Figure 3.3 Simulation prediction for the Casimir side-bands in logarithmic scale (a). Colour map of the same result along the propagation in a modulated waveguide with *200 μm* modulation periodicity, along the 30 mm waveguide length (b) [68].

Figure 3.4 presents the result of the simulation for different modulation periodicities. We see that by increasing the modulation periodicity, the expected Casimir side-bands become more intense, while from the other side the position of these side-bands are more close to the pump frequency. The position of the side-bands is very important from the

experimental point of view as for detection of these side-bands we need to block the pump efficiently.

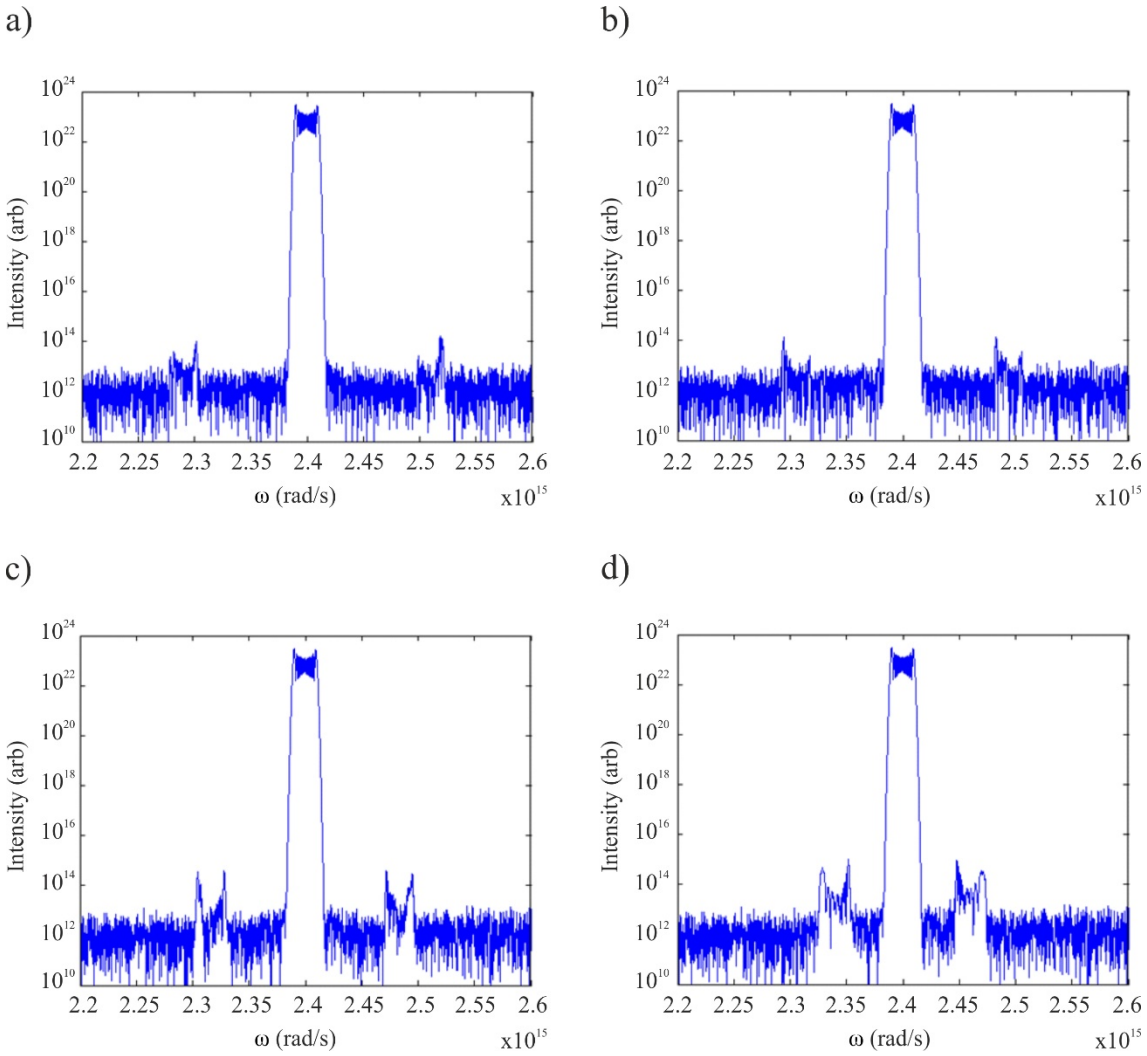

Figure 3.4 Logarithmic scale of the output spectrum of the 5 ps pulse with a peak intensity of $21.2\,GW/cm^2$ for different modulation periodicity. a),b),c) and d) respectively correspond to the 150 µm, 200 µm,250 µm, 450 µm of modulation periodicity along 30 mm waveguide length.

Once can see that by increasing the length of modulation periodicity, Casimir side-bands become stronger, however in the other hand the side-bands become closer to the pump. Experimental detection of these side-bands will be very difficult if we have them close to the pump. In Figure 3.5 we show the numerical simulation for the *4 ps* pulse duration for the *250 µm* and *450 µm* modulation periodicity. By comparing the results for the *5 ps* and

4 ps pulse durations for the same modulation periodicity we see dropping of the intensity of side-bands in *4 ps* pulse duration.

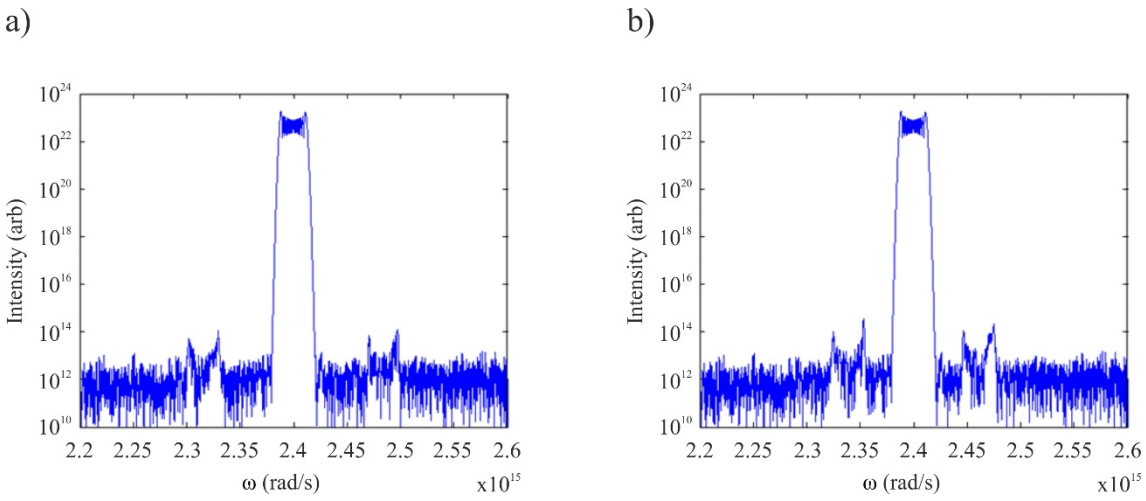

Figure 3.5 Logarithmic scale of the output spectrum of the 4 ps pulse with a peak intensity of $21.2\,GW/cm^2$ for 250 μm (a) and 450 μm (b) of modulation periodicity.

3.1.3 Experimental setup

As previously mentioned, for experimental studies we need ultrashort laser pulses with adjustable pulse durations in the picosecond regime. For this experiment we use a femtosecond laser pulse as the main source and then filter it with a spectral pulse filter setup [69]. Figure 3.6 shows the setup before optimisation. In this setup, we use just one high efficiency diffraction grating. We observe some unexpected peaks around the fundamental pump shown in Figure 3.7 at the end of the spectral pulse filter part. We discovered that the source of these peaks is the back reflection from the optical slit surface.

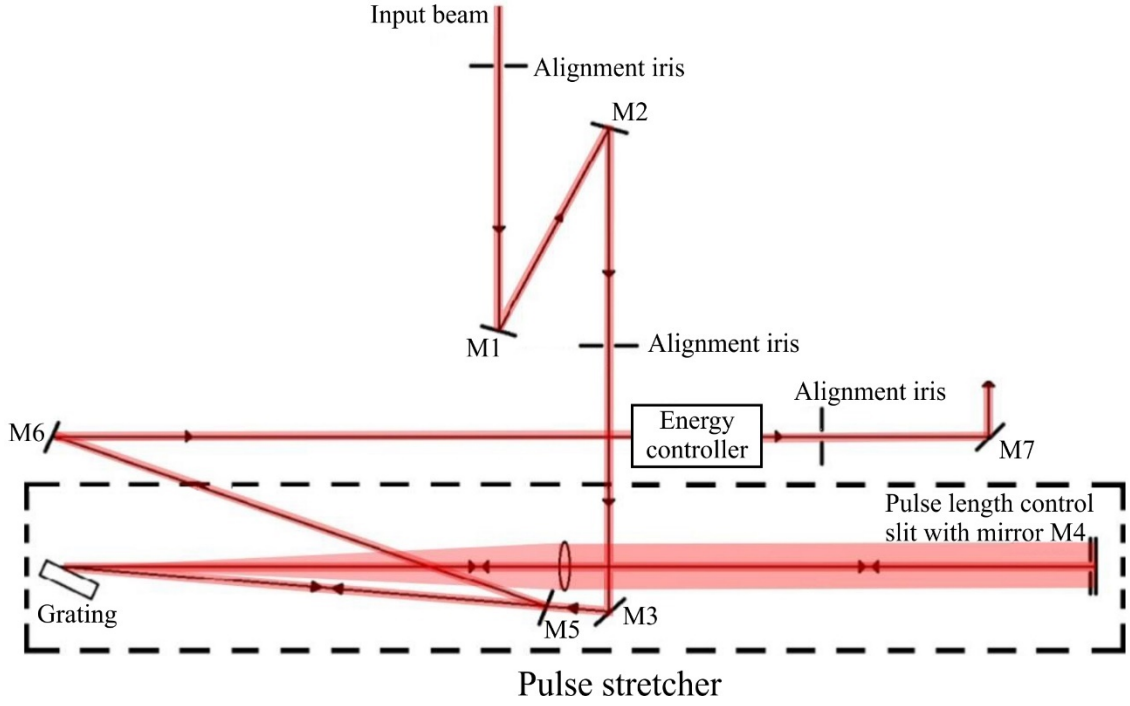

Figure 3.6 Schematic view of the compact spectral pulse filter setup by using one grating for spreading and collimating the spectrum.

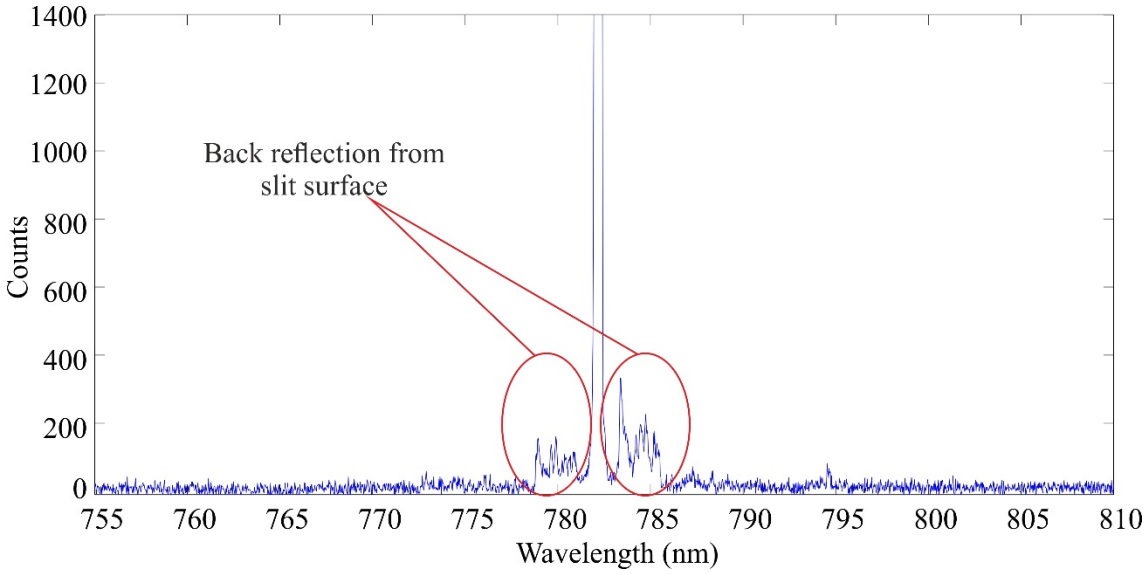

Figure 3.7 Spectrum of the output from the spectral pulse filter setup. In this spectrum, we see unexpected peaks around the fundamental peak at 758 nm.

To circumvent the problem, we improved the setup where we use two separate diffraction gratings, one to stretch the input spectrum and another one to collimate the transmitted (thus avoiding reflection problems) spectrum after the slit to get a clean spectrum in the output of the spectral pulse filter. We also increase the focal length of the lenses in order to stretch the spectrum wider and select a narrower part, which helps us to increase the

pulse duration. Figure 3.9 shows the pulse duration as a function of the slit size. Under the assumption that we have a Fourier transform limited pulse at the input and output of the pulse filtering system, we can measure the spectrum at the output and perform a Fourier transform, in this way we can retrieve the pulse duration.

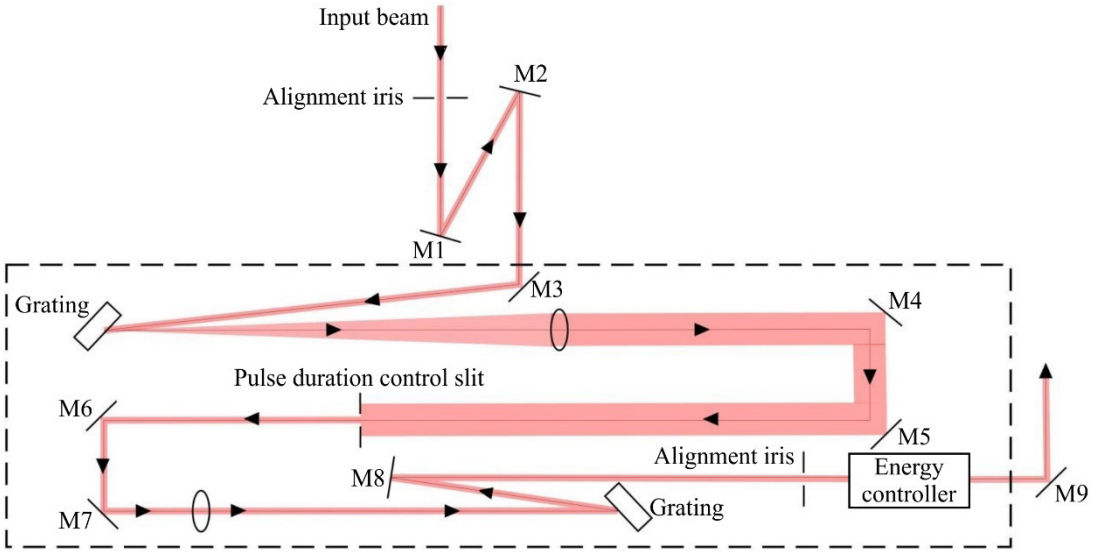

Figure 3.8 Developed setup of the spectral pulse filter. In this setup, there are two separated gratings for the stretching of the input spectrum and collecting of the selected spectrum.

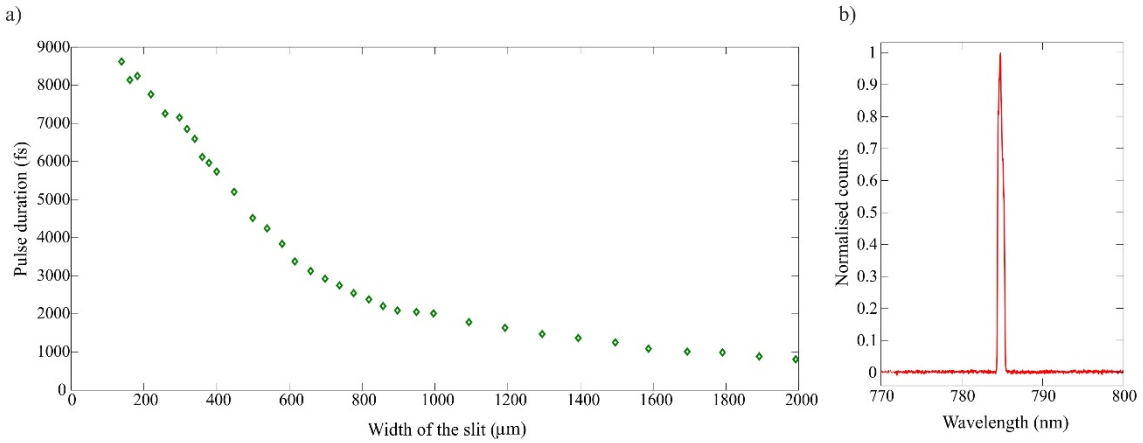

Figure 3.9 Pulse duration versus the width of slit. These data are taken from the setup demonstrated in Figure 3.8 (a), sample output spectrum from the setup in Figure 3.8 (b).

.

After choosing the pulse duration, we couple the pulses into the waveguide. The coupling system consists of a focusing lens on the linear 3D translation stage and the waveguide is placed on a 4D (X-Y, pitch and yaw) stage. A collection/collimating lens after the waveguide is also on a 3D linear stage. The coupling to the waveguide is quite challenging as the modulated waveguide's coupling and transmission efficiency depends sensitively on the perfect coupling conditions. When coupling to the waveguide is correct, we should be able to couple form one waveguide to another one just by moving the waveguide in X direction. Figure 3.10 demonstrates the waveguide coupling part of the setup.

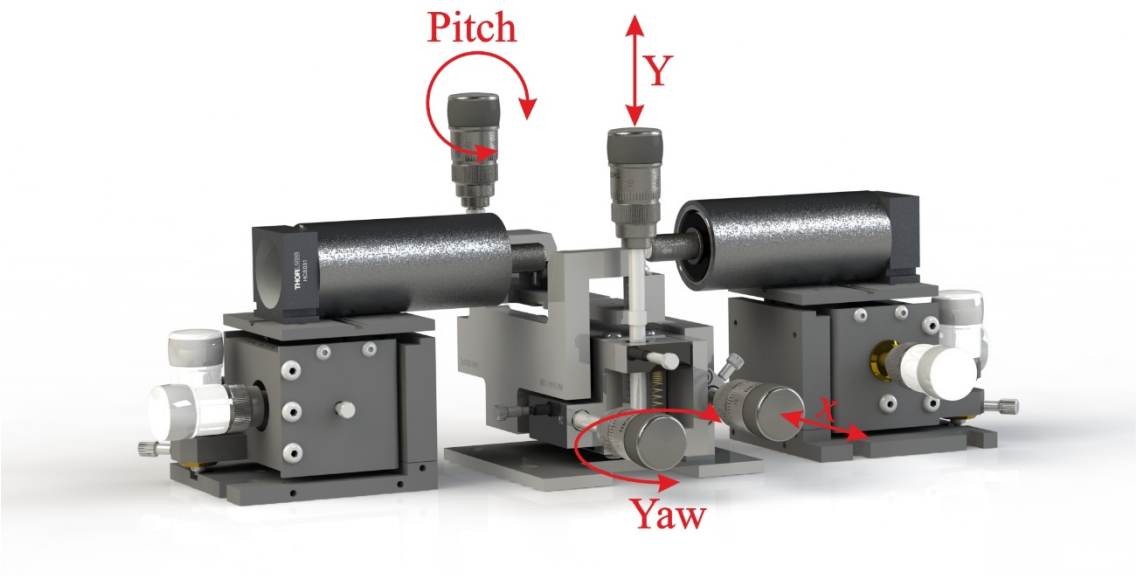

Figure 3.10 Waveguide coupling setup. In the perfect coupling conditions, we need to use the x-axis adjustment to move from one modulated waveguide to another one and keep the coupling efficiency at the maximum.

3.1.4 Waveguides specifications

We use GLS, which has a very high third order nonlinear susceptibility ($\chi^{(3)} = 1.189 \cdot 10^{-20}\, m^2/V^2$) in comparison to the other available materials. The main disadvantage of this material is the limited size of the substrate in length, which is indeed very important in this experiment.

The waveguides on the GLS substrate are made in collaboration with Dr. Robert Thomsons' research group at Heriot Watt University. These waveguides were prepared using the ultrafast laser inscription (ULI) technique. Davis et al. presented this technique in 1996 [70]. The technique found a wide range of application in fabrication of integrated

optical devices such as waveguides in bulk media. ULI is a nonlinear process, in which sub-bandgap absorption of photons causes an irreversible structural change to the material [71]. An ultrafast laser beam is focused inside the bulk material. By selecting the right energy and parameters of the inscription laser pulses, the nonlinear absorption in the medium can exhibit a positive change of the refractive index [71]. Figure 3.11 shows a schematic view of the ULI system. The setup consists of an objective to focus the ultrafast laser beam and an x-y-z linear translation stage to position the substrate. The position of the objective is fixed and in order to fabricate the waveguide the position of the substrate is changed by the translation stage.

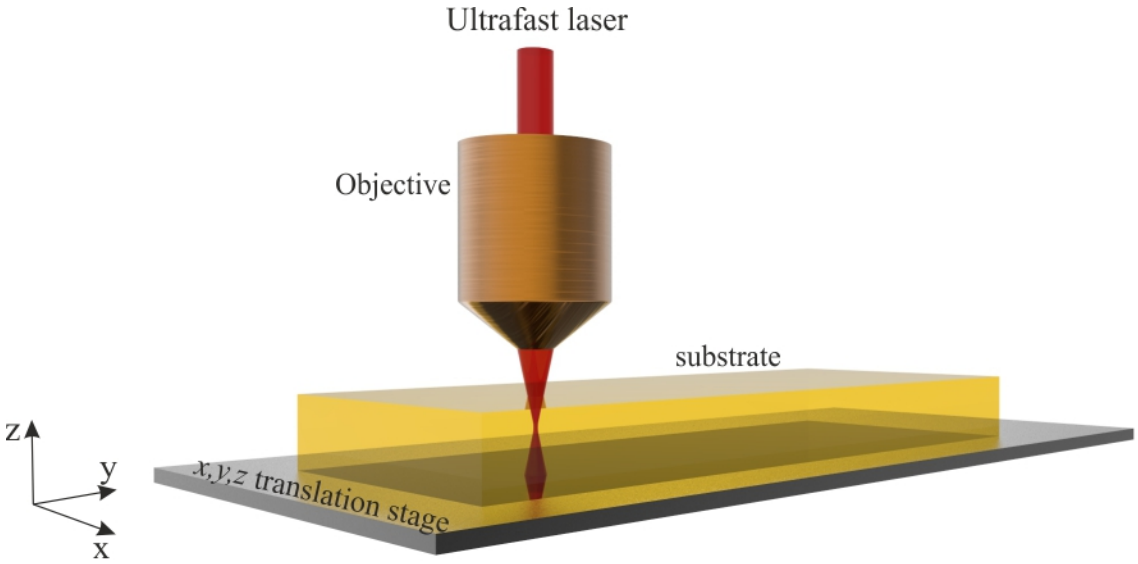

Figure 3.11 Schematic view of the ultrafast laser inscription.

Figure 3.12 (a&b) demonstrate the different type of waveguides under microscope. In Figure 3.12 (a) the waveguide is made by performing 200 laser writing scans along the waveguide and thus change the refractive index accordingly. We refer to this type of waveguide as "modulated waveguide". However, in Figure 3.12 (b) we have 10 laser writing scans along the each side of the boundary of the waveguide. We refer to this type of wavguides as " splitting waveguides". Using these two different methods of writing affect the coupling efficiency. The coupling efficiency of the sample in Figure 3.12 (b) is also very sensitive to the input beam's polarisation. We achieve better coupling efficiency when the input beam is linearly polarised and the polarisation is parallel to the modulation axis. Figure 3.12 (c&d) schematically present two methods of the writing methods of the waveguides in Figure 3.12 a&b.

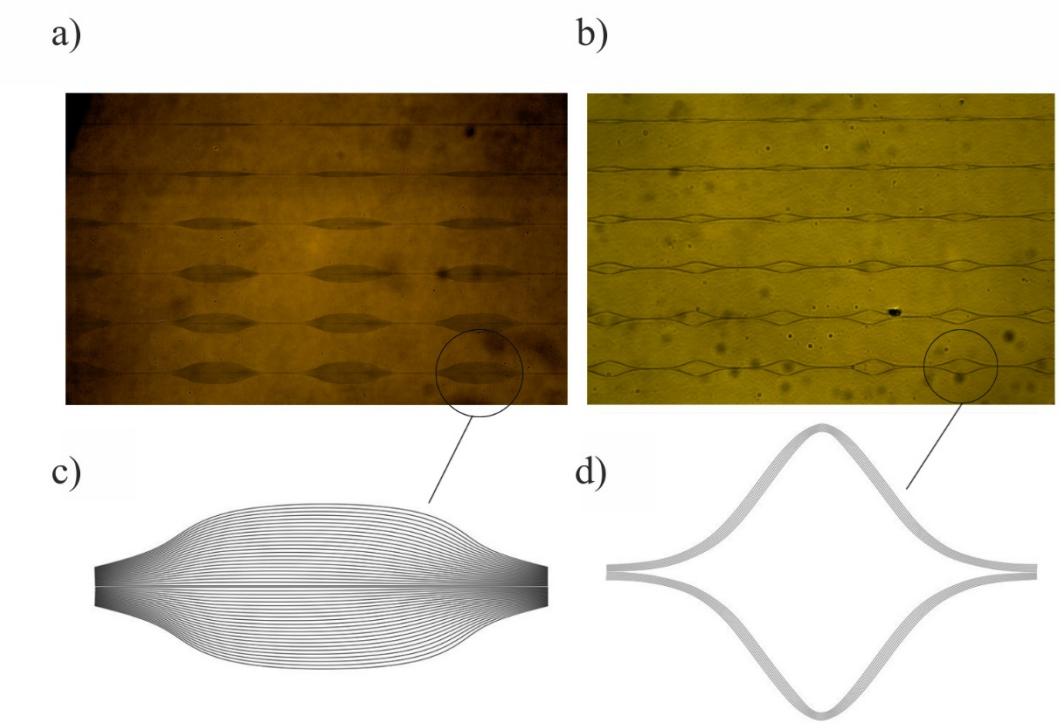

Figure 3.12 The modulated waveguides with same modulation periodicity and different modulation amplitude (0, 12, 16,24, 28 μm) (a), Splitting waveguides with different modulation periodicity (150, 200 and 250 μm) and amplitude (0, 12, 16, 24, 28, μm) (b), modulated waveguides schematic writing method (c), Splitting waveguide schematic writing method (d).

We expect different coupling efficiency from *5%* to *50%* for different waveguides depending on the modulation periodicity and amplitude of modulation. Figure 3.13 presents the expected coupling efficiency for different sets of splitting waveguides. Reflection loss is also considered for the calculation of the insertion loss.

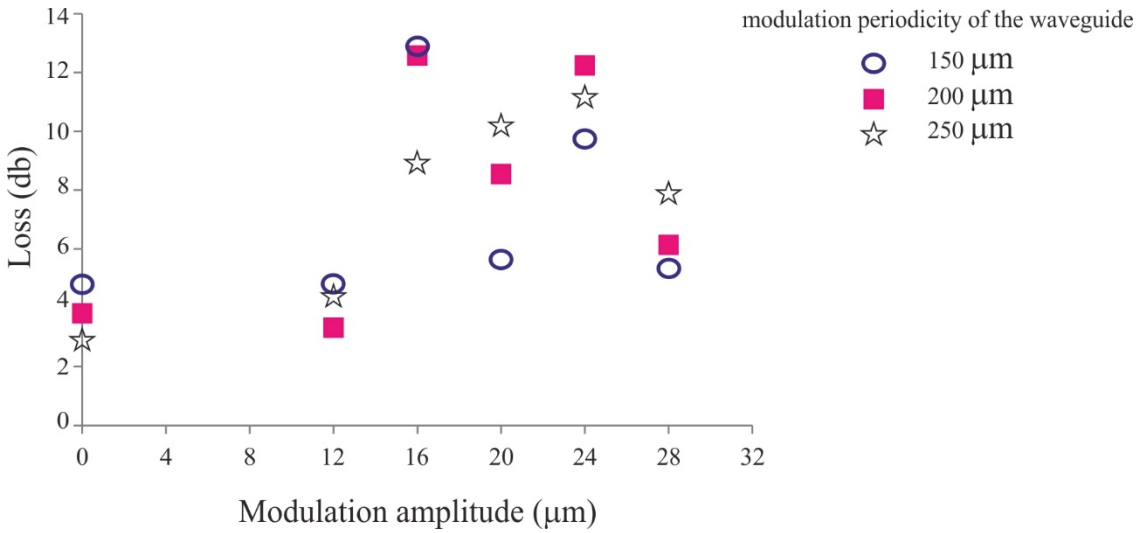

Figure 3.13 Theoretical calculation of the loss in waveguide as a function of modulation periodicity and modulation amplitude. Data are from [72].

After the coupling system, we use a flip mirror to keep the control on the coupling efficiency and the correct coupling mode. If the coupling is perfect, we see the profile of the output from the waveguide as in Figure 3.14 (a). This mode and profile should be observed for each waveguide in this sample. In Figure 3.14 (b) we observe non-Gaussian profile along the horizontal axis. We see similar profiles for all waveguides with amplitude of modulation higher than 16 µm. This effect corresponds to the modulation of the waveguide along the propagation direction and strongly affect the coupling efficiency. We consider the waveguide as a defected waveguide if the output profile looks like the Figure 3.14 (c).

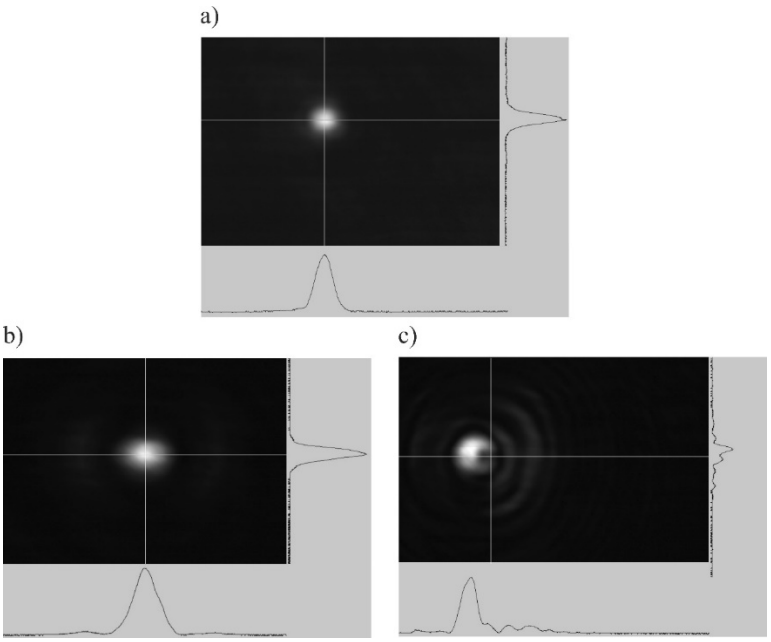

Figure 3.14 Profile of the output beam of the modulated waveguide in ideal coupling conditions (a) output profile of the beam from the waveguides with modulation periodicity higher than 16 µm (b) output profile from the defected waveguide (c).

Figure 3.15 demonstrates the mode field diameter of the waveguides on GLS samples. For different waveguides and different methods of writing the relative deviation of the mode field diameter is ±*10%* of this measured value.

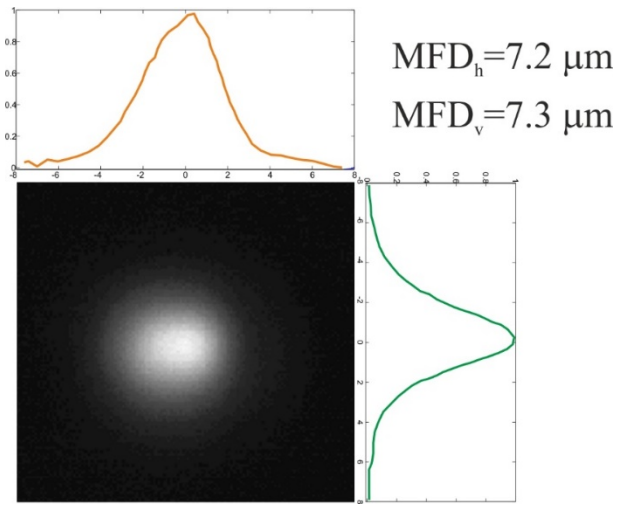

Figure 3.15 Mode field diameter of the waveguide.

3.1.5 Experimental coupling efficiency and damage threshold

The theoretical loss in the waveguides is calculated to be between *3* to *13 db*, which is equivalent to in-out coupling efficiency from *5%* to *50%*. In contrast to the theoretical

calculation the minimum insertion loss for the modulated waveguide is *7 db.* This value is for the waveguide with *200 μm* modulation periodicity and *12 μm* amplitude of modulation. First of all, our aim is to measure the damage threshold for our substrate in our experimental conditions for our pulse duration. We characterise the damage threshold for the GLS sample for different pulse durations in the picosecond regime with 100 Hz repetition rate in Figure 3.16.

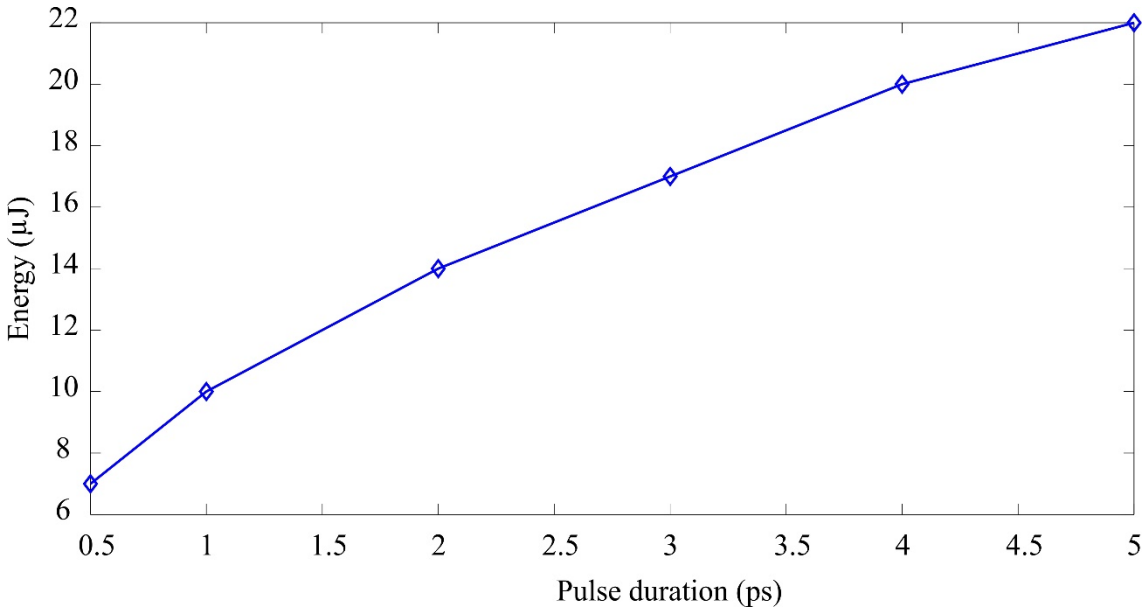

Figure 3.16 Damage threshold for different pulse duration. The repetition rate of the laser is 100 Hz.

Figure 3.17 (a) shows the surface of the polished waveguides under a microscope. In Figure 3.17 (b) we can see the damaged surface of the waveguides under a continued exposure of the pulsed beam. The surface damage threshold of GLS is significantly less than the bulk threshold. Hence this damage of the surface can be easily removed by polishing the surface of the sample, which indeed is an advantage for this substrate.

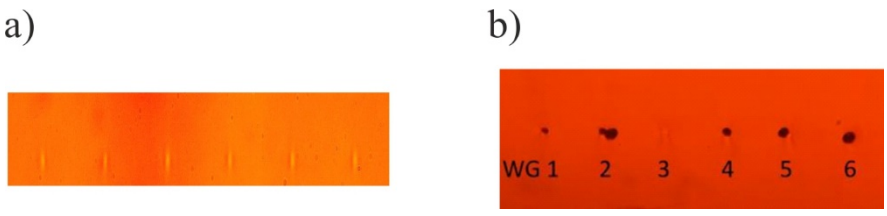

Figure 3.17 Image of the polished surface of the waveguides under microscope (a) Image of the damaged surface of the waveguides under microscope. These damages are removable by polishing the damaged surface (b).

3.1.6 Self-phase modulation in waveguides

As we discussed in 3.1.1 modulation of the intensity in a nonlinear medium leads to the number of nonlinear effects. From a theoretical point of view, we know that the generation of entangled photon pairs from the vacuum state is a less probable effect in comparison to the third order nonlinear effects as SPM and OWB. The numerical study of the intensity modulation along the propagation in 3.1.1 also confirms the SPM and OWB. Hence we start our measurement from the SPM measurement of the spectrum in both straight and modulated waveguides. Figure 3.18 shows the SPM for modulated waveguides and straight waveguide for a *5 ps* pulse duration. As one can see the blue shifting of the spectral broadening of the pulse looks stronger than the red shifting of the SPM broadening. This is due to dispersion that creates a steeper trailing edge in the pulse and thus pulse broadening that is stronger to the blue side. Figure 3.18 (a) corresponds to the SPM in a modulated waveguide with a *150 μm* modulation periodicity and *12 μm* amplitude of the modulation, while the (b) corresponds to the *150 μm* modulation periodicity and *24 μm* amplitude of the modulation. By comparing Figure 3.18 (a&b) one can see that the amplitude of modulation does not seriously affect the quality and properties of the SPM. We also see that the SPM broadening does not depend on the modulation periodicity if we compare Figure 3.18 (a, d and e), corresponding to the *150 μm, 200 μm* and straight waveguide.

Coupling efficiency for the waveguides in Figure 3.18 (a, b, c, d and e) are respectively *22%, 20%, 13%, 21%* and *25%*. In contrast to the simulation results (Figure 3.4), one can see that the spectrum broadening for the pulse duration for the given modulation in experimental measurement is about *20* times less than the numerical simulation. This can be explained by our limitation in the pump intensity because of the damage threshold and the insertion loss, which is minimum *80%* in our waveguides.

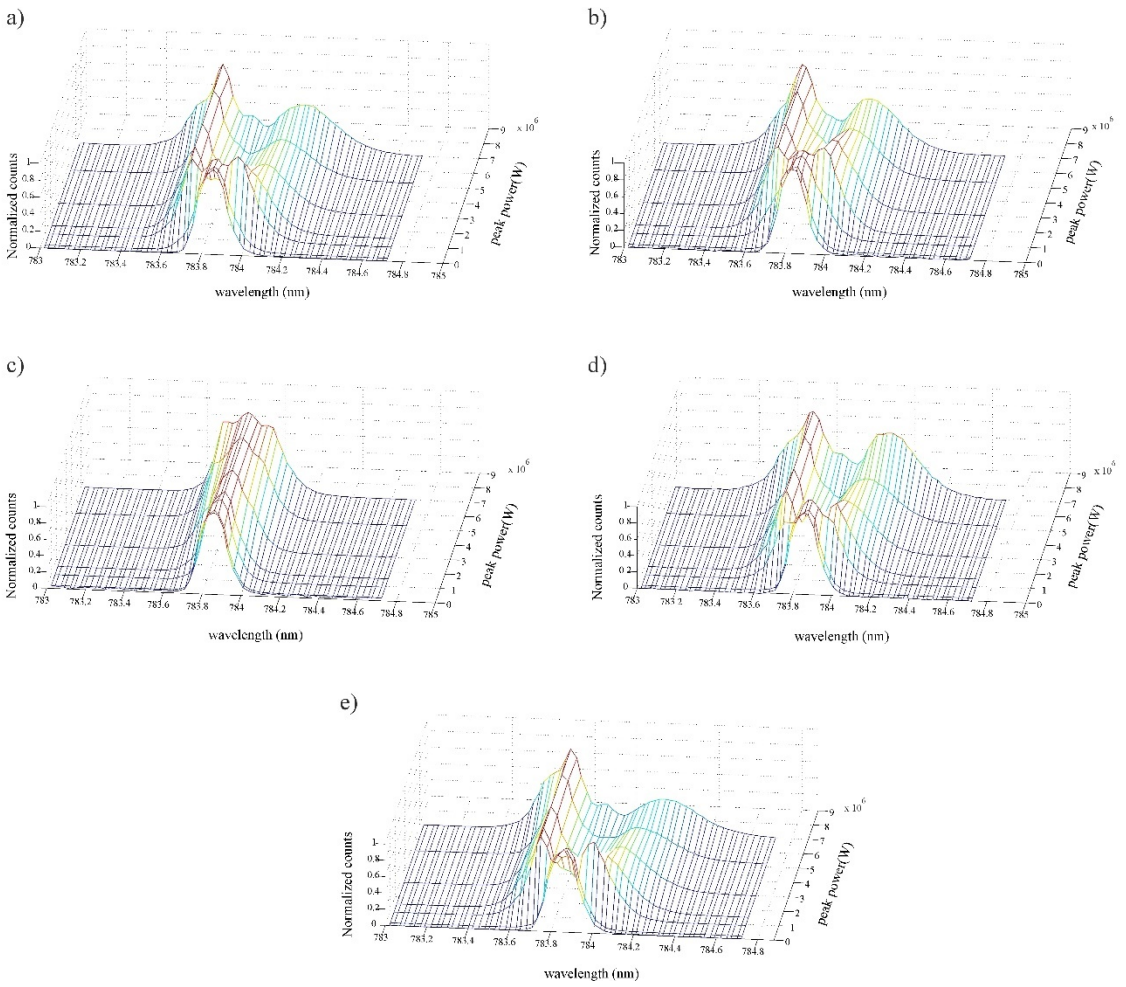

Figure 3.18 Self-phase modulation for different waveguides with a pulse duration of 5 ps. SPM for modulated waveguide with 150 µm modulation periodicity and 12 µm of modulation amplitude (a) SPM for modulated waveguide with 150 µm modulation periodicity and 24 µm of modulation amplitude (b) SPM for modulated waveguide with 200 µm modulation periodicity and 12 µm of modulation amplitude (c) SPM for modulated waveguide with 250 µm modulation periodicity and 12 µm of modulation amplitude (d) SPM for straight waveguide (e).

We also studied the SPM for modulated waveguide for different pulse duration of the pump. Figure 3.19 shows the spectrum broadening for the modulated waveguide with *150 µm* and *12 µm* of the modulation amplitude.

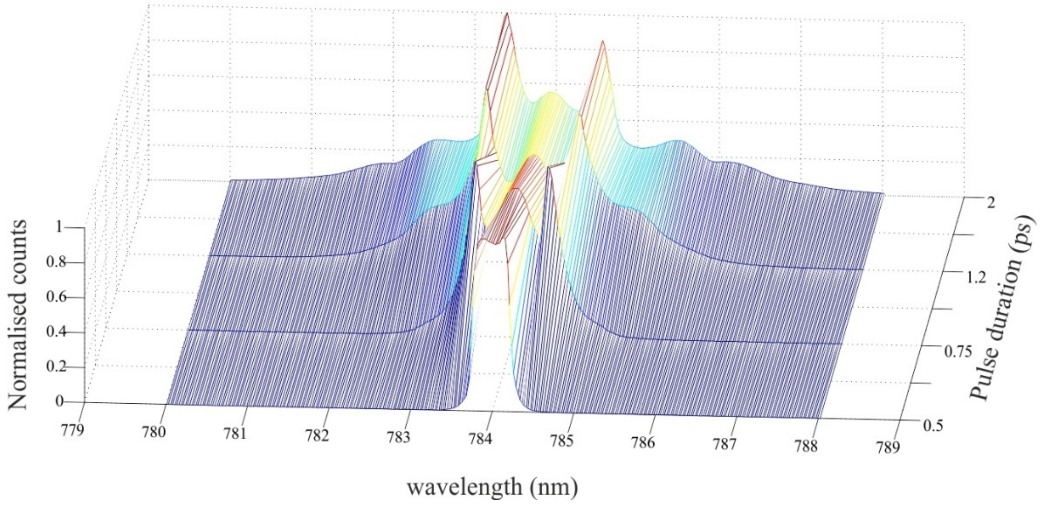

Figure 3.19 Spectrum broadening in the output of the modulated waveguide with 150 µm modulation periodicity and 12 µm of the modulation amplitude under 0.5, 0.75, 1.2 and 2 ps pulse duration of the pump beam.

Figure 3.20 presents the cross-corrleation map of the SPM for *2 ps* pulse duration and peak intensity at *7 MW*. By looking at all the data, our conclusion is that in experimental condtions we have less spectral broadening of the pulse than expected.

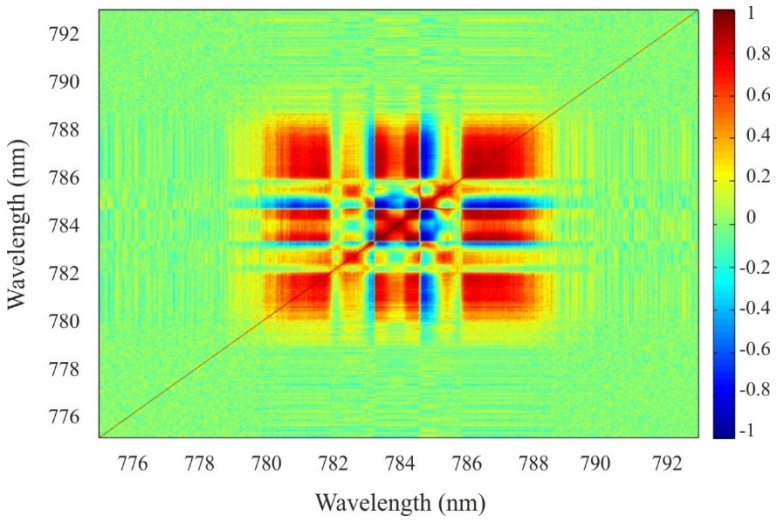

Figure 3.20 Cross-correlation map of experimental measurement of the SPM in modulated waveguide with modulation periodicity of 150 µm and 12 µm amplitude of the modulation. The pump pulse duration is 2 ps.

3.1.7 Dynamical Casimir effect in side-bands measurement

Although the nonlinear effects such as SPM in experimental measurements are about 1 order of magnitude less than in numerical results, we still tried to measure the DCE side-bands.

Figure 3.21 presents the spectrum of the output from the modulated waveguide with 150 µm modulation periodicity and 1*2 µm* modulation amplitude. Pulse duration for this experiment is *5 ps*. This measurement is performed with an Andor EMCCD in *5 minutes* integration and *800* of EM gain and peak laser pulse power at *7 MW*. We use two notch filters to block the pump with optical density (OD) *12*. Literature confirms the existence of Raman shift for GLS around *806 nm* for the pump wavelength at *785 nm* [73]. We suppose that the DCE side-band in red side is covered by the Raman peak. As for different waveguides with different modulation periodicity we see a similar spectrum in the output, we subtract the spectrum of *150 µm* from the output spectrum of the modulated waveguide with *250 µm* and same amplitude of modulation equal to *12 µm*. Figure 3.22 presents the subtracted spectrum of two modulated waveguide with *150 µm* and *250 µm* modulation periodicity and same pump energy for *60 min* integration time. As we expect a shift in the position of side-bands by changing the modulation periodicity, the aim of this measurement is to extract a peak from this subtraction and remove the Raman shift and possible photoluminescence, which simply depends on the material rather than the modulation periodicity. For a given pump power we expect to have a similar Raman and photoluminescence but different position of the DCE side-bands. We clearly see no indication of any peak in the region of interest.

Notwithstanding that the high $\chi^{(3)}$ in GLS plays an important role and DCE side-bands gain from it, the dimensional limitation of the raw material for the substrate, which is *30 mm* in length restricts the increase of modulations along the propagation, which leads to the limitation of the modulation periodicity as well. All these limitations lead us to try another material as a substrate for the modulated waveguides.

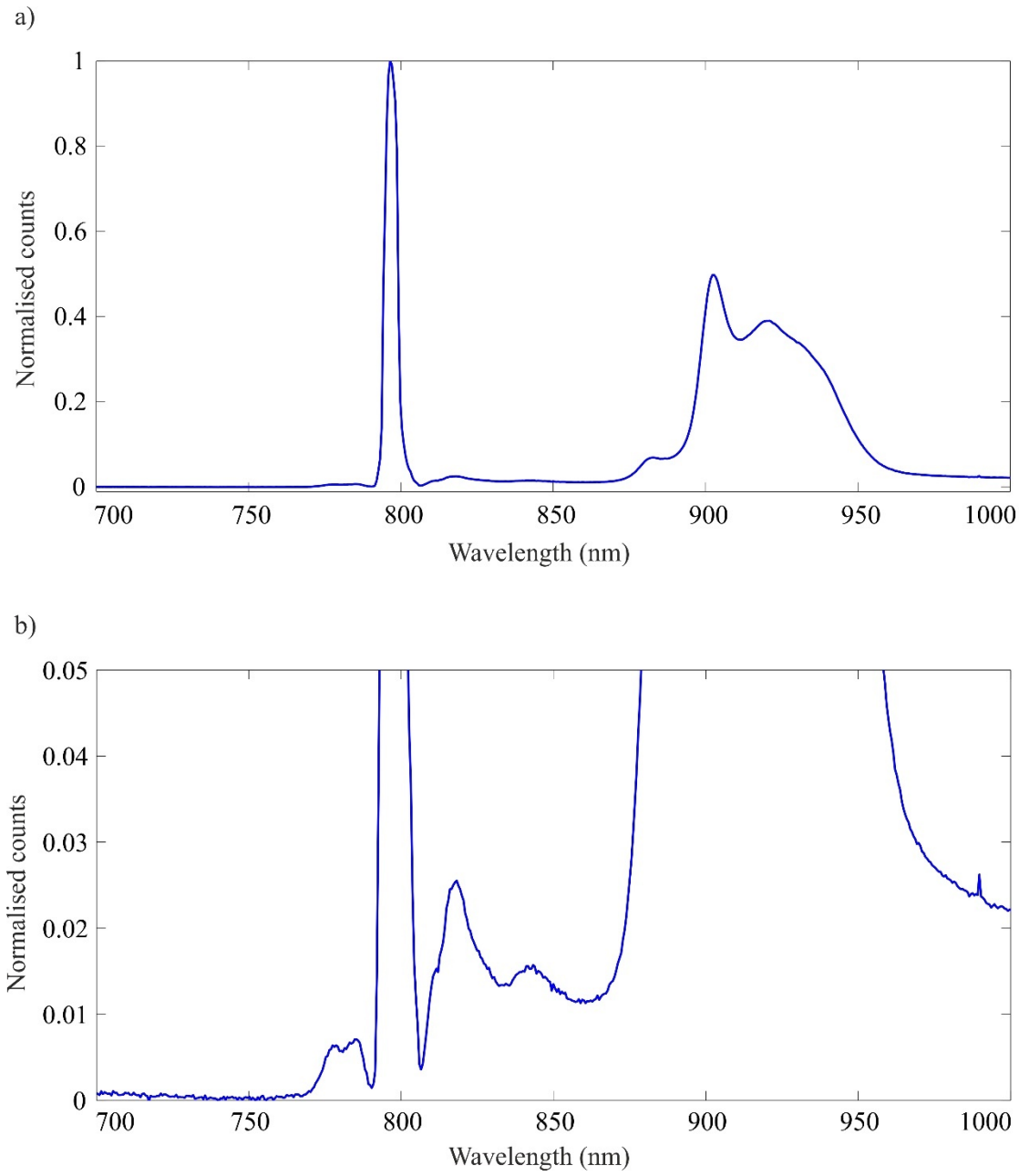

Figure 3.21 Measured spectrum of the output from the modulated waveguide with 150 µm modulation periodicity and 12 µm modulation amplitude (a), zoomed presentation of the same spectrum (b).

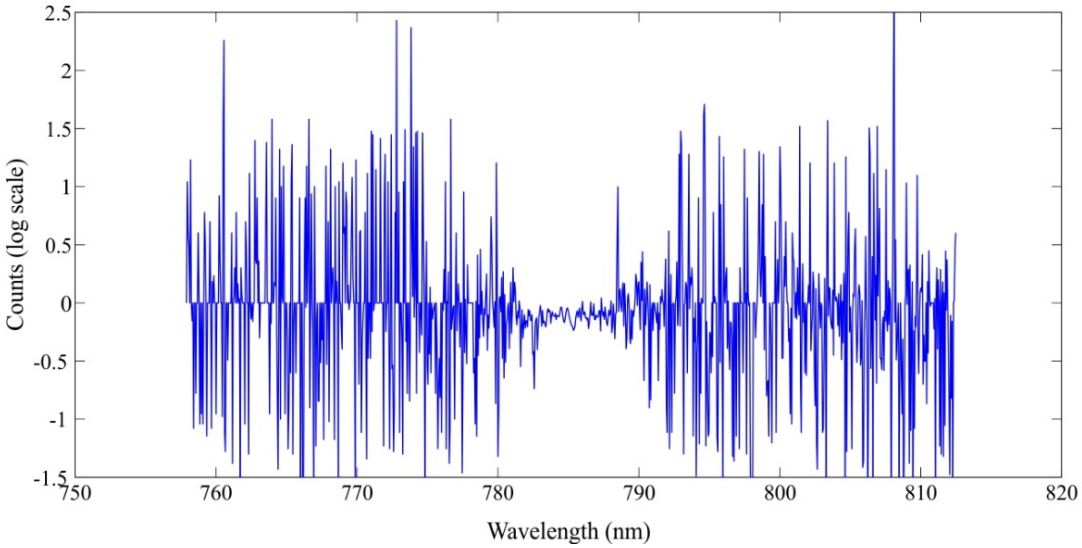

Figure 3.22 Subtracted spectrum of the waveguide with 250 µm modulation periodicity from the spectrum of the waveguide with 150 µm modulation periodicity. The amplitude of modulation is the same for both waveguides and is equal to 12 µm.

3.2 Modulated waveguides in fused silica substrate

All mentioned limitations in 3.1.6 led us to try fused silica as a substrate for the modulated waveguides. In contrast to GLS, using fused silica as the substrate material makes it possible to increase the waveguide length up to *100 mm*. It helps us to increase the number of modulation and modulation periodicities. Another advantage of fused silica in comparison to GLS material is its well-known optical properties and higher damage threshold level, which makes it possible to increase the pump power.

3.2.1 Waveguides specifications

Our modulated waveguides on fused silica substrate are made by Dr. Simon Stutzer (working in the Szameit group) at University of Jena in Germany. The structure of this sample is different from the structure and method of writing for the GLS sample. The waveguide structure is shown in the figure below: it is composed of two coupled structures, one is straight and the other one is sinusoidal modulated section. These structures behave as a coupled waveguide system, where the electric field along the waveguide can be expressed as a combination of the even and odd modes of the overall waveguide [74].

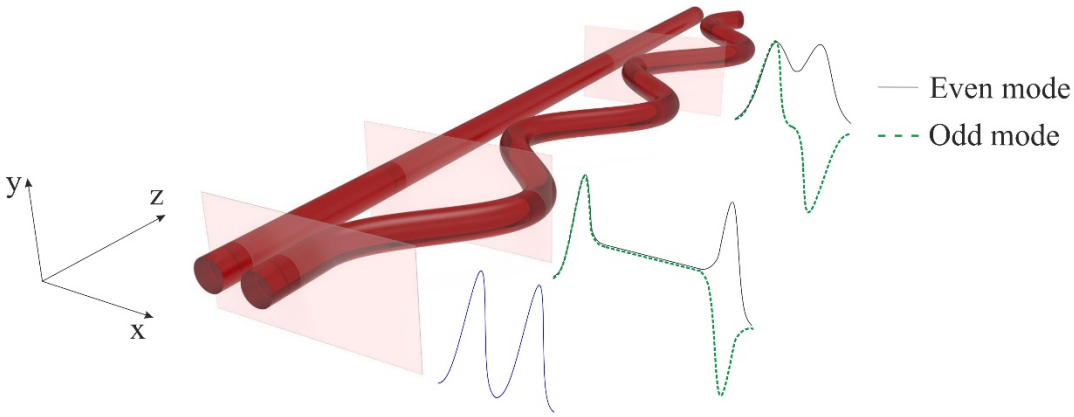

Figure 3.23 Schematic view of the coupled waveguides system. Distribution of the electric field is presented for three different sections of the waveguide Blue colour corresponds to the electric field in the input of the waveguide.

The main difference compared to the GLS waveguides is the modulation of just one of the waveguide (see Figure 3.23). In this sample, we have waveguides with modulation periodicity *400 μm,450 μm, 500 μm, …, 1000 μm* modulation periodicities and *2, 3, 4, 5, 6 μm* amplitude of modulation and 9 straight waveguides pairs. The separation between straight waveguides is different and varies from *6 μm* to *14 μm*. The separation between straight and modulated waveguide in each pair for the coupler part is *60 μm*.

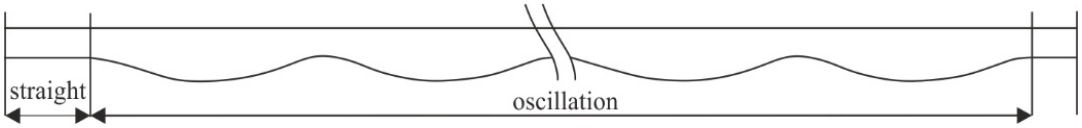

Figure 3.24 Schematic view of the modulated waveguide in the fused silica substrate. The waveguide consists of two waveguides with separation of 60 μm in the straight part (coupler part) between straight and modulated one. We have modulated waveguides with 400 μm,450 μm, 500 μm, …, 100 μm modulation periodicities and 2, 3, 4, 5, 6 μm amplitude of modulation.

In Figure 3.25 the flourescence image for the waveguide along the *99 mm* of propagation is demonstrated. One can see the uniform propagation and distribution for both sides along the waveguide.

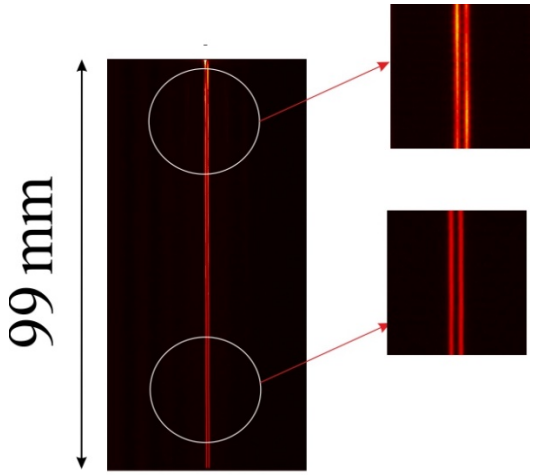

Figure 3.25 Fluorescence image of the straight waveguide along the 99 mm of propagation.

In Figure 3.26 we demonstrate the fluorescence image for waveguides. As one can see the bended waveguides lead to radiation losses, which strongly depends on the amplitude and the modulation periodicity. In comparison to the Figure 3.25 we see that the modulated waveguides experience a high loss along propagation. It is mainly because of the modulation along the propagation [75]. We see that increasing the modulation periodicity also increase the radiation loss and after *99 mm* propagation the coupling efficiency of the waveguides strongly drops.

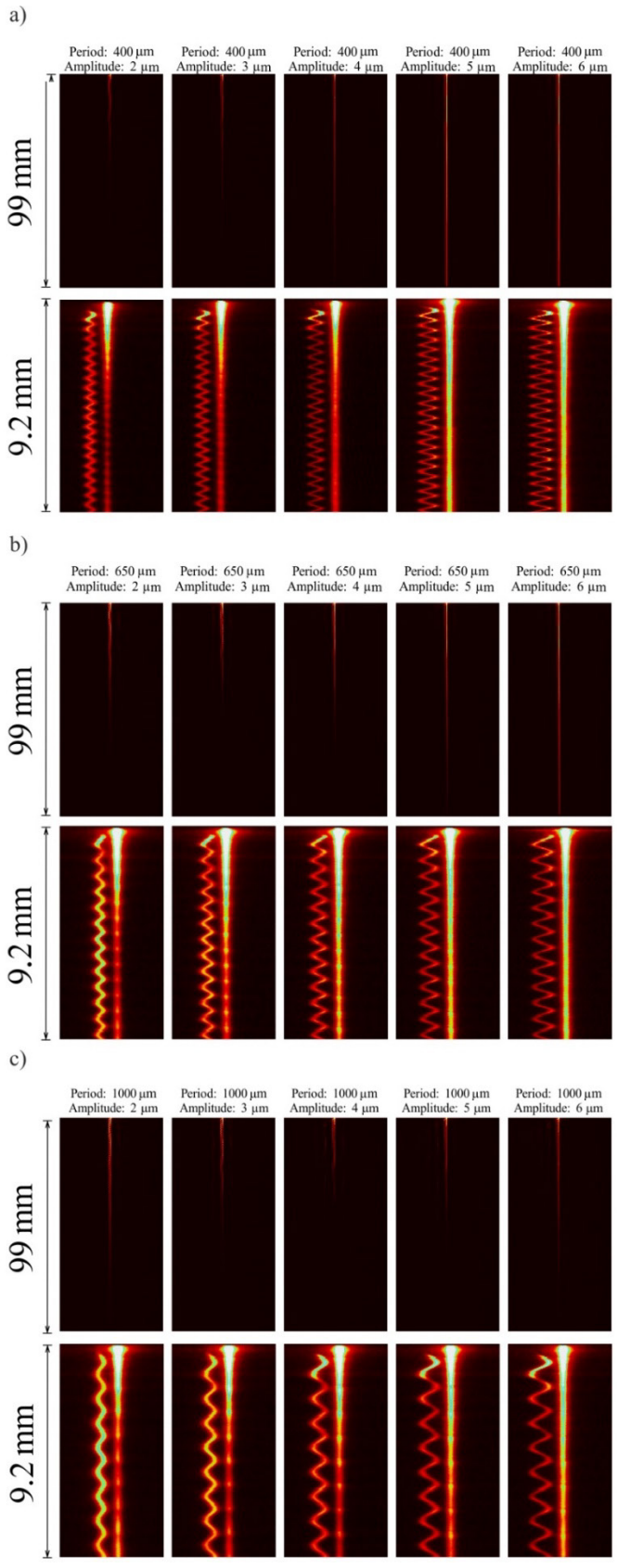

Figure 3.26 Fluorescence image of the modulated waveguides with 400 µm (a), 650 µm (b) and 100 µm (c) modulation periodicity and 2, 3, 4, 5, 6 µm amplitude of modulation.

3.2.2 Experimental coupling efficiency and SPM measurement

For these waveguides in best coupling conditions we achieve up to *30%* coupling efficiency and *18%* coupling efficiency for the modulated waveguide. We achieved the maximum coupling efficiency for the modulated waveguide with *400 μm* modulated periodicity and *6 μm* modulation amplitude. We use *300 fs* pulse duration with *40 MW* peak power for this measurement.

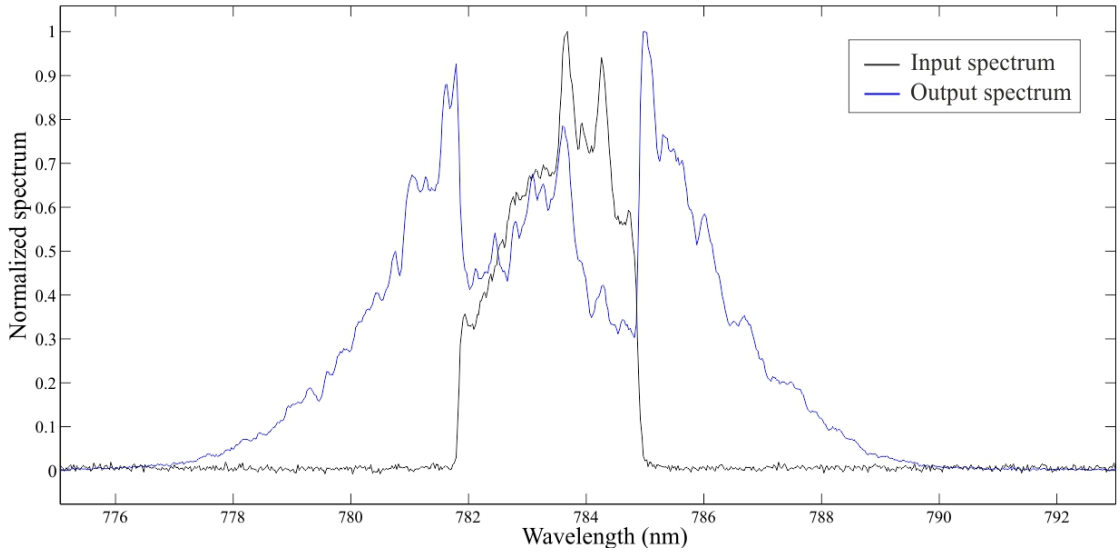

Figure 3.27 Self-phase modulation for the modulated waveguide with 400 μm modulation periodicity and 6 μm modulation amplitude. This SPM is measured for the pulse duration of 0.3 ps pulse duration and 28 MW peak power.

For the given input pulse spectrum with *0.3 ps* pulse duration and given peak power after *99 mm* propagation, we expect to measure *27 nm* of SPM at FWHM instead of *5.5 nm* of spectrum broadening in Figure 3.27. Figure 3.28 presents the numerical calculation of the SPM for given spectrum and pulse characteristics. Figure 3.29 presents the output profile of the straight waveguides. We use this data to find the effective area for each waveguide and compare it with SPM in each waveguide. We also measure the spectral broadening for all straight waveguides in the sample. We keep the peak power fixed for all waveguides. Figure 3.30 (a) demonstrates the SPM for straight waveguides, while Figure 3.30 (b) presents the measured value of the $1/A_{eff}$ for each waveguide. We clearly see that the spectrum broadening is proportional to this value. However, the SPM is still less than our expected value even for straight waveguides. From previous experience with GLS sample, without sufficient SPM occurring, we can immediately conclude that there is

insufficient nonlinearity to observe DCE. We therefore do not proceed with further measurements but instead shift attention to a third kind of waveguide as explained in the following section.

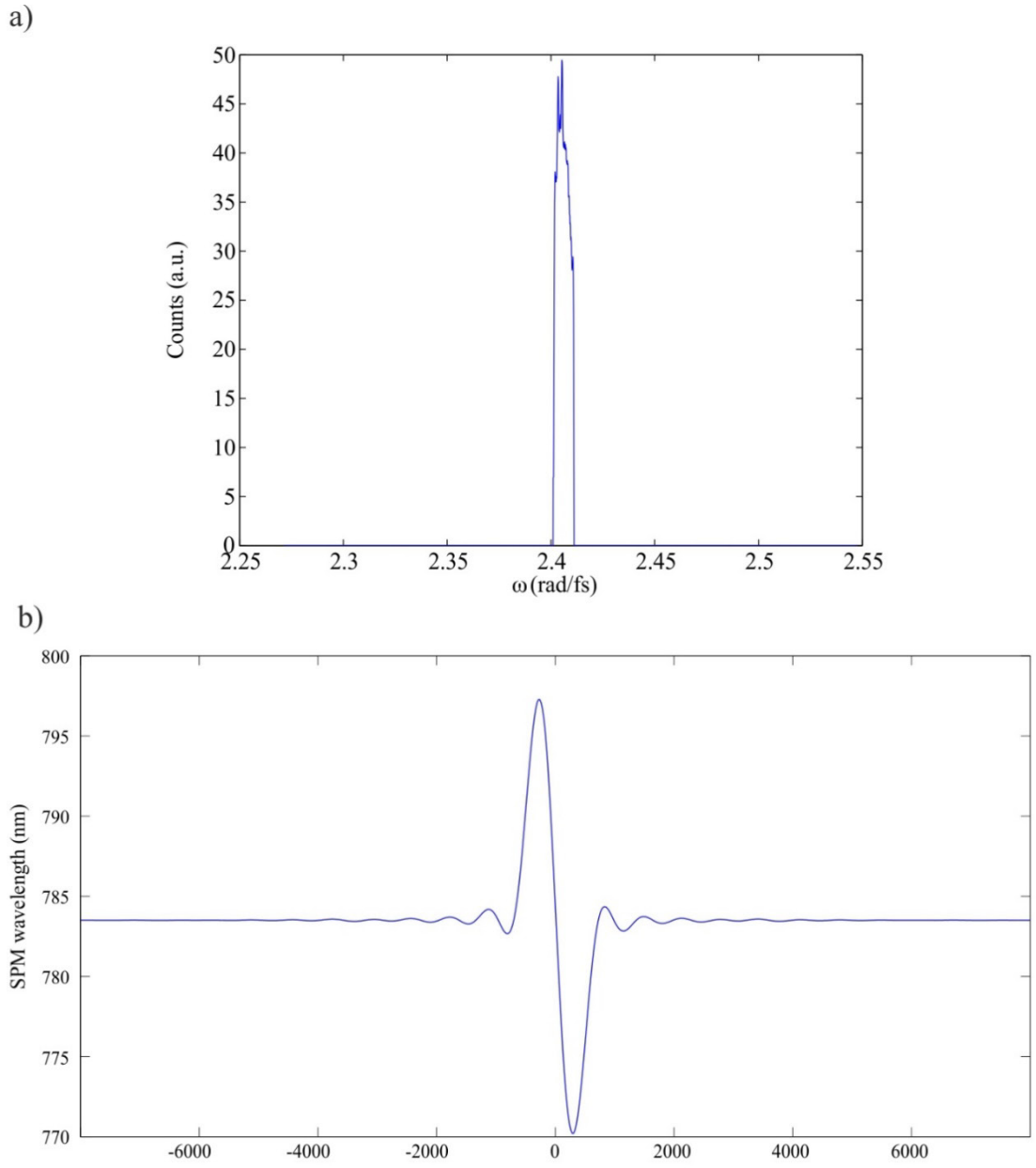

Figure 3.28 Theoretical calculation of the SPM for the given input spectrum and 40 MW peak power along 99 mm propagation. Input spectrum (a) calculated SPM for the given parameters (b).

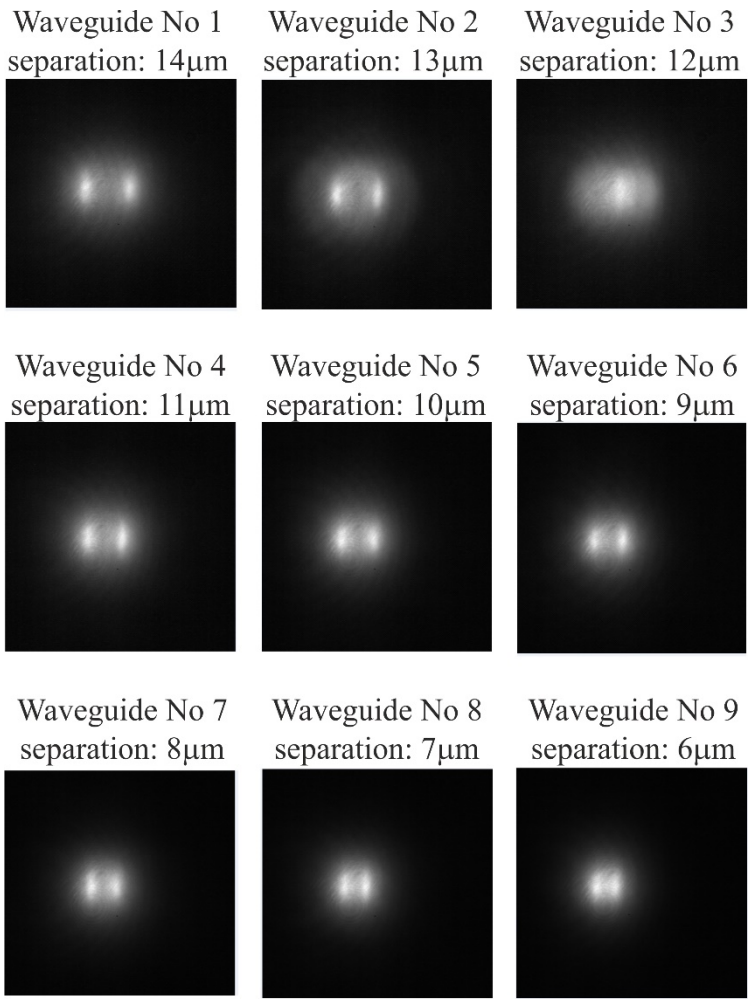

Figure 3.29 Output profile of the straight waveguides. We use the same pulse duration (300 fs) and peak power for all waveguides (40 MW).

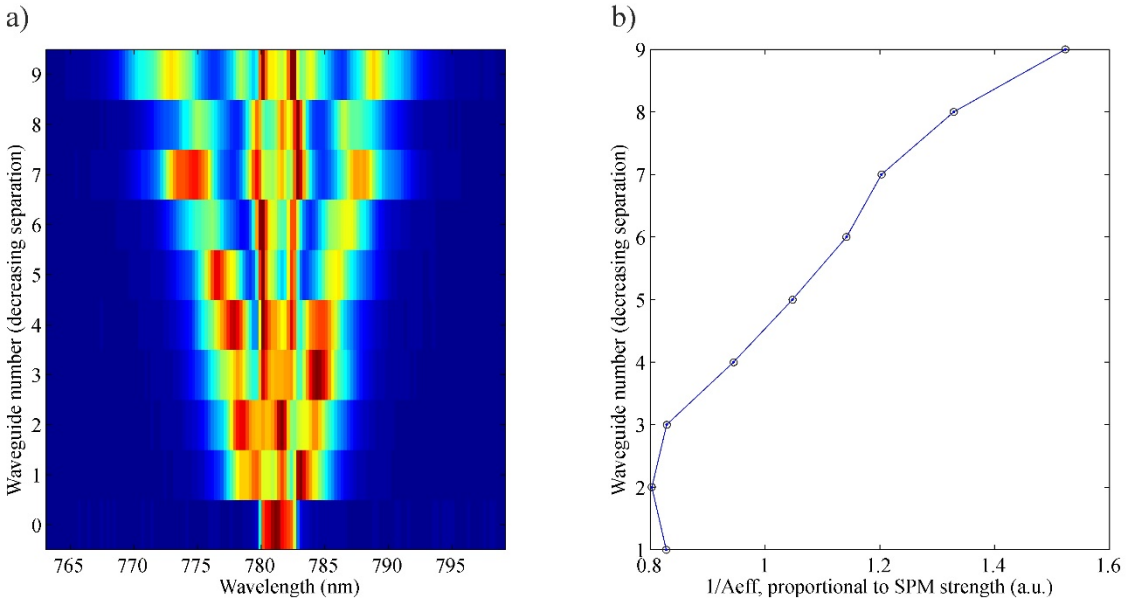

Figure 3.30 Spectrum broadening for all straight waveguides with different separation between two straight waveguides of each pair. Number 0 corresponds to the pump at input (a), measured $1/A_{eff}$ for each straight waveguide. This value is proportional to the growth of the spectrum broadening in waveguides (b).

3.3 Dispersion modulation in photonic crystal fibers (PCF)

Here we consider another approach to study the dynamical Casimir effect analogue in nonlinear optics. In this proposal, the periodic modulation of the group-velocity dispersion (GVD) during the propagation in a photonic crystal fiber is used for the generation of side-bands. This is achieved by a periodic modulation of the fiber core diameter. This dispersion modulation in PCF leads to the generation of photon pairs. In the normal dispersion regime, this phenomenon can be described by four-wave mixing, which satisfies momentum and energy conservation. Considering the phase matching conditions and energy conservation, one can write [74]:

$$k_i + k_s - 2k_p + 2\gamma P_p = 0 \tag{3.1}$$

and

$$\omega_i + \omega_s = 2\omega_p \tag{3.2}$$

where k is the wave vector, ω and P correspond to the frequency and pump power respectively. The i,s,p indexes respectively correspond to the idler, signal and pump and γ is the nonlinear coefficient of the fiber:

$$\gamma = \frac{2\pi n_2}{\lambda_p A_{eff}} \tag{3.3}$$

where λ_p is the pump wavelength and A_{eff} is the effective area of the fiber.

Now we consider the nonlinear Schrodinger equation (NLSE) which explains the modulation instability (MI) process in optical fibers[74]:

$$i\frac{\partial u}{\partial z} - \frac{\beta_2(z)}{2}\frac{\partial^2 u}{\partial t^2} + \gamma |u|^2 u = 0 \tag{3.4}$$

where u is the slowly varying amplitude of the pulse envelope and β_2 is the longitudinal evolution of the GVD along the propagation axis. This GVD can be written as:

$$\beta_2(z) = \overline{\beta}_2 + \beta_2^A \times \sin(2\pi z / Z) \tag{3.5}$$

where Z is the period of modulation, $\overline{\beta}_2$ the average group velocity dispersion and β_2^A corresponds to the amplitude of the GVD modulation. For a uniform fiber $(\beta_2 = const)$, the MI is governed by [74]:

$$\beta_2 \Delta\omega^2 + 2\gamma P = 0 \tag{3.6}$$

From Equation 1.6 one can see that in the normal dispersion regime $(\beta_2 > 0)$ no perfect phase matching can be achieved and consequently MI can not take place. In the anomalous dispersion regime $(\beta_2 < 0)$, on the other hand, we Equation 3.6 has soloution. For the case of dispersion modulated fibers, the periodic modulation of the GVD gives rise to a dispersion grating which must be taken into account [76]:

$$\overline{\beta}_2(z)\Delta\omega^2 + 2\gamma P = 2k\pi / Z \tag{3.7}$$

where k is a positive or negative integer. Equation 3.7 shows that an infinite number of MI side bands can be generated in modulated dispersion fibers. Furthermore, an expansion of up to the fourth order dispersion term is needed to explain why one can observe the MI process in uniform optical fibers that exhibit normal dispersion [77]–[79]. The same approach can also be taken for dispersion modulated fibers. When the average GVD is very low, i.e. when the pump wavelength is close to the average zero dispersion wavelength (ZDW) of the fiber, higher order dispersion terms must be considered and Equation 3.7 should be replaced by [80]:

$$\overline{\beta}_2(z)\Delta\omega^2 + \overline{\beta}_4(z)\Delta\omega^4/12 + 2\gamma P = 2k\pi/Z \tag{3.8}$$

where $\overline{\beta}_4$ is the average fourth order dispersion. Figure 3.31shows the quasi-phase matching curves from Equation 3.8 for a typical dispersion modulated fiber with a ZDW of *1059 nm*.

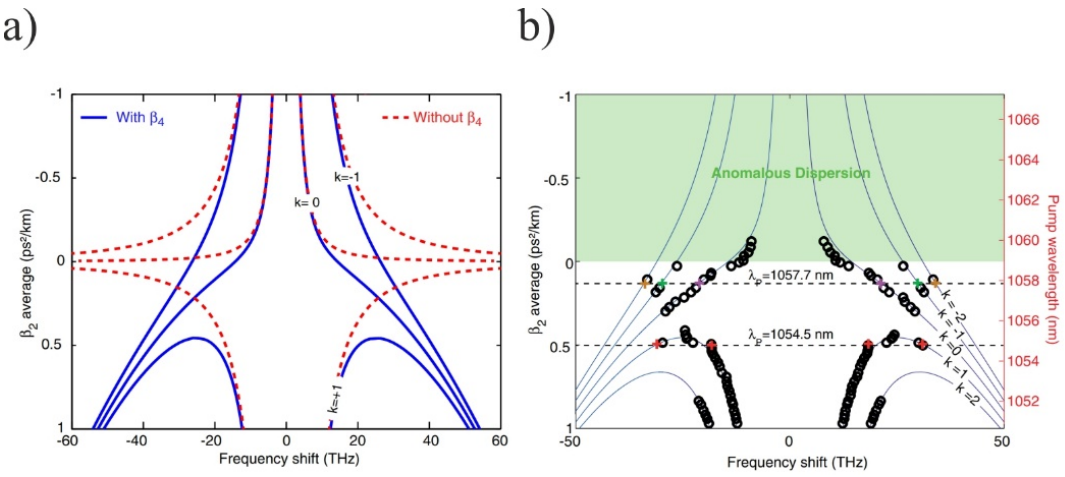

Figure 3.31 Quasi-phase matching curves calculated from Equation 3.8 with and without the β_4 term (blue solid and red dashed lines, respectively) as a function of average GVD (a), Quasi-phase matching curves calculated from Equation 3.8 (solid line) and measured values of side-bands frequencies achieved by tuning the pump wavelength (markers) (b). Figures extracted from Ref. [81]

In order to highlight the role of the dispersion modulation, we can compare Equation 3.8 with the expected behavior in the absence of any modulation i.e. a uniform PCF such as those shown in [78], [79]. Figure 3.32 (a) shows the prediction of the side-bands positions and the corresponding experimental measurements for the uniform PCF pumped with a wavelength below the ZDW (in the normal dispersion regime, $\beta_2 > 0$). The ZDW for the PCF in this experiment is *715 nm*. As one can see in Figure 3.32 (a), it is clear that in the case of no modulation (*k=0*) the signal and idler should diverge for larger amounts of normal dispersion. In contrast to these results for the uniform fiber, our experimental results confirm the opposite trend. This can be explained by looking at the first order of the grating. Figure 3.32 (b) presents the cross-correlation measurement of the side-bands generated from the uniform PCF pumped in the normal dispersion regime.

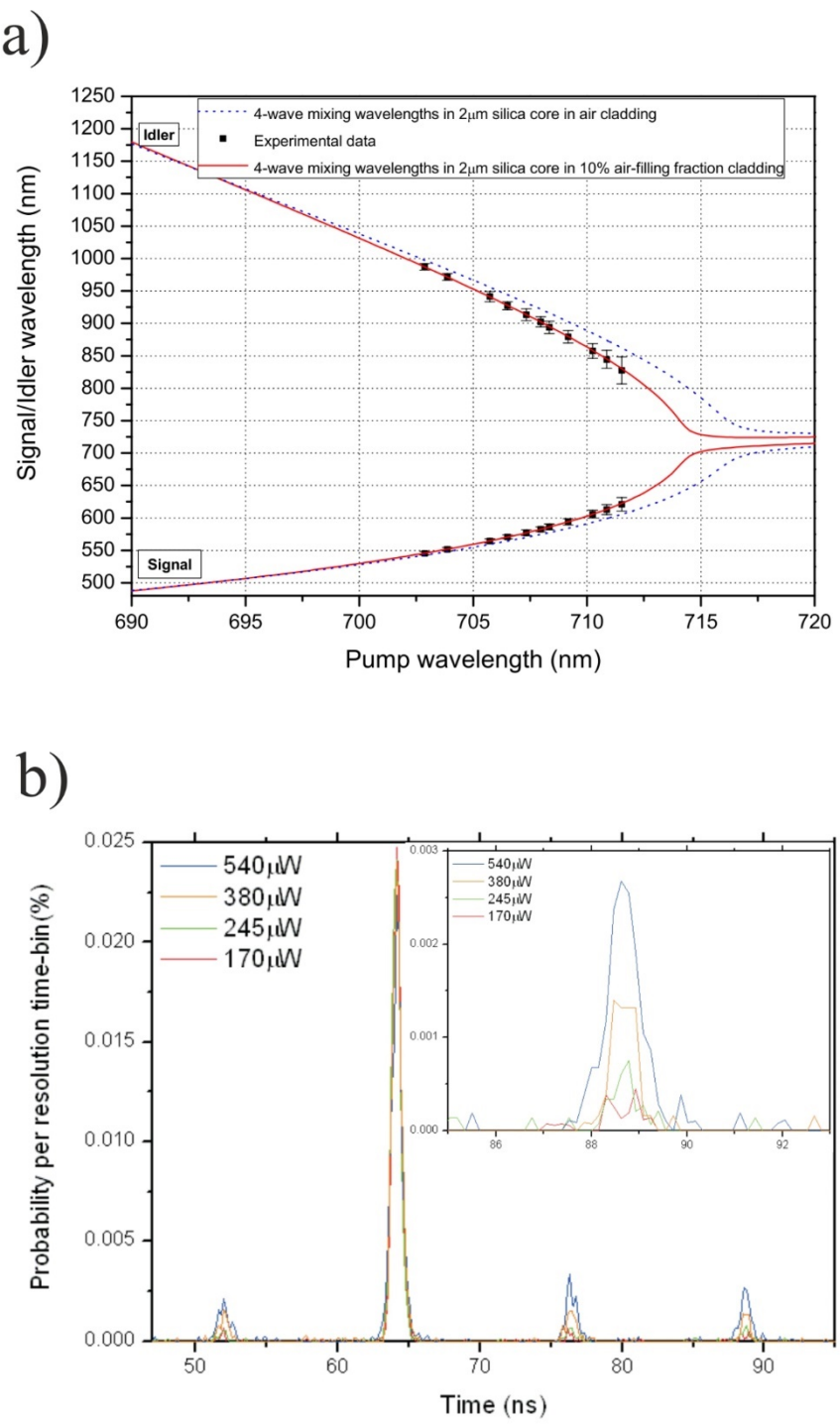

Figure 3.32 Nonlinear phase-matching diagram for the four-wave mixing process. The dashed curve is the simulation using a plain strand of silica suspended in the air, while the solid curve is the fit used to retrieve the actual refractive index of the fibre. The black points correspond to the experimental data while their error bar is proportional to their measured FWHM (a), Time interval histogram showing the correlated photon peak and (inset) an enlarged view of the accidental coincidence peak for different pump powers (b). Figures are taken from [79].

Figure 3.33 predicts the position of the side-bands for a unifrom PCF with a ZDW *(λ_0)* at about *1065 nm* [78]. Here, postion of the side-bands are calculated for different pump powers. As is expected from Equation 3.8, the frequency shift of the side-bands is also a function of the power. However, in the normal dispersion regime, if the pump wavelength is at least *10 nm* below the ZDW, the power dependence of the frequency shifts of the side-bands is not significant.

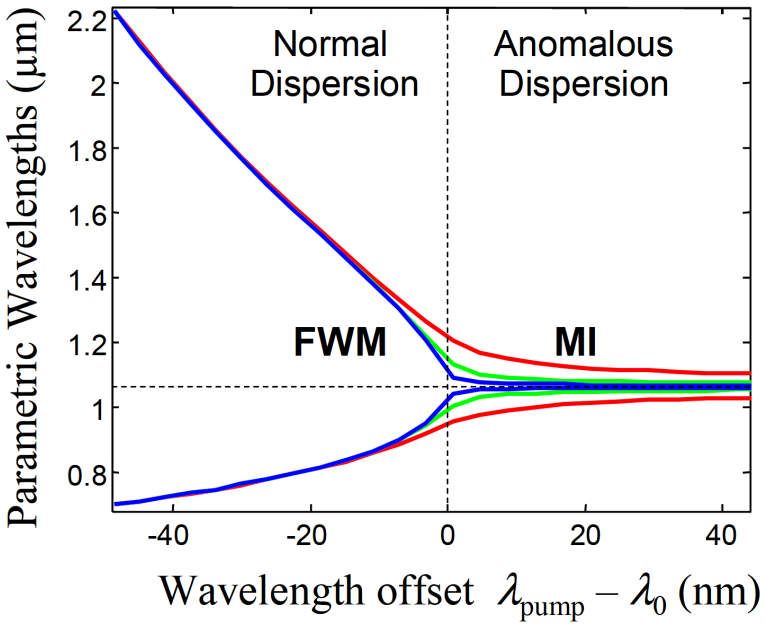

Figure 3.33 Typical solution of the nonlinear phase matching and energy conservation for given pump powers *(P_p=14, 140, 1400 W*, blue, red and green curves). λ_0 corresponds to the ZDW of the fiber. Data from [78].

3.3.1 PCF specifications

The fiber is fabricated by Dr. Arnaud Mussot at the University of Lille in France. The standard stack and draw technique is used for the fabrication of this PCF [82]. Figure 3.34 shows a schematic view of the stack and draw method. In this process, the fiber consists of cappilaries with specific ratio of the inner to outer diameters.. These capillaries are then directed into a triangular lattice by special jigs. The targeted outer diameter for the uniform PCF is controlled by the feeding rate, furnace temperature and tractor speed. However, for the fabrication of the periodically modulated PCF, the fiber diameter is shaped and adjusted by the evolutoin of the drawing speed.

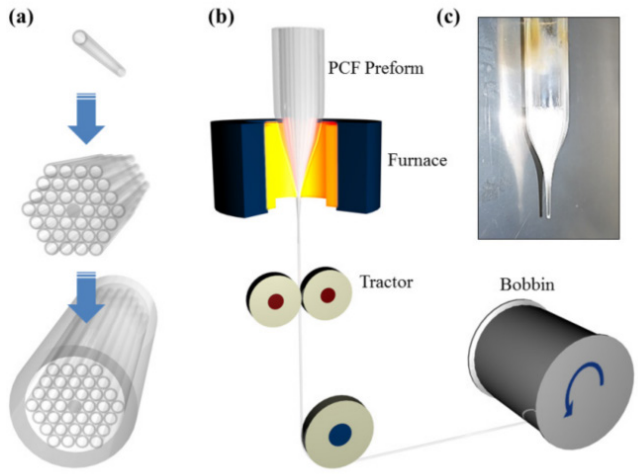

Figure 3.34 Schematic of stack-and draw method. (a) Stacking of photonic crsytal fiber prefrom. (b) Fiber drawing process. (c) photonic crystal fiber preform. Figure from [83].

The fiber is designed with a modulation period of *50 cm* with the ZDW at *1062 nm*. Figure 3.35 (a) presents a typical outer diameter modulation versus the fiber length and a scanning electronic microscope image of the cross-sections ifor the maximum and minimum outer diameters are shown in b & c. Figure 3.35 (d) shows the corresponding sinusoidal dispersion modulation along the fiber's axis.

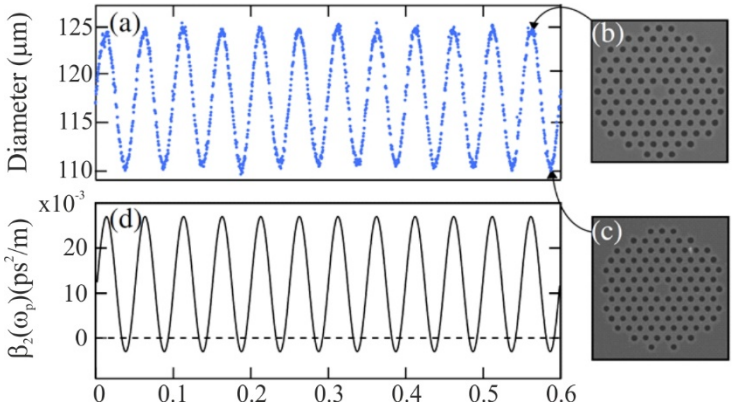

Figure 3.35 Modulation properties of the photonic crystal fiber. Sinusoidal modulation of the outer diameter of the fiber along the propagation (a), scanning electronic microscope (SEM) image of the fiber in its maximum outer diameter section (b), SEM image of the fiber cross-section in its minimum outer diameter (c), corresponding second order dispersion modulation (for the fundamental wavelength at 1062 nm) versus the fiber length (d). Figure is taken from [84].

The positions of the side bands, which were later measured and the results published [84], are defined by the following equation:

$$\Omega_k = \pm\sqrt{\frac{2}{\beta_2}\left(\frac{\pi k}{Z} - \gamma P_p\right)} \tag{3.9}$$

where Ω_k is the frequency detuning from the pump, k is the integer number, Z is the modulation periodicity, β_2 second order and P_p corresponds to the pump power.

Here we present the experimental approach for the quantum correlation measurement of these side-bands to confirm the entangled photon emission. Figure 3.36 presents the schematic view of the setup. In this setup, we use a pulsed laser with a pulse duration of *1.2 ns* and repetition rate of *1 MHz*. We use grating (G1) to spatially spread the spectrum of the collected signal from the photonic crystal fiber. With this arrangement the spectrum of the signal photons can be filtered with a high efficiency using an adjustable slit. The slits on either side allow us to adjust the resolution of the coupling signal to the single photon detectors. The stages are mainly used for the cross-correlation measurement, where we need to find and select the best part of the spectrum to optimise the coincidence-to-accidental ratio (CAR). Later, in the results section, we discuss the procedure for the CAR measurement in details.

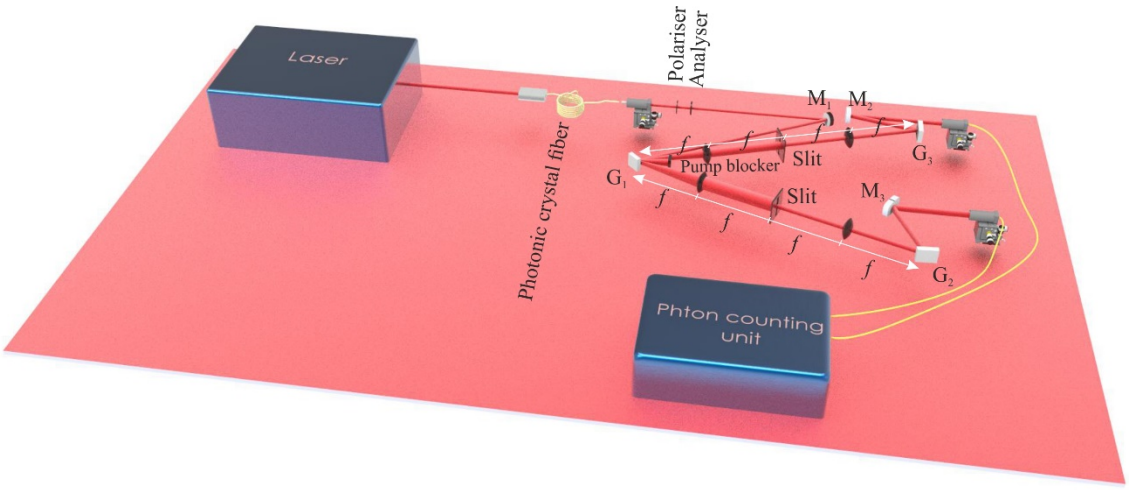

Figure 3.36 Schematic view of the setup for characterisation and cross-correlation measurement.

3.3.2 Experimental results

First we attempt to characterise the spectral filtering system, which consists of grating lenses and a slit. With this system we can decrease the spectral bandwith of the signal down to 0.3 nm. Figure 3.37 shows the experimental results of the spectral filtering

characterisation. In order to perform this measurement, we measure the spectrum for four different sizes of the slit with a relatively high pump power of 60 mW.

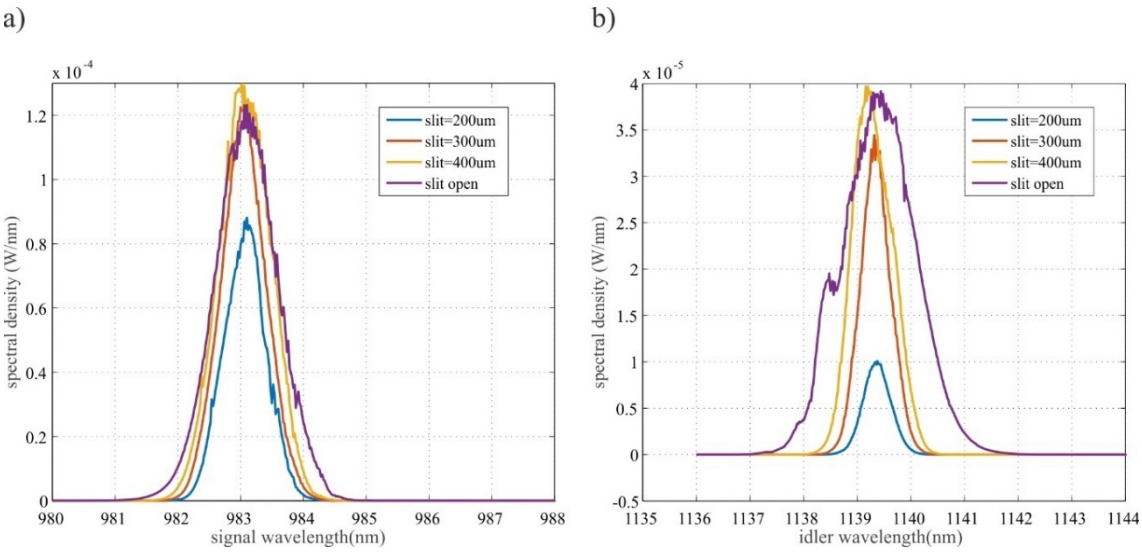

Figure 3.37 Spectral filtering of the signal and idler from the experimental setup in Figure 3.36 for different slit sizes. Signal spectrum for dirrent slit sizes (a), idler spectrum for the same slit sizes (b).

Figure 3.38 presents the measured spectrum at the output of the fiber for a fixed pump power. A shift in the side-bands peaks can clearly be observed by tuning the wavelength. For a fundamental wavelength less than *1054 nm*, the side-band at the right hand side of the pump will be covered by Raman emission, which will affect the cross-correlation measurement and add counts to the accidental peak leading to the drop of the CAR ratio. From this measurement we see that the safe range of the pump wavelength for cross-correlation purposes is about *1054 nm* to *1056 nm*.

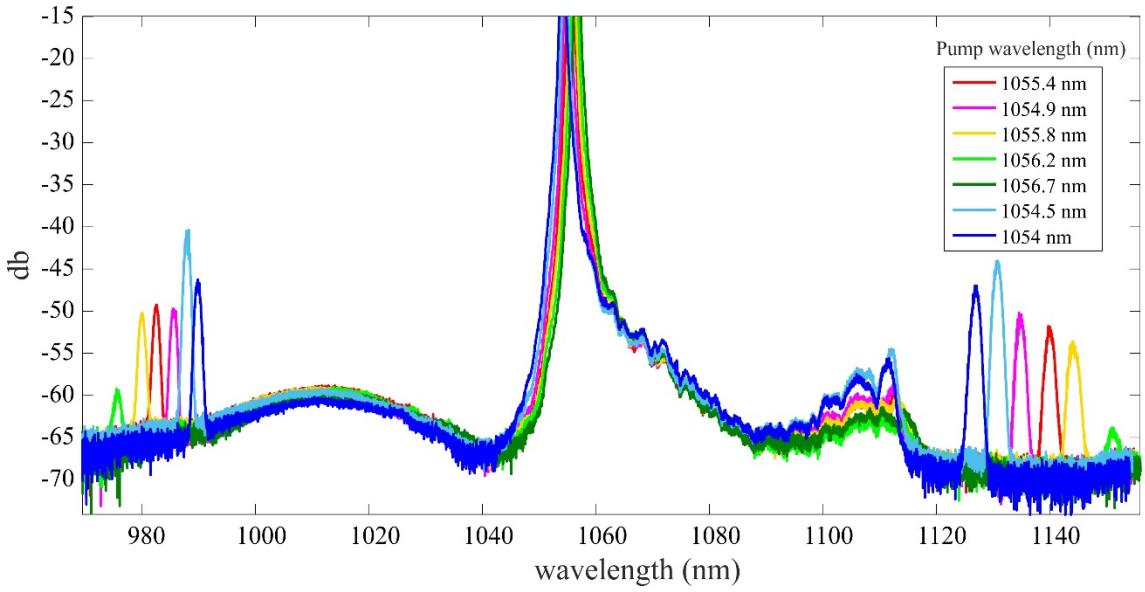

Figure 3.38 Side-bands positions for different pump wavelengths. For this measurement, we keep the pump power fixed for all wavelengths.

ZDW for this fiber is between *1061 nm* to *1062 nm*. The gain drops dramatically by pumping with higher wavelengths close to the ZDW. Figure 3.39 shows the spectrum of the signal and idler side-bands for different pump powers. By changing the pump power one can observe a shift in the signal and idler peak, this can be explained by considering Equation 3.8.

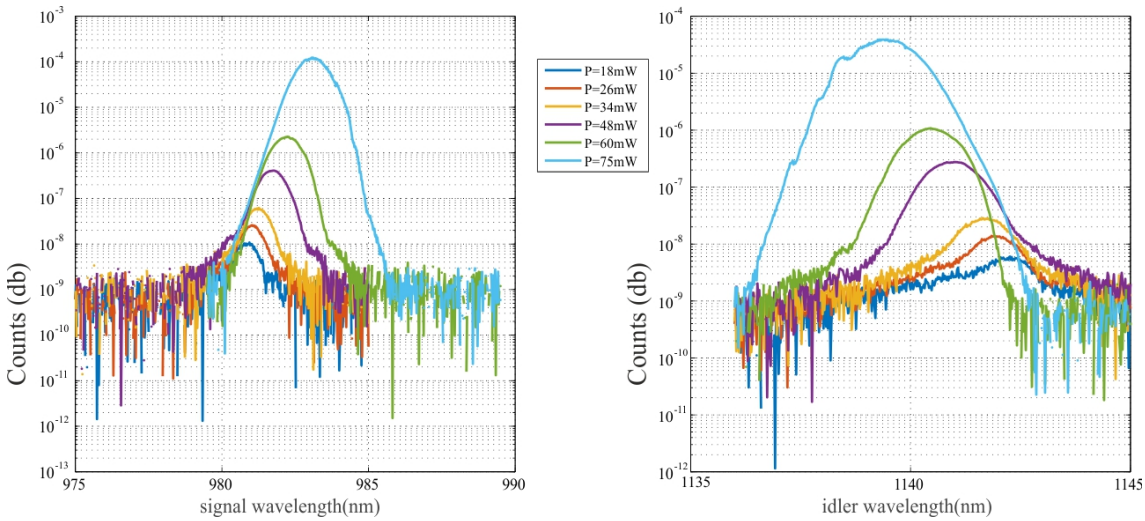

Figure 3.39 Power dependence of the signal and idler peaks for the fixed pump wavelength. The pump wavelength for this measurement is 1055.4 nm.

We characterise the pump power dependence of the signal and idler in the low power regime (see Figure 3.40). This power dependence has a linear fit as expected for low power regime.

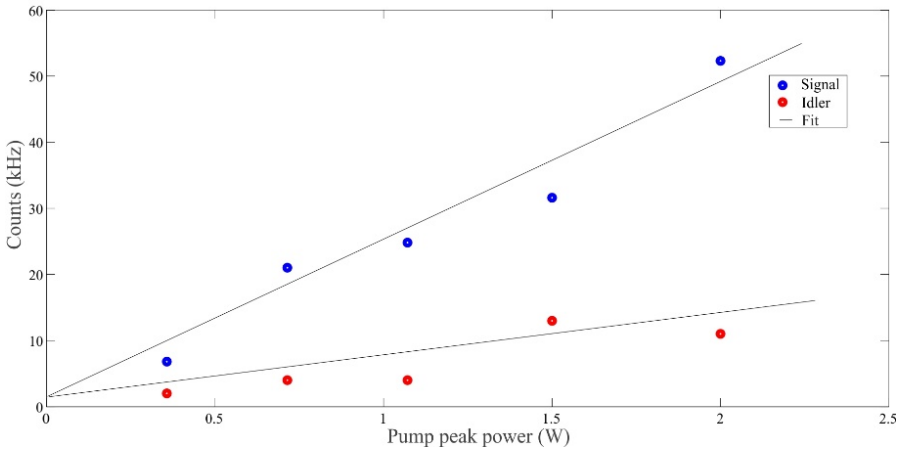

Figure 3.40 Power dependence of the signal and idler counts for the pump wavelength at 1055.4 nm.

As the next step, we perform the quantum cross-correlation measurement. For this purpose we use Excelitas single photon detectors and an IDQuantique ID801 photon counter unit. First we present the cross-correlation measurement between the signal and idler (see Figure 3.41 (a)). In Figure 3.41, we also compare this measurment with the cross-correlation measurment of the Raman peak with the blue shifted side-band (signal peak). We use a technique where we find the maximum of the signal peak and then scan the x axis of the slit position on the idler side to find the the position with the highest CAR. The peak at zero position in the time axis corresponds to the measured number of correlated photons in signal and idler peaks. In this measurement, one detector works as the start and the other one as stop. This means the detector on the first channel (start channel) measures a photon and the electronics measures the amount of time before a click on the second channel (stop channel). If the second photon from the stop channel arrives within a very short amount of time (within the response function of the detector, which is typically a few hundred picosends) this will contribute to the zero delay peak and is considered a correlated photon pair event. Otherwise it is considered to be an uncorrelated ("accidental") event and contributes to one of the accidental peaks.

In order to make the cross-correlation measurement between the signal and Raman emission (Figure 3.41 (b)) we keep the position of the slit on the signal side (blue shifted side-band) fixed and change the position of the slit on the idler side, which collects the photons where we do not expect any correlation and consists mainly of Raman emission. One can see that in Figure 3.41 (b) the zero delay peak is similar to the accidental peaks. This means that there is no quantum correlation between the Raman emission and the

signal photons. The number of the peaks seen in each window depends on the chosen resolution of the photon counting unit (ID801). The time interval between peaks corresponds to the repetation rate of the laser.

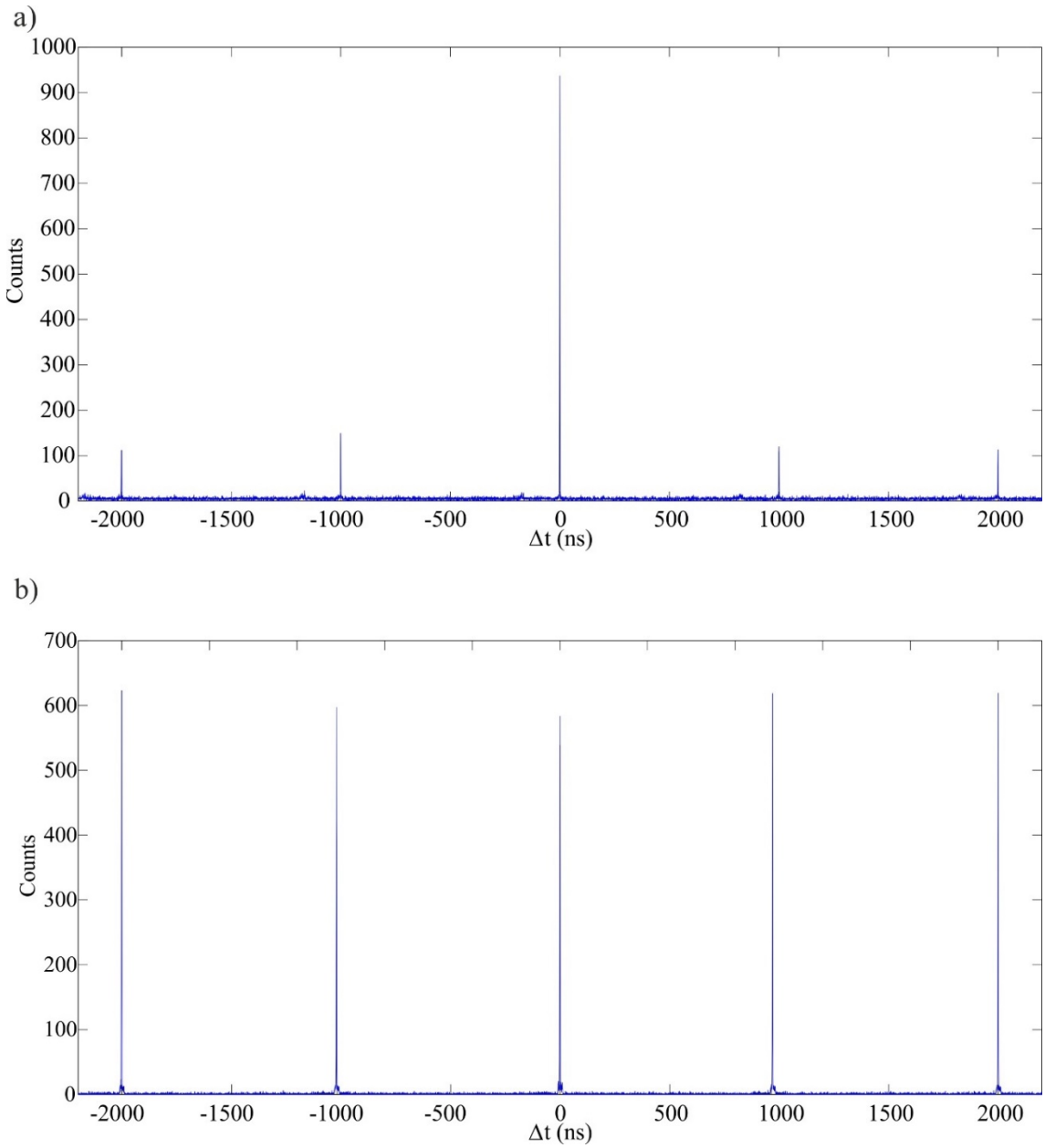

Figure 3.41 Cross-correlation measurement of the signal and idler peaks (a), Cross-correlation measurement of the signal peak with the Raman peak (b).

Additionally, we characterise the power dependence of the CAR for a fixed pump wavelength of *1055.4 nm* (see Figure 3.42). One can see that by decreasing the pump power the CAR increases as expected for quantum correlation measurements. From an experimental point of view, using a low pump power means that we have a smaller number of counts in each channel. This potentially influences the integration time. The

slit positions are reoptimised every time the pump power is changed to ensure the maximum CAR is reached.

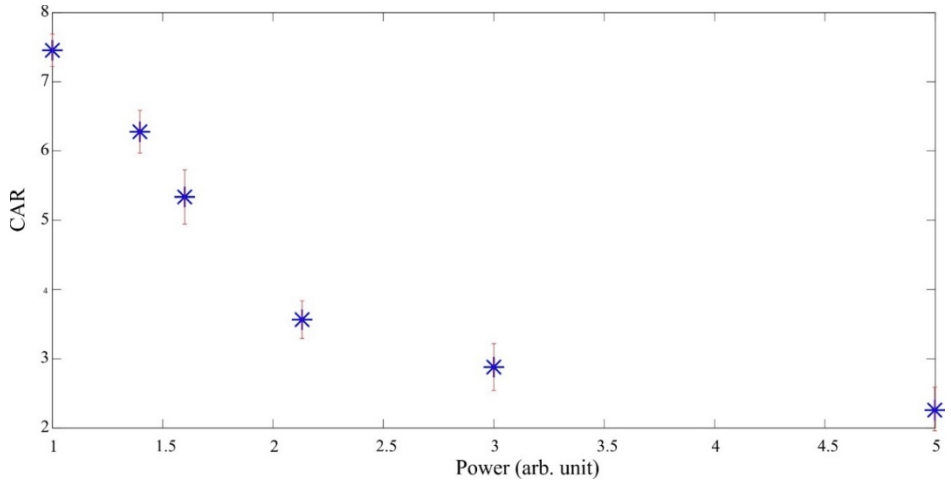

Figure 3.42 Pump power influence on CAR. The pump wavelength is fixed for all measurements and is at 1055.4 nm.

Additionally we study the influence of the slit size on the CAR (see Figure 3.43). We see that by reducing the slit size, we get higher CAR. However, the influence of the slit size is not that significant.

As previously mentioned in this chapter, in order to consider the photon pair generation from the spatially modulated boundary conditions, as a DCE-like emission, the main criterion is to have a pulse shorter than the modulation periodicity. In this case one can consider the modulation of the boundary conditions in the comoving frame of the pulse as the oscillation in time. The pulse duration of our laser (*1.2 ns*) corresponds to a length of about 17.2 cm. This is about 3 times shorter than the modulation periodicity which is 50 cm. By satisfying this criterion, we can claim that the measured correlated photons are due to DCE emission.

As the next step we will prepare the setup to measure a heralded single photon $g^{(2)}(\tau)$. This measurement provides undeniable proof of single photon emission. In this experiment three single photon detectors will be used. For this measurement a beamsplitter will be placed on the signal side. Coincident events will be measured between the two output paths heralded by the arrival of a photon in the idler arm resulting in a threefold coincidence measurement. It shows that the photon arrival statistics are sub-poissonian. Below 0.5 in the zero-delay peak can only be achieved by quantum states [85].

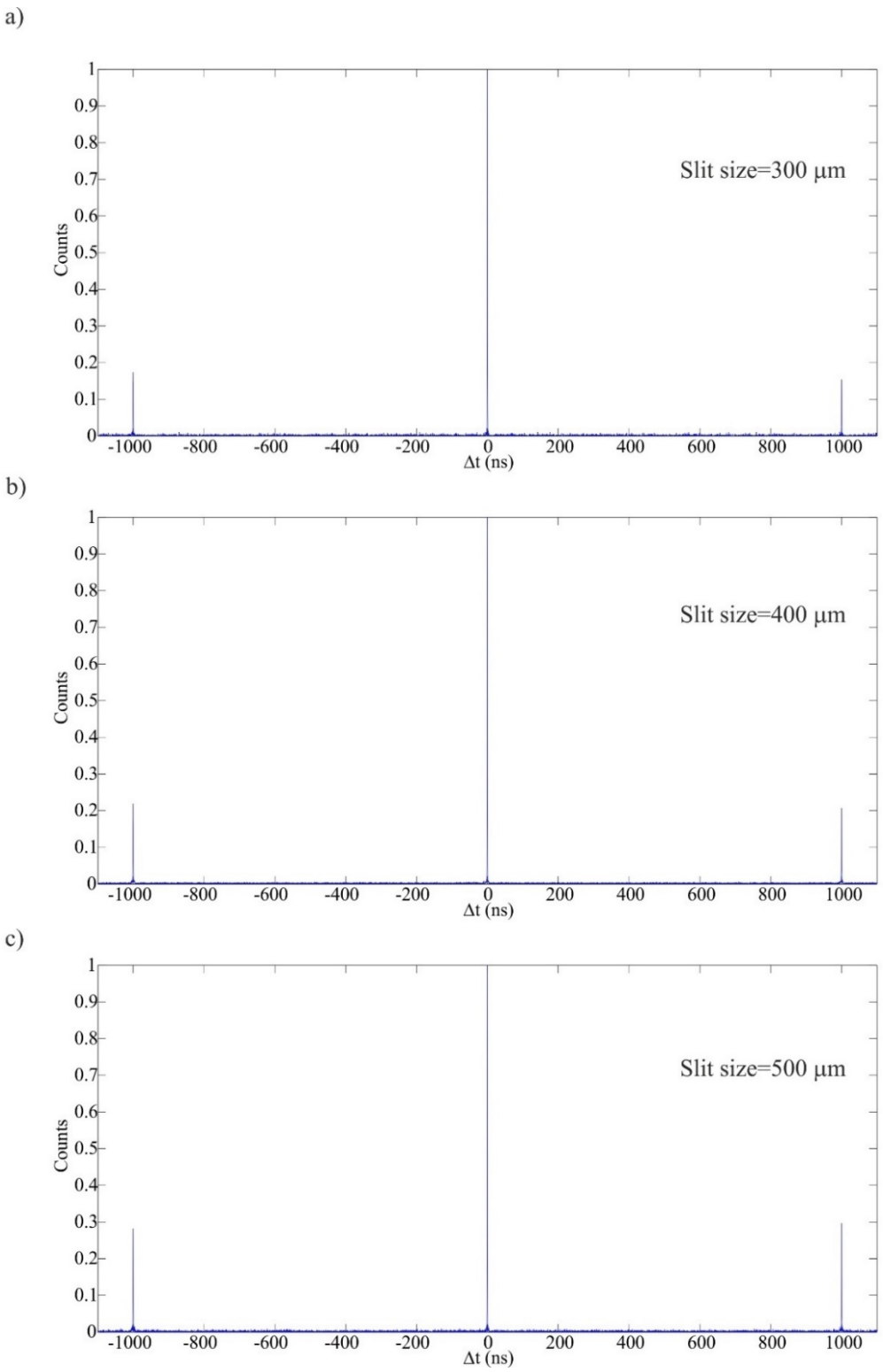

Figure 3.43 Influence of the slit size on the CAR. In this measurement we keep the pump power and the pump wavelength fixed. We stop the measurement, when the zero-delay peak reaches the fixed number of counts. (a),(b) and (c) correspond to slit sizes of 300, 400 and 500 µm respectively.

3.4 Conclusion

We demonstrated how the spatial modulation of the waveguide along the propagation axis is an optical analogue of DCE. Our numerical study confirms the generation of new entangled photon pairs. We show the dependence of the position of the DCE side-bands on the modulation periodicity.

However, in a GLS sample the low coupling efficiency in comparison to the theoretical expectation from one side and the low surface damage threshold from the other, limit us in coupling enough power into the waveguide. We also have the dimensional limitation of the raw material, which means that we cannot increase the modulation periodicity to separate the DCE side-bands or increase the modulation numbers along the propagation in order to amplify the number of generated photons to make them measurable and extract them from the Raman and photoluminescence signal. However, we measure the SPM from the modulated waveguides, but all nonlinear effects are still less than the theoretical expectation.

Using fused silica as the substrate material makes it possible to have a longer propagation length in the nonliner medium. However, we still have extremely low coupling efficiency and very high radiation loss for the modulated waveguides. We consider the lack of third order nonlinearity as the main reason why we measure a SPM about 5 times less than the theoretical calculation in modulated waveguide.

The final approach for the investigation of the correlated photon pairs from the photonic crystal fiber, assisted by the nonlinear dispersion of the fiber appears to provide an analogue of DCE as we modulate the dispersion as a boundary condition in time. This project has been starting in the last months of this PhD research and the project is still ongoing in the research group for the further optimisation of CAR and investigation.

4 Conclusion and future work

This thesis presents the development of a set of novel optical approaches to study the Dynamical Casimir effect (DCE). This work provides a new perspective and insight into one of the most exciting and surprising phenomena in Quantum Physics. All of the approaches considered use manipulation of material properties through the nonlinear optical susceptibility to reproduce the temporal modulation of boundary conditions concomitant with the dynamical Casimir effect. We underline how different optical processes in the nonlinear medium can be considered as the analogy of DCE.

In chapter two, we presented the possibility to use a monolayer of MoS_2 $(\chi^{(2)})$ for the study of the DCE. Preliminary studies focused on characterisation of this material in both the visible and IR regime can, which find broad application and huge potential for novel electronic and optoelectronic applications. We note that these characterisation techniques can be used in a number of atomically thin layers of 2D materials ranging from wide-bandgap insulators and semiconductors to superconductors that can be easily and inexpensively isolated from a piece of bulk layered material [1].

The SHG signal from 2D MoS_2 flakes is estimated to be a few orders of magnitude larger than that of common bulk materials such as $LiNbO_3$ and β-BaB_2O_4 (BBO) (*7* to *9 pm/V*). However theoretical estimations and experimental values for the $\chi^{(2)}$ currently reported in literature are contrasting and vary over *3* orders of magnitude. Some authors [19] estimate a susceptibility of the order of *100 pm/V*, with on-resonance values rising to *4000 pm/V* at *800 nm*. We presented measurements of $\chi^{(2)}$ for mechanically exfoliated MoS_2 monolayer as a function of input wavelength in the range between *710 nm (1.75 eV)* and *1000 nm (1.24 eV)*. We presented high resolution data in which we found a maximum value of $\chi^{(2)} \approx 10^4\ pm/V$, that compares well to the values from [17] which are about *20* times smaller (*400 pm/V* at the maximum). Our values are one order of magnitude less than those reported by [16] and thus overall compatible with the range of values reported in literature.

In this work, we proposed a mathematical model for the pump polarisation dependence and polarisation of the emitted signal of the second harmonic generation (SHG) and

spontaneous parametric down conversion (SDPC) from a MoS_2 monolayer. We also presented different experimental methods of the polarisation measurement of SHG signal, which match the theoretical expectation. The possible SPDC signal measurement from a 2D transitional metal dichalcogenide material was first performed and discussed in this thesis. In the monolayer MoS_2 sample we show a perfect match between the experimentally measured polarisation dependence of the input and output light emission with that predicted by our mathematical model based on SPDC. However, in bulk and edge states of the MoS_2 sample we see a very different dependency on the polarisation, suggesting an alternative mechanism for the light emission.

We also presented the time-resolved measurement of the expected SPDC signal from a MoS_2 monolayer. We observe a long life-time of the SPDC signal, which is expected to be instantaneous and within the resolution of the detector response function. For detection in the visible range of *50 nm* bandwidth centred at *875 nm*, we find agreement with our expectation that SPDC can be strongly dominated by photoluminescence signal. However, the emitted signal from the MoS_2 monolayer flake in IR regime, where we do not expect to have significant photoluminescence signal, shows just one fast exponential decay. This fits the response function of the detector, while the emitted signal from a bulk and edge state is longer than the response function and is represented by two exponential components with different weights from one point to another one on bulk or the edge states, respectively.

These differences between the signal from monolayer and bulk crystal led us to make a conclusion that the nature of these signals are different and they belong to different physical processes. They indicate, that indeed the fast signal from the monolayer could correspond to SPDC, but a stronger emission or more evidence is needed in order to reach a definite conclusion.

Cross-correlation measurements of the emitted signal from MoS_2 in both visible and IR regime show the coincident to accidental ratio (CAR) around *1*. However, our estimation for the number of detectable photons in the visible regime proves that the measurable number of generated entangled photon pairs is much less (about *14* times) than the experimental standard deviation in the cross-correlation measurement. This experimental standard deviation is about *15* times higher than the theoretical standard deviation. The experimental error comes from electronic noise and scales linearly with integration time.

It means that with the current state-of-the-art electronics, it is impossible to measure CAR higher than *1* for this type of SPDC.

However, polarisation dependence and life-time measurement in IR regime are two strong indications for SPDC emission from the MoS_2 monolayer. This is strong motivation for future experimental measurement of the SPDC signal from a MoS_2 monolayer. As mentioned in Appendix I, the number of detectable correlated photon pairs scales with the square of the collection efficiency μ, which is very low in this experimental configuration. Our estimation suggests that a viable strategy to improve the CAR consists in increasing the collection efficiency of the emitted signal.

In chapter three we present two experimental methods for the study of DCE in a different nonlinear medium. In this chapter, we use the third order nonlinear optical susceptibility $(\chi^{(3)})$ of the material.

As we mentioned in chapter one, the main criterion for the DCE is the modulation of the EM mode boundary condition in time. We presented two main approaches to possibly perform study the DCE using spatial modulation of the boundary conditions of the EM mode in the lab frame. In chapter three we demonstrated that a spatial modulation along the propagation length acts as a temporal modulation in the co-moving frame of the pulse.

The first approach considers modulation of the pump field intensity along the length of a waveguide. In this case, we modulate the intensity of the pump by modulation of the refractive index along the waveguide. We use two different materials as substrate for the waveguide. In both cases, we use a Ti-Sapphire *100 Hz* femtosecond laser beam centred at *785 nm* as the pump source.

The first waveguide is made from a gallium lanthanum sulphide (GLS) substrate. However, a number of effects lead to compromised experimental results, such as low coupling efficiency, low surface damage threshold and limited size of the substrate . As a possible route to improve these experimental results, we suggest that a longer waveguide size and more efficient coupling can pave the way to make the DCE effect measurable.

We also used a fused silica substrate for the modulated waveguides. Choosing this material makes it possible to increase the waveguide length up to *10 cm*. However, the

lack of nonlinearity, radiation loss along the waveguide [5] and low coupling efficiency strongly affects nonlinear processes. Our measurements show self-phase modulation in the most efficient waveguide in the fused silica substrate to be about one order of magnitude smaller than the theoretical expectation.

In a second approach, presented in chapter three, we use a periodic modulation of the group velocity dispersion in a photonic crystal fiber to study the generation of two new frequencies resulting from the annihilation of two pump photons. This process can be described by spontaneous four wave mixing. We also show that in dispersion modulated photonic crystal fiber this criterion is satisfied, which means the new generated pairs of photons can be considered as DCE photon pairs. As a proof of this we present cross-correlation measurements of signal and idler photons, which is the sufficient and necessary condition for the presence of quantum correlations. The measurement of the temporal correlations between the signal and idler in presented experiments leads to a coincident to accidental ratio (CAR) of *7.5*. We also present the characterisation of the slit size influence on CAR (see Figure 3.43). Notwithstanding that the slit size not strongly affect the CAR but it shows that the CAR can be opitimsed by adjusting the slit size.

This thesis presents experiments that are currently ongoing within the Extreme Light research group. Presented data are the initial successful measurements and below we list future works and experiments that are planned within this field:

- Using shorter pulses or alternatively using a photonic crystal fiber with longer modulation periodicity in order to efficiently satisfy the DCE emission's condition in spatially modulated medium.
- Increasing the collection efficiency in the experimental setup and more efficient filtering. In the short term, an improvement in the performance of the detection assembly can be obtained by optimizing the choice of the optical components used: the aim is to maximize the reflectivity or transmission of these components (diffraction gratings, mirrors, imaging lens, Microscope objective).
- Presented measurements of the power dependence of CAR in Figure 3.42, clearly shows that there is optimal value of the pump power, which gives the higher value of the CAR. However, this pump dependence can be done with higher resolution. We also assume that the pulse duration of the pump field can affect the CAR.

Hence for the optimisation of the CAR, the pulse duration dependence can be studied to find the optimal value.

- As mentioned in chapter three, the current experimental setup does not allow us to measure the accidental and zero-delayed peak at the same time. We are planning to use other Time-Correlated Single Photon Counting (TCSPC) to measure both peaks simultaneously.
- Measuring the second order correlation function $(g^{(2)})$ of the emission.

5 Appendices

5.1 Appendix I Estimation of the measurable correlated photons from SPDC process

In Figure 2.21 we present the cross-correlation measurement of monolayer MoS_2, while pumping the crystal at *437 nm* and measuring at *875 nm* with a bandwidth of *50 nm*. As one can see, the coincidence-to-accidental ratio (CAR) for this measurement is around 1. We assume that the main reason for the lack of CAR>1 in this case is that only a very small part of the collected signal is due to the SPDC process, as it is dominated by the strong PL signal at this wavelength. In order to confirm this hypothesis, we use Equation (1.31) to estimate the contribution of the SPDC signal to the zero-delay peak in cross-correlation measurements. It can be seen that the signal power in Equation (1.31) scales quadratically with $\chi^{(2)}$. It should be noted that the value of $\chi^{(2)}$ for MoS_2 reported in literature varies by 3 orders of magnitude; for this estimation we use the value of $\chi^{(2)}$ that we measured at *875 nm* ($0.9 \cdot 10^4$ *pm/V*, Figure 2.21). This value is in the middle of the reported range and we estimate that it is accurate within a factor of 3, based on the experimental sources of error.

The parameters for this calculation are:

Variable	unit	variable	unit	variable	unit	variable	unit
$L = 0.68$	*nm*	$P_p = 18$	μW	$d_{eff} = 4.5$	nm / V	$n_p = 3.5$ [86]	–
$\delta\lambda_s = 50$	*nm*	$\lambda_p = 437$	*nm*	$\lambda_s = 875$	*nm*	$\lambda_i = 875$	*nm*

By inserting all these parameters into Equation 1.31, we get:

$$\delta P_s = (2\pi)^4 \frac{2\hbar c d_{eff}^2 L \lambda_p}{\varepsilon_0 n_p \lambda_s^5 \lambda_i^2} P_p \delta\lambda_s = 3.17 \cdot 10^{-14}\, W \qquad \text{(App.1)}$$

We then divide the signal power by the photon energy in order to find the rate of expected SPDC photon pairs emitted from the crystal:

$$N_{generated} = \frac{\delta P_s \lambda_s}{hc} = 1.4 \cdot 10^5 \ \frac{1}{s} \qquad \text{(App.2)}$$

where h is the Planck constant and c is the speed of the light. For simplicity, we use the central wavelength of the measured spectrum, which is *875 nm*. The error arising from this estimation is less than *0.05%*, which, in comparison to other assumptions made in this calculation, is not significant.

The next step in this calculation is the estimation of the collection efficiency, μ. This parameter make a quadratic contribution to the estimation of the SPDC role in the zero-delay peak, and so plays a critical part [87]. The lack of phase-matching conditions in the SPDC process for subwavelength films means that the emission is expected to be isotropic on a full solid angle of 4π, along every possible direction. Figure App.1 shows schematic view of all possible directions for the SPDC entangled photon pairs generation.

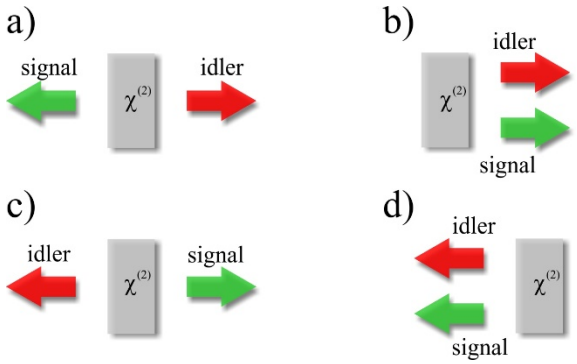

Figure App.1 All possible combinations of the spontaneous parametric down conversion entangled photon pairs generation from monolayer MoS_2 crystal.

Since we collect only from one side of the sample, and we separate signal and idler photons non-deterministically with a *50/50* beam splitter, a factor of *1/4* is contributed to μ, and the collection efficiency of the objective can be estimated from *NA=0.85*. We then consider the collection efficiency of the transmission line, where we take into account the transmission efficiency of all optical elements, the coupling efficiency into the fibres, and the quantum efficiency of the detectors. Taking into account all these parameters gives us a final efficiency of $\mu = 1.4 \cdot 10^{-3}$. By multiplying the rate of generated photons by μ^2 we find the number of detected photons as coincident photons in the cross-correlation measurement (Figure 2.21 (b)):

$$N_{generated}\mu^2 = 0.268 \qquad \text{(App.3)}$$

We then multiply this number by the integration time (*2 hours*) of the measurement in order to find the contribution of the real detected coincident photon pairs in zero-delay peak:

$$N_{generated}\mu^2\Delta t = 1929 \qquad \text{(App.4)}$$

Theoretical calculation of the standard deviation for the peak height in the measurement gives an approximate value of *1800*, while the experimental standard deviation is *~27000*. This experimental standard deviation is calculated by integrating each peak in Figure 2.22 (a), rather than from the peak height, as this integration corresponds to the photon numbers in each peak. This calculation shows that our experimental standard deviation is about *14* times higher than our estimated coincident photon numbers for the whole measurement. This is mainly due to the fact that the few detected photons from the SPDC signal are strongly dominated by the PL signal. Furthermore, as we mentioned, this calculation is based on the assumption that the system is ideal and takes into account just the systematic losses, which means the real detected photons due to the SPDC signal at zero-delay peak are probably even less than our calculated value. All these facts lead to the conclusion that with the currently available electronics and measurement techniques it is impossible to see the CAR>1. We can consider different approaches in order to have the CAR>1, but the simplest solution will be increasing the efficiency of detection.

5.2 Appendix II Theoretical calculation of the polarisation dependence of the SHG and SPDC from MoS_2 monolayer.

Theorethical calculation of the polarisation properties of the SPDC from MoS_2 monolayer has never been studied before. This Calculation developed in our research group and is presented in this thesis first.

Figure App.2 (a) presents a schematic view of the experimental setup for polarisation measurements. In this setup, we control the pump polarisation with a half-wave plate (HWP) and select the output polarisation using a linear polariser (Pol).

Assuming the MoS_2 monolayer is lying in the *x*-*y* plane, and that the incident pump beam is traveling along the *z* axis, we define 2 systems of reference for the polarisation measurements. As illustrated in Figure App.2 (b), θ is the angle of the pump polarisation given by the electric field $\overrightarrow{E_p}$ with respect to the mirror plane *y*, and α is the angle of the polariser with respect to the same axis.

In both SPDC and SHG the generated field is proportional to the nonlinear polarisation:

$$P_i(\omega_1+\omega_2)=\varepsilon_0\sum_{ijk}\chi^{(2)}_{ijk}(\omega_1+\omega_2)E_j(\omega_1)E_k(\omega_2)\ , \qquad \text{(App.5)}$$

where *i*, *j* and *k* are indexing the directions with respect to the crystal axes. The MoS_2 monolayer is a D_{3h} crystal [56], thus we have [28]:

$$\chi^{(2)}_{yyy}=-\chi^{(2)}_{yxx}=-\chi^{(2)}_{xxy}=-\chi^{(2)}_{xyx}\equiv\chi\ , \qquad \text{(App.6)}$$

and all the other terms of the nonlinear susceptibility vanish.

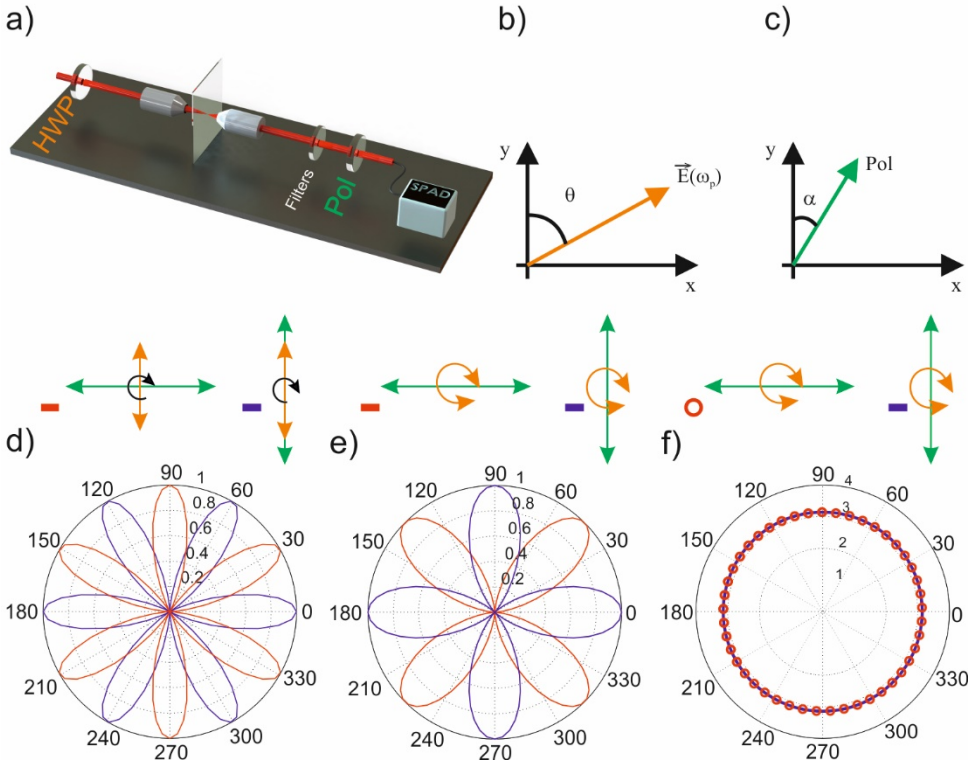

Figure App.2 (a) Experimental setup for the polarisation dependent characterisation. (b) Orientation of the pump polarisation with respect to the mirror plane. (c) Orientation of the linear polariser with respect to the mirror plane. (d) Six-folded pattern for the SHG polarisation dependence when we have the polariser angle perpendicular to the pump polarisation and rotate them together (red line), and when the polariser angle is parallel to the pump polarisation and we rotate them together (blue line). (e) Four-folded pattern for the SHG polarisation dependence when we keep the polariser angle horizontal and rotate the pump polarisation (red line), and when we fix the vertical polariser axis and rotate the pump polarisation (blue line). (f) Polarisation dependence of SPDC when we keep the polariser axis fixed at any random angle α_0 (here α_0=0 – blue line, and $\pi/2$ – red circles) and rotate the pump polarisation. The graphs above panels (d)-(f) represent the legend: the orange and green arrows represent the pump polarisation and polariser angle, respectively. The circular arrow indicates the angle of rotation, and the black circular arrow indicates that both the pump and polariser angles are rotated simultaneously.

In SHG a pump beam at ω_p generates a signal at:

$$P_i(2\omega_p) = \varepsilon_0 \sum_{ijk} \chi^{(2)}_{ijk}(2\omega_p) E_j(\omega_p) E_k(\omega_p) \qquad \text{(App.7)}$$

Now, by considering a pump field in the *x-y* plane at an angel θ with respect to the mirror plane (θ is the angel between the mirror plane and the polarisation of the pump beam) as in Figure App.2 (c), one can write:

$$\begin{cases} E_x = E_p.\sin(\theta) \\ E_y = E_p.\cos(\theta) \end{cases} . \qquad \text{(App.8)}$$

For the $\hat{x}$ and $\hat{y}$ polarisations (no tensor terms give the polarisation along $\hat{z}$), we thus have:

$$\begin{aligned} P_x(2\omega) &= \varepsilon_0 \chi^{(2)}_{xxy} E_{px}(\omega) E_{py}(\omega) + \varepsilon_0 \chi^{(2)}_{xyx} E_{py}(\omega) E_{px}(\omega) = \\ &= \varepsilon_0 \chi^{(2)} 2 E_{px}(\omega) E_{py}(\omega) = \varepsilon_0 \chi^{(2)} E_p^2 2\sin(\theta)\cos(\theta) = \\ &= -\varepsilon_0 \chi^{(2)} E_p^2 \sin(2\theta) \end{aligned}$$

$$\begin{aligned} P_y(2\omega) &= \varepsilon_0 \chi^{(2)}_{yyy} E_{py}(\omega) E_{py}(\omega) + \varepsilon_0 \chi^{(2)}_{yxx} E_{px}(\omega) E_{px}(\omega) = \\ &= \varepsilon_0 \chi [E^2_{py}(\omega) - E^2_{px}(\omega)] = \\ &= \varepsilon_0 \chi [E_p^2 \cos^2(\theta) - E_p^2 \sin^2(\theta)] = \\ &= \varepsilon_0 \chi E_p^2 \cos(2\theta) \end{aligned} \qquad \text{(App.9)}$$

So the intensity of second harmonic along $\hat{x}$ and $\hat{y}$ is proportional to:

$$\begin{aligned} I_x(2\omega) &\propto \sin^2(2\theta) \\ I_y(2\omega) &\propto \cos^2(2\theta) \end{aligned} . \qquad \text{(App.10)}$$

We can write the polarisation *P* along the polariser axis in terms of α:

$$P_\alpha = P_y \cos(\alpha) + P_x \sin(\alpha) \ . \qquad \text{(App.11)}$$

In most of literature the authors fix both the pump and the polariser angles, θ and α, and rotate the sample. This is equivalent to fixing the sample and rotating both the pump and the analyser together, which in our notation corresponds to setting $\alpha = \theta$ (parallel, $P_{\parallel}$) or $\alpha = \theta + \pi/2$ (perpendicular, $P_{\perp}$) in Equation (App.12):

$$\begin{aligned} P_{\parallel}(2\omega) &= \varepsilon_0 \chi E_p^2 \cos(2\theta)\cos(\theta) - \varepsilon_0 \chi E_p^2 \sin(2\theta)\sin(\theta) = \\ &= \varepsilon_0 \chi E_p^2 ((\cos^2(\theta) - \sin^2(\theta))\cos(\theta) - 2\sin(\theta)\cos(\theta)\sin(\theta)) = \\ &= \varepsilon_0 \chi E_p^2 (\cos^3(\theta) - \sin^2(\theta)\cos(\theta) - 2\sin^2(\theta)\cos(\theta)) = \\ &= \varepsilon_0 \chi E_p^2 (\cos^3(\theta) - 3\sin^2(\theta)\cos(\theta)) = -\varepsilon_0 \chi E_p^2 \cos(3\theta) \end{aligned} \qquad \text{(App.12)}$$

Similarly, we can write for the perpendicular component:

$$\begin{aligned} P_{\perp}(2\omega) &= \varepsilon_0 \chi E_p^2 \cos(2\theta)\sin(\theta) + \varepsilon_0 \chi E_p^2 \sin(2\theta)\cos(\theta) = \\ &= \varepsilon_0 \chi E_p^2 ((\cos^2(\theta) - \sin^2(\theta))\sin(\theta) + 2\sin(\theta)\cos^2(\theta)) = \\ &= \varepsilon_0 \chi E_p^2 (\cos(\theta)\sin(\theta) - \sin^3(\theta) + 2\sin(\theta)\cos^2(\theta)) = \\ &= \varepsilon_0 \chi E_p^2 (3\cos^2(\theta)\sin(\theta) - \sin^3(\theta)) = -\varepsilon_0 \chi E_p^2 \sin(3\theta) \end{aligned} \quad \text{(App.13)}$$

The SHG intensity is proportional to the modulus square of *P:*

$$\begin{aligned} I_{\parallel}(2\omega) &\propto \cos^2(3\theta) \\ I_{\perp}(2\omega) &\propto \sin^2(3\theta) \end{aligned} \quad \text{(App.14)}$$

This case gives the standard and well-known six-folded pattern and is represented in Figure App.2 (d).

An alternative way to perform the same measurement is what we presented in the main text, i.e. keeping the polariser fixed at some angle α_0 and rotating the pump polarisation angle θ. In this case the intensity of the emitted signal along α_0 is:

$$I_{\alpha_0}(2\omega) \propto (\cos(2\theta)\cos(\alpha_0) - \sin(2\theta)\sin(\alpha_0))^2 \quad \text{(App.15)}$$

In Figure App.2) (e) we plot the case for $\alpha_0 = 0, \pi/2$ and always find a 4-fold pattern. This is indeed what we observed in the SHG experiment.

For calculating the polarisation dependence of the SPDC, we start by considering a seed at ω_s and calculate the nonlinear polarisation along direction *i*, at the idler frequency (ω_i), from Equation (App.5):

$$P_i(\omega_i = \omega_p - \omega_s) = \varepsilon_0 \sum_{jk} \chi^{(2)}_{ijk}(\omega_p - \omega_s) E_j(\omega_p) E_k(-\omega_s) \ , \quad \text{(App.16)}$$

where ω_p, ω_s and $\omega_i = \omega_p - \omega_s$ are the pump, signal, and idler frequencies, respectively. Since for SPDC, $\overrightarrow{E_s}$ is only given by vacuum fluctuations, we have to average the result on all possible directions of the polarisation vector, $\overrightarrow{E_s}$.

Now, by considering Equation (App.6) and Equation (App.16) for the *x* and *y* components of the SPDC polarisation, one can write:

$$P_y(\omega_p-\omega_s)=\varepsilon_0\{\chi_{yyy}(\omega_p-\omega_s)E_y(\omega_p)E_y^*(\omega_s)+ \\ +\chi_{yyy}(\omega_p-\omega_s)E_y(\omega_p)E_y^*(\omega_s)+ \\ +\chi_{yxx}(\omega_p-\omega_s)E_x(\omega_p)E_x^*(\omega_s)+\chi_{yxx}(\omega_p-\omega_s)E_x(\omega_p)E_x^*(\omega_s)\} \quad . \quad \text{(App.17)}$$

So for P_y we have:

$$P_y(\omega_p-\omega_s)=\varepsilon_0\chi\{2E_y(\omega_p)E_y^*(\omega_s)-2E_x(\omega_p)E_x^*(\omega_s)\} \quad . \quad \text{(App.18)}$$

Similarly, for P_x one can write:

$$P_x(\omega_p-\omega_s)=\varepsilon_0\{\chi_{xxy}E_x(\omega_p)E_x^*(\omega_s)+\chi_{xxy}E_y(\omega_p)E_x^*(\omega_s)+ \\ +\chi_{xyx}E_y(\omega_p)E_y^*(\omega_s)+\chi_{xyy}E_x(\omega_p)E_y^*(\omega_s)\}= \\ =\varepsilon_0\chi\{2E_y(\omega_p)E_y^*(\omega_s)+2E_y(\omega_p)E_x^*(\omega_s)\} \quad . \quad \text{(App.19)}$$

Now, by applying Equation (App.8) to Equation (App.18) and Equation (App.19), one can write:

$$\begin{aligned} P_y(\omega_p-\omega_s)&=\varepsilon_0\chi E_p\{2\cos(\theta)E_y^*(\omega_s)-2\sin(\theta)E_x^*(\omega_s)\} \\ P_x(\omega_p-\omega_s)&=-\varepsilon_0\chi E_p\{2\sin(\theta)E_y^*(\omega_s)+2\cos(\theta)E_x^*(\omega_s)\} \end{aligned} \quad . \quad \text{(App.20)}$$

Assuming that $\overrightarrow{E_s}$ is at a certain angle, θ_s, with respect to y, Equation (App.20) becomes:

$$P_y(\omega_p-\omega_s)=\varepsilon_0\chi E_p\{2\cos(\theta)E_s^*\cos(\theta_s)-2\sin(\theta)E_s^*\sin(\theta_s)\}= \\ =2\varepsilon_0\chi E_pE_s^*\{\cos(\theta)\cos(\theta_s)-\sin(\theta)\sin(\theta_s)\} \\ P_x(\omega_p-\omega_s)=-\varepsilon_0\chi E_p\{2\sin(\theta)E_s^*\cos(\theta_s)-2\cos(\theta)E_s^*\sin(\theta_s)\}= \\ =-2\varepsilon_0\chi E_pE_s^*\{\sin(\theta)\cos(\theta_s)-\cos(\theta)\sin(\theta_s)\} \quad . \quad \text{(App.21)}$$

Polarisation of the idler is proportional to:

$$\begin{aligned} P_y(\omega_p-\omega_s)&\propto\{\cos(\theta)\cos(\theta_s)-\sin(\theta)\sin(\theta_s)\} \\ P_x(\omega_p-\omega_s)&\propto\{\sin(\theta)\cos(\theta_s)-\cos(\theta)\sin(\theta_s)\} \end{aligned} \quad . \quad \text{(App.22)}$$

Now, if we consider a polariser at a fixed angel α_0 we have:

$$P_{\alpha_0}^{\parallel}(\omega_p-\omega_s)=P_x(\omega_p-\omega_s)\sin(\alpha_0)+P_y(\omega_p-\omega_s)\cos(\alpha_0) \quad . \quad \text{(App.23)}$$

Instead the components parallel and perpendicular to the pump are:

$$\begin{aligned} P_{\parallel p}(\omega_p-\omega_s) &= P_x(\omega_p-\omega_s)\sin(\theta)+P_y(\omega_p-\omega_s)\cos(\theta) \\ P_{\perp p}(\omega_p-\omega_s) &= P_y(\omega_p-\omega_s)\sin(\theta)-P_x(\omega_p-\omega_s)\cos(\theta) \end{aligned} . \quad \text{(App.24)}$$

Similarly, one can evaluate the components parallel and perpendicular to the seed:

$$\begin{aligned} P_{\parallel s}(\omega_p-\omega_s) &= P_x(\omega_p-\omega_s)\sin(\theta_s)+P_y(\omega_p-\omega_s)\cos(\theta_s) \\ P_{\perp s}(\omega_p-\omega_s) &= P_y(\omega_p-\omega_s)\sin(\theta_s)-P_x(\omega_p-\omega_s)\cos(\theta_s) \end{aligned} . \quad \text{(App.25)}$$

For each case we have to compile the intensity that is proportional to the square of the polarisation, e.g.:

$$\begin{aligned} I^{\parallel}_{\alpha_0}(\omega_p-\omega_s) \propto [&\sin(\alpha_0)(\sin(\theta)\cos(\theta_s)+\cos(\theta)\sin(\theta_s))+ \\ &+\cos(\alpha_0)(\cos(\theta)\cos(\theta_s)-\sin(\theta)\sin(\theta_s))]^2 \end{aligned}$$

$$\begin{aligned} I^{\parallel}_{p}(\omega_p-\omega_s) \propto [&\sin(\theta)(\sin(\theta)\cos(\theta_s)+\cos(\theta)\sin(\theta_s))+ \\ &+\cos(\theta)(\cos(\theta)\cos(\theta_s)-\sin(\theta)\sin(\theta_s))]^2 \end{aligned} . \quad \text{(App.26)}$$

$$\begin{aligned} I^{\parallel}_{s}(\omega_p-\omega_s) \propto [&\sin(\theta_s)(\sin(\theta)\cos(\theta_s)+\cos(\theta)\sin(\theta_s))+ \\ &+\cos(\theta_s)(\cos(\theta)\cos(\theta_s)-\sin(\theta)\sin(\theta_s))]^2 \end{aligned}$$

In the spontaneous amplification case, we have to consider a seed given by the vacuum fluctuations at all values of θ_s, so that:

$$\begin{aligned} I^{SPDC}_{\parallel\alpha_0}(\omega_p-\omega_s) \propto \int_0^{2\pi} d\theta_s [&\sin(\alpha_0)(\sin(\theta)\cos(\theta_s)+\cos(\theta)\sin(\theta_s))+ \\ &+\cos(\alpha_0)(\cos(\theta)\cos(\theta_s)-\sin(\theta)\sin(\theta_s))]^2 = \pi \end{aligned} ,$$

(App.27)

and similarly:

$$\begin{aligned} I^{SPDC}_{x}(\omega_2) &\propto \int d\theta_s [\sin(\theta)\cos(\theta_s)+\cos(\theta)\sin(\theta_s)]^2 = \pi \\ I^{SPDC}_{y}(\omega_2) &\propto \int d\theta_s [\cos(\theta)\cos(\theta_s)-\sin(\theta)\sin(\theta_s)]^2 = \pi \\ I^{SPDC}_{\parallel p}(\omega_2) &\propto \int d\theta_s [\sin(\theta)(\sin(\theta)\cos(\theta_s)+\cos(\theta)\sin(\theta_s))+ \\ &\quad +\cos(\theta)(\cos(\theta)\cos(\theta_s)-\sin(\theta)\sin(\theta_s))]^2 = \pi \end{aligned} . \quad \text{(App.28)}$$

Therefore, as illustrated in Figure App.2 (f) for any choice of the polariser angle α_0, no dependence of the SPDC signal on the pump polarisation angle is expected, as indeed observed in our measurements (Figure 2.31).

5.3 Appendix III Setup alignment procedure for cross-correlation measurement

The experimental alignment is very important, especially for the investigation of the signal from a monolayer crystal in IR regime. As we mentioned in section 2.6.2, a large percentage of the signal is due to the substrate. In order solve this problem we used different kinds of substrates. Here, we want to mention important aspects of the setup alignment. As one can see we just use the collimation objective to collect the signal from the monolayer in the transmission configuration. The first step to align the setup is to couple the laser directly to the multimode optical fibre without any additional optical elements, such as objectives. This spatial fibre coupler will be used to couple the collected signal from collimating objective; in this stage the aim is to minimise the final adjustment to this coupler. Using this procedure helps us to be sure that after putting g objectives in the system, we still couple the light to the detectors under the same angle. The second step is to put in objectives and try to obtain the same coupling efficiency, without touching the spatial coupler. The final step, which is very important, is finding the right distance of the coupling objective from the sample. For this configuration our flake is on the right hand side facet of the substrate. As we work with monolayer flakes with thickness of about *0.7 nm*, we will rely only on maximising the collected signal to adjust the distance of the objective from the flake. The main difficulty of this process is the photoluminescence from the substrate at this wavelength. So, maximising the collected signal on the single photon detector does not necessarily mean that we couple the image of the flake into the fibre, and it can simply be the image and signal from the substrate. In order to bypass this issue, we first maximise the signal from the flake and take a note of the number of counts "N_f". We then change the position of the substrate and look for a place where there is no flake and we have just the signal from the substrate "N_s". We slightly decrease the signal from the substrate by increasing the focal distance, and then go back to the place where we have the monolayer and take a note of the number of counts "N_f". Finally, the best position for the focal distance of the collecting objective is the distance where the ration of "N_f / N_s" is highest.

For the transmission-reflection configuration, this issue still very important as we use an objective for focusing, which has a longer working distance, and there is a layer of substrate between focusing objective and flake.

5.4 Appendix IV Substrate choice

Choosing the right substrate plays an important role in the coincidence-to-accidental ratio. The photoluminescence emitted from the substrate mainly goes to the accidental peaks, while the signal from the crystal mainly makes a contribution to the zero-delay peaks. Hence it is very important to reduce the photoluminescence signal from the substrate as much as we can. One way to attempt this is to find the best fused silica substrate, which theoretically does not emit photoluminescence in IR regime. We tried different substrates from different companies, but consistently measure a significant photoluminescence from the substrate in comparison to the signal from the monolayer. Our aim is to reduce the photoluminescence signal from the substrate by optimising the collection from the flake. This is relatively easy to achieve for the transmission configuration, but we still have difficulty with the transmission-reflection configuration as the thickness of the substrate plays an important role in the reflection side. We use substrates with thicknesses of *150 μm* and *100 μm* in order to make it possible to focus and collimate with identical objectives. This can improve the collection efficiency and reduce the photoluminescence signal from the substrate at the reflection side. This substrate not only makes it very difficult to transfer the flake onto it, as they are extremely fragile, but also produces a high photoluminescence signal. Another idea for the transmission configuration is to make a free standing sample. We tried two ways of implementing this. We make parallel lines with a cutter on one side of the silicon wafer substrate with a depth of *60%* of the thickness, and make another line on the other side of the substrate to *50%* of the substrate depth, which is perpendicular to the lines on first side. We therefore have a substrate with a square extruded cut through all the substrate in the cross point of the two lines. Figure App.3 presents a schematic view of this substrate. The main disadvantage of this method is the choice of substrate material. Instead of using fused silica, which is very fragile, we use silicon for this purpose. Another limiting factor for this method is the size of these squares, which is the thickness of the blade (*40-50 μm*) used for this process. This means that to successfully transfer the crystal to the substrate our flake should be about two times larger than the square (*roughly 100 μm* by *100 μm*). The largest crystal size which we have is *100 μm* by *50 μm* and it is very difficult to get such a large crystal by mechanical exfoliation.

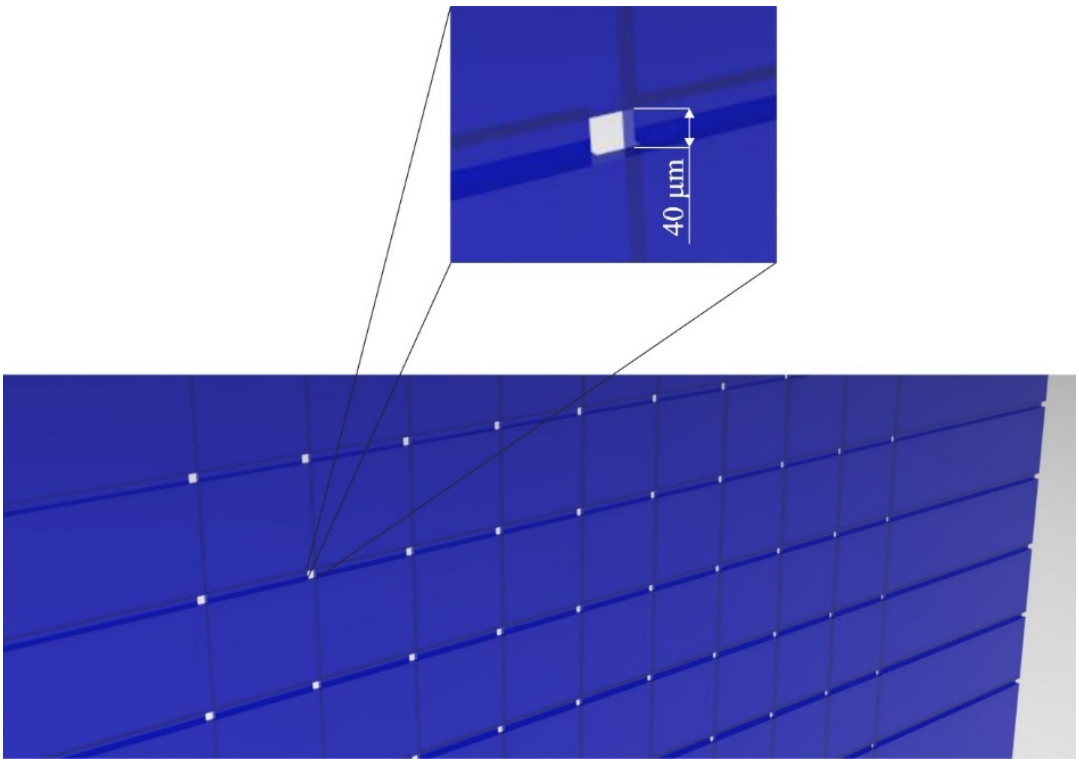

Figure App.3 Schematic view of the silicon substrate with rectangle holes. This substrate has straight horizontal cuts from one side with the depth of 300 µm and vertical cuts from the other side with the depth of 250 µm, while the thickness of the substrate is 500 µm. The hole has a square shape with dimension of 40 µm.

The other idea, which has greater potential, is to make a hole by laser beam on the thin fused silica substrate and transfer the flake onto the hole. In this method, we do not have a problem with the hole size and the material for the substrate. Figure App.4 (a) presents our laser substrates with holes made using a femtosecond Ti-Sapphire laser with *100 Hz* repetition rate. It is relatively easy to transfer the monolayer flake onto this hole. Figure App.4 (b) shows the transferred flake on the hole. After transferring the flake onto the whole, surprisingly, we measured a huge photoluminescence signal from the substrate. After a test measurement of the photoluminescence from the substrate and the edge of the hole, we discovered that as a result of making hole with laser beam, the structure of substrate material changes and when we excite the edge of the hole even by a very low intensity we measure a very strong photoluminescence from this edge. This important disadvantage mean that the best method is to use the normal fused silica substrate and chose the transmission configuration as the main method of the cross-correlation measurement.

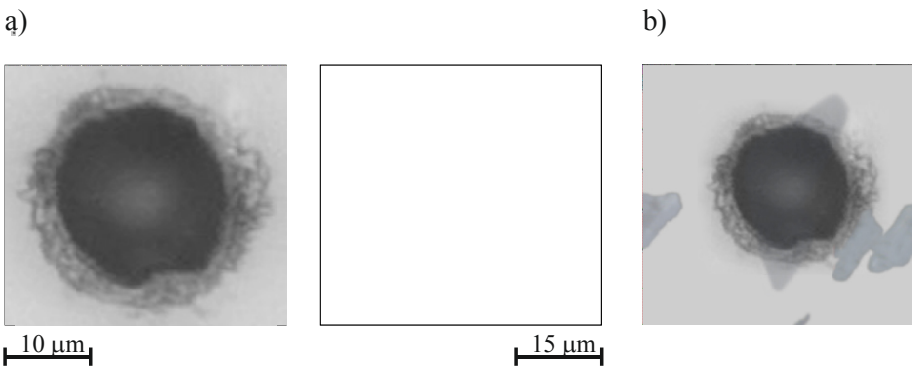

Figure App.4 Laser made hole in fused silica. We use a high power femtosecond laser to make a hole on the fused silica (a), and transferred a free standing flake of mechanically exfoliated monolayer crystal on the fused silica (b).

6 References

[1] P. Milonni and U. Mohideen, 'Casimir Effect', in *Compendium of Quantum Physics*, D. Greenberger, K. Hentschel, and F. Weinert, Eds. Berlin, Heidelberg: Springer Berlin Heidelberg, 2009, pp. 87–88.

[2] N. D. Birrell, *Quantum Fields in Curved Space*. Cambridge: Cambridge University Press, 1982.

[3] W. G. Unruh, 'Notes on black-hole evaporation', *Phys Rev D*, vol. 14, no. 4, pp. 870–892, Aug. 1976.

[4] S. W. Hawking, 'Particle creation by black holes', *Commun. Math. Phys.*, vol. 43, no. 3, pp. 199–220, 1975.

[5] G. T. Moore, 'Quantum Theory of the Electromagnetic Field in a Variable-Length One-Dimensional Cavity', *J. Math. Phys.*, vol. 11, no. 9, pp. 2679–2691, Sep. 1970.

[6] V. V. Dodonov and A. B. Klimov, 'Generation and detection of photons in a cavity with a resonantly oscillating boundary', *Phys Rev A*, vol. 53, no. 4, pp. 2664–2682, Apr. 1996.

[7] S. A. Fulling and P. C. W. Davies, 'Radiation from a Moving Mirror in Two Dimensional Space-Time: Conformal Anomaly', *Proc. R. Soc. Lond. Math. Phys. Sci.*, vol. 348, no. 1654, p. 393, Mar. 1976.

[8] G Barton, 'On the fluctuations of the Casimir forces. II. The stress-correlation function', *J. Phys. Math. Gen.*, vol. 24, no. 23, p. 5533, 1991.

[9] E. Yablonovitch, 'Accelerating reference frame for electromagnetic waves in a rapidly growing plasma: Unruh-Davies-Fulling-DeWitt radiation and the nonadiabatic Casimir effect', *Phys Rev Lett*, vol. 62, no. 15, pp. 1742–1745, Apr. 1989.

[10] J. Schwinger, 'Casimir energy for dielectrics.', *Proc. Natl. Acad. Sci.*, vol. 89, no. 9, pp. 4091–4093, May 1992.

[11] V. V. Dodonov, A. B. Klimov, and V. I. Man'ko, 'Nonstationary Casimir effect and oscillator energy level shift', *Phys. Lett. A*, vol. 142, no. 8, pp. 511–513, Dec. 1989.

[12] Harry Johnston and Sarben Sarkar, 'A re-examination of the quantum theory of optical cavities with moving mirrors', *J. Phys. Math. Gen.*, vol. 29, no. 8, p. 1741, 1996.

[13] G. Barton and C. Eberlein, 'On Quantum Radiation from a Moving Body with Finite Refractive Index', *Ann. Phys.*, vol. 227, no. 2, pp. 222–274, Nov. 1993.

[14] A. Lambrecht, M.-T. Jaekel, and S. Reynaud, 'Motion Induced Radiation from a Vibrating Cavity', *Phys Rev Lett*, vol. 77, no. 4, pp. 615–618, Jul. 1996.

[15] V. V. Dodonov, 'Nonstationary Casimir Effect and Analytical Solutions for Quantum Fields in Cavities with Moving Boundaries', in *Modern Nonlinear Optics, Part I*, John Wiley & Sons, Inc., 2002, pp. 309–394.

[16] V. V. Dodonov and A. V. Dodonov, 'Quantum Harmonic Oscillator and Nonstationary Casimir Effect', *J. Russ. Laser Res.*, vol. 26, no. 6, pp. 445–483, 2005.

[17] D. Faccio and I. Carusotto, 'Dynamical Casimir Effect in optically modulated cavities', *EPL Europhys. Lett.*, vol. 96, no. 2, p. 24006, 2011.

[18] E. Yablonovitch, J. P. Heritage, D. E. Aspnes, and Y. Yafet, 'Virtual photoconductivity', *Phys. Rev. Lett.*, vol. 63, no. 9, pp. 976–979, Aug. 1989.

[19] Teruaki Okushima and Akira Shimizu, 'Photon Emission from a False Vacuum of Semiconductors', *Jpn. J. Appl. Phys.*, vol. 34, no. 8S, p. 4508, 1995.

[20] Yurii E Lozovik and V G Tsvetus and E A Vinogradov, 'Parametric excitation of vacuum by use of femtosecond laser pulses', *Phys. Scr.*, vol. 52, no. 2, p. 184, 1995.

[21] C. Braggio and G. Bressi and G. Carugno and C. Del Noce and G. Galeazzi and A. Lombardi and A. Palmieri and G. Ruoso and D. Zanello, 'A novel experimental approach for the detection of the dynamical Casimir effect', *EPL Europhys. Lett.*, vol. 70, no. 6, p. 754, 2005.

[22] M. Tsindlekht, M. Golosovsky, H. Chayet, D. Davidov, and S. Chocron, 'Frequency modulation of the superconducting parallel-plate microwave resonator by laser irradiation', *Appl. Phys. Lett.*, vol. 65, no. 22, pp. 2875–2877, Nov. 1994.

[23] V. I. Man'ko, 'The Casimir effect and quantum vacuum generator', *J. Sov. Laser Res.*, vol. 12, no. 5, pp. 383–385, 1991.

[24] V. V. Dodonov, Man'ko O V, and Man'ko V I, 'Squeezed and Correlated States of Quantum Systems', *Proc. Lebedev Phys. Inst.*, vol. 205.

[25] K Takashima and N Hatakenaka and S Kurihara and A Zeilinger, 'Nonstationary boundary effect for a quantum flux in superconducting nanocircuits', *J. Phys. Math. Theor.*, vol. 41, no. 16, p. 164036, 2008.

[26] J. R. Johansson, G. Johansson, C. M. Wilson, and F. Nori, 'Dynamical Casimir Effect in a Superconducting Coplanar Waveguide', *Phys Rev Lett*, vol. 103, no. 14, p. 147003, Sep. 2009.

[27] C. M. Wilson *et al.*, 'Observation of the dynamical Casimir effect in a superconducting circuit', *Nature*, vol. 479, no. 7373, pp. 376–379, Nov. 2011.

[28] R. Boyd, *Nonlinear Optics*, 3rd ed. Elsevier Wordmark, 2008.

[29] R. L. Sutherland, *Handbook of Nonlinear Optics*, 2nd ed. MARCEL DEKKER, INC.

[30] A. Yariv, *Quantum Eectronics*, 3rd ed. Wiley.

[31] K. Koch, E. C. Cheung, G. T. Moore, S. H. Chakmakjian, and J. M. Liu, 'Hot spots in parametric fluorescence with a pump beam of finite cross section', *IEEE J. Quantum Electron.*, vol. 31, no. 5, pp. 769–781, May 1995.

[32] R. L. Liboff, *Introductory Quantum Mechanics*, 2nd ed. Wesley, 1992.

[33] J. T. Mendonça and A. Guerreiro, 'Time refraction and the quantum properties of vacuum', *Phys. Rev. A*, vol. 72, no. 6, p. 063805, Dec. 2005.

[34] J. T. Mendonça, G. Brodin, and M. Marklund, 'Vacuum effects in a vibrating cavity: Time refraction, dynamical Casimir effect, and effective Unruh acceleration', *Phys. Lett. A*, vol. 372, no. 35, pp. 5621–5624, Aug. 2008.

[35] F. X. Dezael and A. Lambrecht, 'Analogue Casimir radiation using an optical parametric oscillator', *EPL Europhys. Lett.*, vol. 89, no. 1, p. 14001, 2010.

[36] F. Träger, *Springer Handbook of Lasers and Optics*, 2nd ed. Springer Berlin Heidelberg, 2012.

[37] K. S. Novoselov *et al.*, 'Electric Field Effect in Atomically Thin Carbon Films', *Science*, vol. 306, no. 5696, p. 666, Oct. 2004.

[38] J. S. Park, W.-J. Maeng, H.-S. Kim, and J.-S. Park, 'Review of recent developments in amorphous oxide semiconductor thin-film transistor devices', *Thin Solid Films*, vol. 520, no. 6, pp. 1679–1693, Jan. 2012.

[39] R. G. Dickinson and L. Pauling, 'THE CRYSTAL STRUCTURE OF MOLYBDENITE', *J. Am. Chem. Soc.*, vol. 45, no. 6, pp. 1466–1471, Jun. 1923.

[40] P. Joensen, R. F. Frindt, and S. R. Morrison, 'Single-layer MoS_2', *Mater. Res. Bull.*, vol. 21, no. 4, pp. 457–461, Apr. 1986.

[41] A. Castellanos-Gomez, N. Agraït, and G. Rubio-Bollinger, 'Optical identification of atomically thin dichalcogenide crystals', *Appl. Phys. Lett.*, vol. 96, no. 21, p. 213116, May 2010.

[42] Y.-H. Lee *et al.*, 'Synthesis of Large-Area MoS_2 Atomic Layers with Chemical Vapor Deposition', *Adv. Mater.*, vol. 24, no. 17, pp. 2320–2325, 2012.

[43] K.-K. Liu *et al.*, 'Growth of Large-Area and Highly Crystalline MoS_2 Thin Layers on Insulating Substrates', *Nano Lett.*, vol. 12, no. 3, pp. 1538–1544, Mar. 2012.

[44] Y. Zhan, Z. Liu, S. Najmaei, P. M. Ajayan, and J. Lou, 'Large-Area Vapor-Phase Growth and Characterization of MoS_2 Atomic Layers on a SiO2 Substrate', *Small*, vol. 8, no. 7, pp. 966–971, 2012.

[45] Y.-C. Lin *et al.*, 'Wafer-scale MoS_2 thin layers prepared by MoO3 sulfurization', *Nanoscale*, vol. 4, no. 20, pp. 6637–6641, 2012.

[46] A. M. van der Zande *et al.*, 'Grains and grain boundaries in highly crystalline monolayer molybdenum disulphide', *Nat Mater*, vol. 12, no. 6, pp. 554–561, Jun. 2013.

[47] S. Najmaei *et al.*, 'Vapour phase growth and grain boundary structure of molybdenum disulphide atomic layers', *Nat Mater*, vol. 12, no. 8, pp. 754–759, Aug. 2013.

[48] A. Kuc, N. Zibouche, and T. Heine, 'Influence of quantum confinement on the electronic structure of the transition metal sulfide TS_2', *Phys. Rev. B*, vol. 83, no. 24, p. 245213, Jun. 2011.

[49] K. F. Mak, C. Lee, J. Hone, J. Shan, and T. F. Heinz, 'Atomically Thin MoS_2: A New Direct-Gap Semiconductor', *Phys. Rev. Lett.*, vol. 105, no. 13, p. 136805, Sep. 2010.

[50] N. Kumar *et al.*, 'Second harmonic microscopy of monolayer MoS_2', *Phys. Rev. B*, vol. 87, no. 16, p. 161403, Apr. 2013.

[51] L. M. Malard, T. V. Alencar, A. P. M. Barboza, K. F. Mak, and A. M. de Paula, 'Observation of intense second harmonic generation from MoS_2 atomic crystals', *Phys. Rev. B*, vol. 87, no. 20, p. 201401, May 2013.

[52] Y. Li *et al.*, 'Probing Symmetry Properties of Few-Layer MoS_2 and h-BN by Optical Second-Harmonic Generation', *Nano Lett.*, vol. 13, no. 7, pp. 3329–3333, Jul. 2013.

[53] M. L. Trolle, G. Seifert, and T. G. Pedersen, 'Theory of excitonic second-harmonic generation in monolayer MoS_2', *Phys Rev B*, vol. 89, no. 23, p. 235410, Jun. 2014.

[54] D. J. Clark *et al.*, 'Erratum: Strong optical nonlinearity of CVD-grown MoS $_2$monolayer as probed by wavelength-dependent second-harmonic generation [Phys. Rev. B 90, 121409(R) (2014)]', *Phys. Rev. B*, vol. 92, no. 15, p. 159901, Oct. 2015.

[55] D. J. Clark *et al.*, 'Strong optical nonlinearity of CVD-grown MoS $_2$ monolayer as probed by wavelength-dependent second-harmonic generation', *Phys. Rev. B*, vol. 90, no. 12, p. 121409, Sep. 2014.

[56] M. Grüning and C. Attaccalite, 'Second harmonic generation in h-BN and MoS$_2$ monolayers: Role of electron-hole interaction', *Phys Rev B*, vol. 89, no. 8, p. 081102, Feb. 2014.

[57] G. A. Wagoner, P. D. Persans, E. A. V. Wagenen, and G. M. Korenowski, 'Second-harmonic generation in molybdenum disulfide', *J Opt Soc Am B*, vol. 15, no. 3, pp. 1017–1021, Mar. 1998.

[58] 'SPCM-NIR NIR-Optimized Single Photon Counting Module'. Excetilas.

[59] 'Redefining Measurement ID230 Infrared Single-Photon Detector'. IDQuantique.

[60] N. Westerberg, 'On oscillating intensities and the Dynamical Casimir e_ect'. Internal report, 2014.

[61] T. S. Y. D. West D. J.Brady, D. W.Hewak, 'Gallium Lanthanum Sulphide Fibers for Infrared Transmission', *Fiber Integr. Opt.*, vol. 19, no. 3, pp. 229–250, Jul. 2000.

[62] Evgenii M Dianov and P G Kazanskiĭ and D Yu Stepanov, 'Problem of the photoinduced second harmonic generation in optical fibers', *Sov. J. Quantum Electron.*, vol. 19, no. 5, p. 575, 1989.

[63] I. Kang, T. D. Krauss, F. W. Wise, B. G. Aitken, and N. F. Borrelli, 'Femtosecond measurement of enhanced optical nonlinearities of sulfide glasses and heavy-metal-doped oxide glasses', *J. Opt. Soc. Am. B*, vol. 12, no. 11, pp. 2053–2059, Nov. 1995.

[64] Z. H. Zhou, T. Hashimoto, H. Nasu, and K. Kamiya, 'Two-photon absorption and nonlinear refraction of lanthanum sulfide-gallium sulfide glasses', *J. Appl. Phys.*, vol. 84, no. 5, pp. 2380–2384, Sep. 1998.

[65] G. Demetriou *et al.*, 'Refractive index and dispersion control of ultrafast laser inscribed waveguides in gallium lanthanum sulphide for near and mid-infrared applications', *Opt. Express*, vol. 24, no. 6, pp. 6350–6358, Mar. 2016.

[66] G. Demetriou, 'Ultrafast Nonlinear Optics of Bulk and Two-Dimensional Materials for Infrared Applications', Heriot Watt University, 2016.

[67] J. C. A. Tyrrell *, P. Kinsler, and G. H. C. New, 'Pseudospectral spatial-domain: a new method for nonlinear pulse propagation in the few-cycle regime with arbitrary dispersion', *J. Mod. Opt.*, vol. 52, no. 7, pp. 973–986, May 2005.

[68] M. Marshall, 'Photon Pair Generation in a Modulated Waveguide', Mphys, Heriot Watt University, Edinburgh, 2014.

[69] J.-C. Diels and W. Rudolph, '8 - Pulse Shaping', in *Ultrashort Laser Pulse Phenomena (Second Edition)*, Burlington: Academic Press, 2006, pp. 433–456.

[70] K. M. Davis, K. Miura, N. Sugimoto, and K. Hirao, 'Writing waveguides in glass with a femtosecond laser', *Opt. Lett.*, vol. 21, no. 21, pp. 1729–1731, Nov. 1996.

[71] R. R. Thomson and G. Cerullo, 'Ultrafast Laser Inscription of Photonic Devices in Bulk Dielectrics', in *Ultrafast Nonlinear Optics*, R. Thomson, C. Leburn, and D. Reid, Eds. Heidelberg: Springer International Publishing, 2013, pp. 323–350.

[72] S. mukherjee, 'Characterisation of Modulated and plitting waveguide'. not published-internal report.

[73] T. Schweizer, F. Goutaland, E. Martins, D. W. Hewak, and W. S. Brocklesby, 'Site-selective spectroscopy in dysprosium-doped chalcogenide glasses for 1.3-μm optical-fiber amplifiers', *J. Opt. Soc. Am. B*, vol. 18, no. 10, pp. 1436–1442, Oct. 2001.

[74] G. Agrawal, *Nonlinear Fiber Optics (Fifth Edition)*. Boston: Academic Press, 2013.

[75] T. Eichelkraut, S. Weimann, S. Stützer, S. Nolte, and A. Szameit, 'Radiation-loss management in modulated waveguides', *Opt. Lett.*, vol. 39, no. 24, pp. 6831–6834, Dec. 2014.

[76] X. Wang *et al.*, 'Correlation between multiple modulation instability side lobes in dispersion oscillating fiber', *Opt Lett*, vol. 39, no. 7, pp. 1881–1884, Apr. 2014.

[77] S. Pitois and G. Millot, 'Experimental observation of a new modulational instability spectral window induced by fourth-order dispersion in a normally dispersive single-mode optical fiber', *Opt. Commun.*, vol. 226, no. 1, pp. 415–422, 2003.

[78] J. G. Rarity, J. Fulconis, J. Duligall, W. J. Wadsworth, and P. S. J. Russell, 'Photonic crystal fiber source of correlated photon pairs', *Opt. Express*, vol. 13, no. 2, pp. 534–544, Jan. 2005.

[79] O. Alibart, J. Fulconis, G. K. L. Wong, S. G. Murdoch, W. J. Wadsworth, and J. G. Rarity, 'Photon pair generation using four-wave mixing in a microstructured fibre: theory versus experiment', *New J. Phys.*, vol. 8, no. 5, p. 67, 2006.

[80] A. Mussot, S. Trillo, M. Conforti, and A. Kudlisnki, 'Multiple quasi-phase matched resonant radiations induced by modulation instability in dispersion oscillating fibers', vol. arXiv:1505.01256.

[81] M. Droques *et al.*, 'Fourth-order dispersion mediated modulation instability in dispersion oscillating fibers', *Opt Lett*, vol. 38, no. 17, pp. 3464–3467, Sep. 2013.

[82] P. Russell, 'Photonic Crystal Fibers', *Science*, vol. 299, no. 5605, p. 358, Jan. 2003.

[83] Desmond M. Chow, S. R. Sandoghchi, and F. R. Mahamd Adikan, 'Fabrication of Photonic Crystal Fibers', vol. 3d.

[84] M. Droques, A. Kudlinski, G. Bouwmans, G. Martinelli, and A. Mussot, 'Experimental demonstration of modulation instability in an optical fiber with a periodic dispersion landscape', *Opt. Lett.*, vol. 37, no. 23, pp. 4832–4834, Dec. 2012.

[85] Alan Migdall, Sergey Polyakov, Jingyun Fan, and Joshua Bienfang, *Single-Photon Generation and Detection*, 1st ed., vol. 45. ELSEVIER, 2013.

[86] H. Zhang *et al.*, 'Measuring the Refractive Index of Highly Crystalline Monolayer MoS_2 with High Confidence', vol. 5, p. 8440, Feb. 2015.

[87] P. Kapusta, M. Wahl, and R. Erdmann, *Advanced Photon Counting*. Springer, 2015.